STUDIA UNIVERSITATIS
BABEŞ-BOLYAI

UNIVERSITATEA BABEŞ-BOLYAI
BABEŞ-BOLYAI TUDOMÁNYEGYETEM
BABEŞ-BOLYAI UNIVERSITÄT
BABEŞ-BOLYAI UNIVERSITY
TRADITIO ET EXCELLENTIA

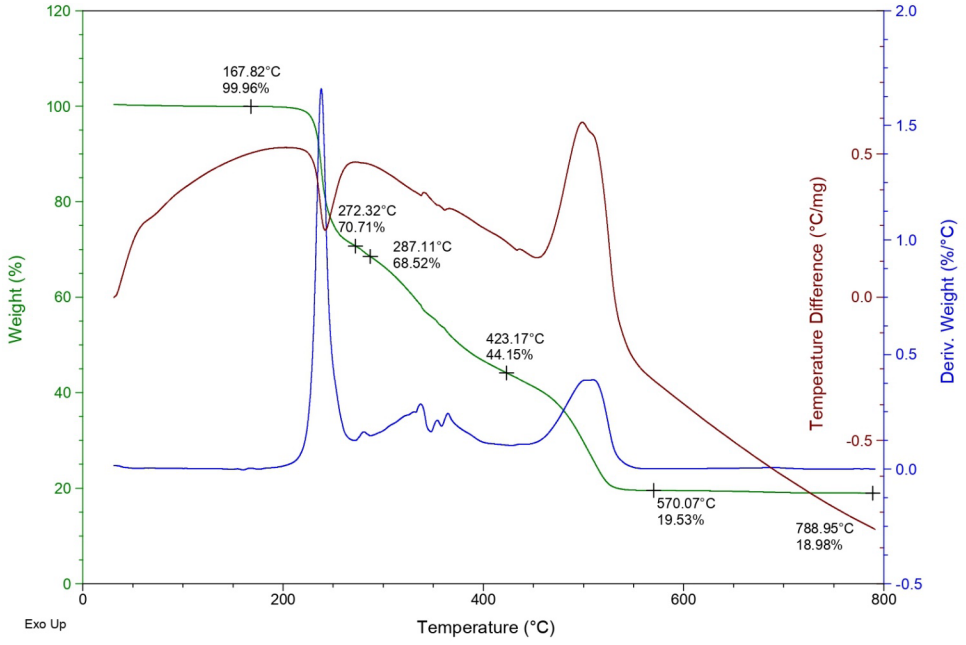


# CHEMIA

2/2024

# STUDIA UNIVERSITATIS BABEŞ-BOLYAI CHEMIA

## 2/2024

ISSN (print): 1224-7154;
ISSN (online): 2065-9520; ISSN-L: 2065-9520

Published by Babeş-Bolyai University

http://chem.ubbcluj.ro/~studiachemia/;
http://www.studia.ubbcluj.ro/serii/chemia/index_en.html

**YEAR** **Volume 69 (LXIX) 2024**
**MONTH** **June**
**ISSUE** **2**

PUBLISHED ONLINE: 2024-06-30
PUBLISHED PRINT: 2024-06-30
ISSUE DOI: 10.24193/subbchem.2024.2

# S T U D I A
# UNIVERSITATIS BABEŞ–BOLYAI
# CHEMIA

## 2

### CONTENT/ SOMMAIRE/ INHALT/ CUPRINS

Studia Universitatis Babes-Bolyai Chemia has been selected for coverage in Thomson Reuters products and custom information services. Beginning with V. 53 (1) 2008, this publication is indexed and abstracted in the following:

- Science Citation Index Expanded (also known as SciSearch®)
- Chemistry Citation Index®
- Journal Citation Reports/Science Edition

STUDIA UBB CHEMIA, LXIX, 2, 2024 (p. 7-17)
(RECOMMENDED CITATION)
DOI:10.24193/subbchem.2024.2.01

# COMPARATIVE PHASE EVOLUTION, MORPHOLOGICAL AND OPTICAL ANALYSIS OF PARTIALLY STABILIZED ZIRCONIA CERAMICS

**Claudia Andreea COJAN[a], Réka BARABÁS[b], Marieta MUREȘAN-POP[c,d], Liliana BIZO[a,c,*]**

**ABSTRACT.** Partially stabilized zirconia (PSZ) ceramics are one of the most important materials used for different applications like thermal barrier coatings, refractories, oxygen-permeating membranes, and dental and bone implants. In this work, the structural, morphological, and optical properties of bulk Mg-PSZ, Ca-PSZ, and Ce-PSZ, prepared by solid state reaction at high temperature, were comparatively evaluated. Laser diffraction analyses revealed particles by thousands orders of magnitude larger compared to crystallite sizes determined from X-ray powder diffraction (XRPD), more evidenced in the case of Ca-PSZ. The structural analyses indicated the presence of both *m*- and *t*-$ZrO_2$ phases, in different ratios, depending on the doping cation. The scanning electron microscopy (SEM) micrographs confirmed the homogenous distribution of the elements through mixed oxides. Further, optical properties evaluated in terms of ultraviolet–visible diffuse reflectance spectroscopy (UV-VIS DRS) revealed that the doped $ZrO_2$ samples showed a smaller bandgap compared with pure $ZrO_2$, which may be due to the incorporation of magnesia, calcia or ceria in the $ZrO_2$ matrix. The maximum bandgap reduction of $ZrO_2$ was observed on Ca-PSZ, having a value of 3.52 eV.

***Keywords:*** *partially stabilized zirconia, solid state reaction, structural properties, optical properties*

[a] *Department of Chemical Engineering, Babeş-Bolyai University, 11 Arany Janos Street, RO-400028, Cluj-Napoca, Romania*
[b] *Department of Chemistry and Chemical Engineering of Hungarian Line of Study, Babeş-Bolyai University, 11 Arany Janos Street, RO-400028, Cluj-Napoca, Romania*
[c] *Interdisciplinary Research Institute on Bio-Nano-Sciences, Babeş-Bolyai University, 42 Treboniu Laurian Street, RO-400271, Cluj-Napoca, Romania*
[d] *INSPIRE Research Platform, Babeş-Bolyai University, 11 Arany Janos Street, RO-400028, Cluj-Napoca, Romania*
** Corresponding author: liliana.bizo@ubbcluj.ro*

## INTRODUCTION

Besides many ceramic materials, zirconia ($ZrO_2$), which is also known as “ceramic steel”, has gained a special interest among researchers due to its multiple applications such as catalysts, sensors, and semiconductor devices, and structural materials, such as coatings on cutting tools ceramics, or implants [1]. The most useful mechanical properties can be achieved when zirconia is in a multiphase form or partially stabilized zirconia (PSZ), obtained by adding small amounts of a metal oxide dopant, such as MgO (magnesia), CaO (calcia), $Sc_2O_3$ (scandia), $Y_2O_3$ (yttria) and ceria ($CeO_2$) [1-3].

PSZ are interesting materials due to their fascinating properties like good flexural strength, high toughness, excellent wear resistance, high thermal shock resistance, good ionic conductivity, and biocompatible, finding applications in thermal barrier coatings, refractories, oxygen-permeating membranes, dental and bone implants [4].

About 10 mol% Mg is the percentage most used in industry to obtain Mg-PSZ (magnesia partially stabilized zirconia) [5]. Mg-PSZ exhibits satisfactory thermal shock resistance, high mechanical properties and a small thermal expansion coefficient. MgO or $MgCO_3$ could be used as a stabilizer, and one of the advantages presented by these compounds is that they can be used in humid, high-temperature environments [6]. Ca-PSZ (calcia partially stabilized zirconia) has shown excellent thermal stability and corrosion resistance in extreme environments. It could be used in immersion nozzle refractories for continuous steel casting involving extremely high temperatures (~1500 °C) and corrosive molten flow environments [7-10]. The accessibility of calcium precursors is another aspect that makes the Ca-PSZ an interesting material. $CeO_2$ nanoparticles have important attention due to their unique characteristics and distinctive properties such as high refractive index, high thermal stability, high hardness, high surface area, UV absorbing ability, facile electrical conductivity, specific chemical reactivity, or large oxygen storage capacity [11]. Stabilizing $ZrO_2$ with $CeO_2$ improves the physicochemical properties of zirconia, Ce-PSZ (ceria partially stabilized zirconia) being recognized as a high-toughness ceramic.

The role of Ca and Mg dopant cations in phase stabilization of $ZrO_2$ has been intensively studied, with Mg emerging as a crucial dopant ion because of its ability to enhance the photocatalytic properties of $ZrO_2$ [12]. On the other hand, the Ce inclusion in $ZrO_2$ is expected to reduce thermal conductivity, which would widen the utilization of Ce doped $ZrO_2$ in thermal barrier coating applications [13]. Even if the phase stability was intensively studied in the last years, the role of alkaline earth and rare earth doping cations in zirconia have been widely examined at present. Thus, a *comparative study* of structural

and optical properties of bulk PSZ, which could provide an insight on the phase stabilization and structure modifications due to the Ca, Mg and Ce-doping in $ZrO_2$, which has not yet been reported to the best of our knowledge, is necessary.

The present work reported the facile synthesis of bulk Mg-PSZ, Ca-PSZ and Ce-PSZ by solid-state reaction at high temperature. The effect of doping with 10 at% Mg, Ca or Ce on zirconia's structural, morphological and optical properties, determined by different techniques, was comparatively analyzed and discussed.

## RESULTS AND DISCUSSION

The particle size distribution (PSD) of the prepared PSZ ceramic powders was analyzed by laser diffraction with the results given in **Figure 1**. From the PSD data presented graphically in the figure there are two types of curves: differential and cumulative. It can be observed that the PSD curves of Mg-PSZ and Ce-PSZ overlap, implying that the particle sizes for both materials were approximately identical. In addition, a wide bimodal distribution presenting two maximum points, which are centered at around 0.1 μm was revealed. Conversely, in the Ca-PSZ sample, the results show a narrow distribution with fractions ranging from 3 μm to 20 μm.

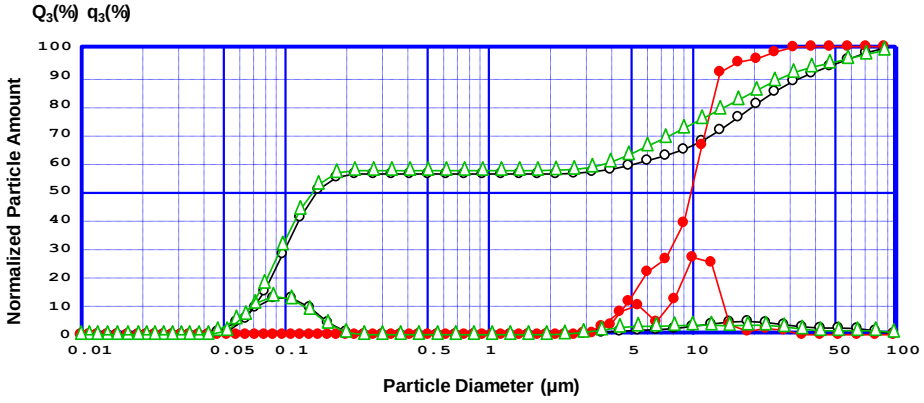


**Figure 1.** Differential and cumulative PSD curves of Mg-PSZ (black), Ca-PSZ (red) and Ce-PSZ (green) ceramics.

The results summarized in **Table 1** show that the Mg-PSZ and Ce-PSZ contain finer particles, with a mean value of 0.978 μm, and 0.851 μm, respectively, whereas larger particles were found for the Ca-PSZ, with a mean value of 9.030 μm. The modal and median diameters, defined for the cumulative distribution, are also shown.

**Table 1.** The results of particle size analyses of Mg-PSZ, Ca-PSZ and Ce-PSZ ceramics

| Sample ID | Median D (μm) | Modal D (μm) | Mean V (μm) | SD* | $D_{25}$ (μm) | $D_{50}$ (μm) | $D_{75}$ (μm) |
|---|---|---|---|---|---|---|---|
| Mg-PSZ | 0.145 | 0.087 | 0.978 | 1.161 | 0.092 | 0.145 | 16.227 |
| Ca-PSZ | 9.808 | 9.993 | 9.030 | 0.192 | 6.858 | 9.808 | 11.930 |
| Ce-PSZ | 0.138 | 0.087 | 0.851 | 1.121 | 0.088 | 0.138 | 11.040 |

* SD- standard deviation

To determine the structural properties, XRPD analyses were performed on Ca-PSZ, Mg-PSZ, and Ce-PSZ samples with the XRPD patterns shown in **Figure 2.**

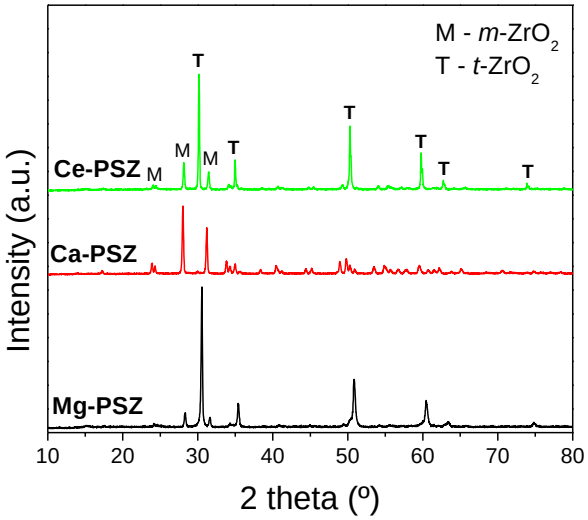


**Figure 2.** XRPD patterns of the prepared PSZ bulk ceramics.

Their examination revealed polymorphic powders because monoclinic (*m*-$ZrO_2$) and tetragonal (*t*-$ZrO_2$) structures are exhibited. For the phase identification the crystallographic information files corresponding to the pure monoclinic and tetragonal zirconia (*m*-$ZrO_2$, PDF # 96-152-8985; *t*-$ZrO_2$, PDF # 96-230-0613) phases from Crystallography Open Database (COD) of Match! Software were used.

The crystallite sizes of the prepared compositions were estimated using Scherrer equation:

$$D_{hkl}=0.9\lambda/(\beta\cos\theta) \quad (1)$$

where: D - crystallite size along (hkl) direction, β - full width half maximum (FWHM) of the most intense diffraction line, λ - wavelength of X-ray, θ - the Bragg angle [14].

The calculated *m*-$ZrO_2$ and *t*-$ZrO_2$ weight fractions, estimated using Match! software, and evolution of the crystallite sizes, determined by the Scherrer formula, are presented in **Table 2**. The calculated crystallite size of PSZ ranges in the nanometric domain, with the lowest value obtained for Ca-PSZ. The Mg-PSZ and Ce-PSZ powders are mainly composed of *t*-$ZrO_2$, with small peaks belonging to the *m*-$ZrO_2$ phase which are more evident in Ce-PSZ, whereas in the Ca-PSZ sample the predominant phase is *m*-$ZrO_2$. For the Mg-PSZ sample, the small difference between ionic radii of the $Zr^{4+}$ (0.84 Å) and $Mg^{2+}$ (0.72 Å), the substitution of $Zr^{4+}$ on its lattice site by the $Mg^{2+}$ ion is expected [2]. Furthermore, since Mg has the oxidation state of +2, it induces some oxygen vacancy in the structure which could be the main reason for the stabilization of the *t*-$ZrO_2$ phase [15]. In the case of Ca-PSZ, the increase in the lattice parameter is expected as the $Ca^{2+}$ (1.00 Å) has a larger ionic radius than that of $Zr^{4+}$(0.86 Å). Substituting Ce with a higher ionic radius (0.97 Å) at Zr sites induces slight change in the lattice parameters. The mixture of *m*-$ZrO_2$ and *t*-$ZrO_2$ phases indicated that they were partially stabilized by the MgO, CaO, and $CeO_2$.

**Table 2.** The *t*- and *m*-$ZrO_2$ phase fractions and crystallite size calculated by Scherrer formula for the prepared PSZ materials.

| **Sample ID** | ***t*-$ZrO_2$ (wt.%)** | ***m*-$ZrO_2$ (wt.%)** | **$D_{Scherrer}$* (nm)** |
|---|---|---|---|
| Mg-PSZ | 79.2 | 20.8 | 47.79 |
| Ca-PSZ | 3.5 | 96.5 | 46.93 |
| Ce-PSZ | 66.6 | 33.4 | 59.98 |

The FTIR spectra of the prepared samples are displayed in Figure 3. Upon analyzing the spectra in the high-frequency region, it is evident that a broadband positioned around 3448 $cm^{-1}$ is present in all three samples. This band is caused by the stretching vibration of the -OH group from the adsorbed water and is also visible in the low region as a sharp band of low intensity located at 1637 $cm^{-1}$.

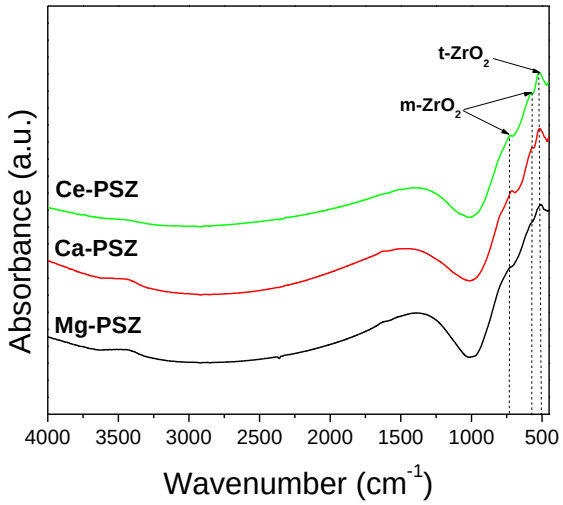


**Figure 3.** FTIR spectra of the prepared PSZ bulk ceramics.

Between 1600-1000 $cm^{-1}$, the broadband observed at ~ 1400 $cm^{-1}$, is likely due to the stretching mode vibration of Mg-O, Ca-O, or Ce-O bonds. [16]. The characteristic bands ascribed to the *m*-$ZrO_2$ are observed at 585 $cm^{-1}$ and 735 $cm^{-1}$, and *t*-$ZrO_2$ is 529 $cm^{-1}$ [17]. These results agree with the XRPD results where different phase ratio of *t*- and *m*-$ZrO_2$ phases were revealed, depending on the doping cations.

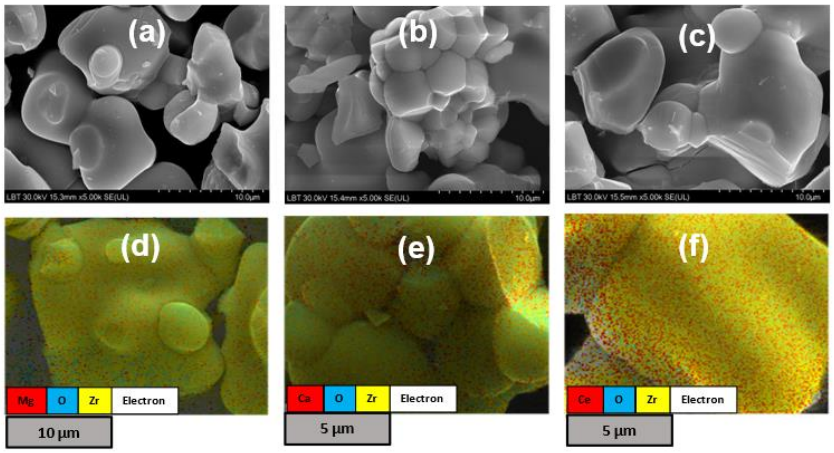


**Figure 4.** SEM images and corresponding elemental mapping of Mg-PSZ (a, d), Ca-PSZ (b, e), and Ce-PSZ (c, f), respectively

The results of morphological characterization of the prepared PSZ carried out using SEM are presented in **Figure 4a-c**. As shown irregular and agglomerated shapes like morphology were formed in the ceramic sample with grains interconnected to each other, as previously observed [18]. Qualitative analysis evaluated by elemental mapping (**Figure 4d-f**) confirmed the homogenous distribution of the elements in the PSZ samples. The results of elemental EDX analyses, displayed in **Figure 5** (right), accompanied by the SEM images of the surface of samples (left), confirmed the presence of the magnesium, calcium, cerium, zirconium, and oxygen elements. No other signals were detected, indicating the purity of the materials.

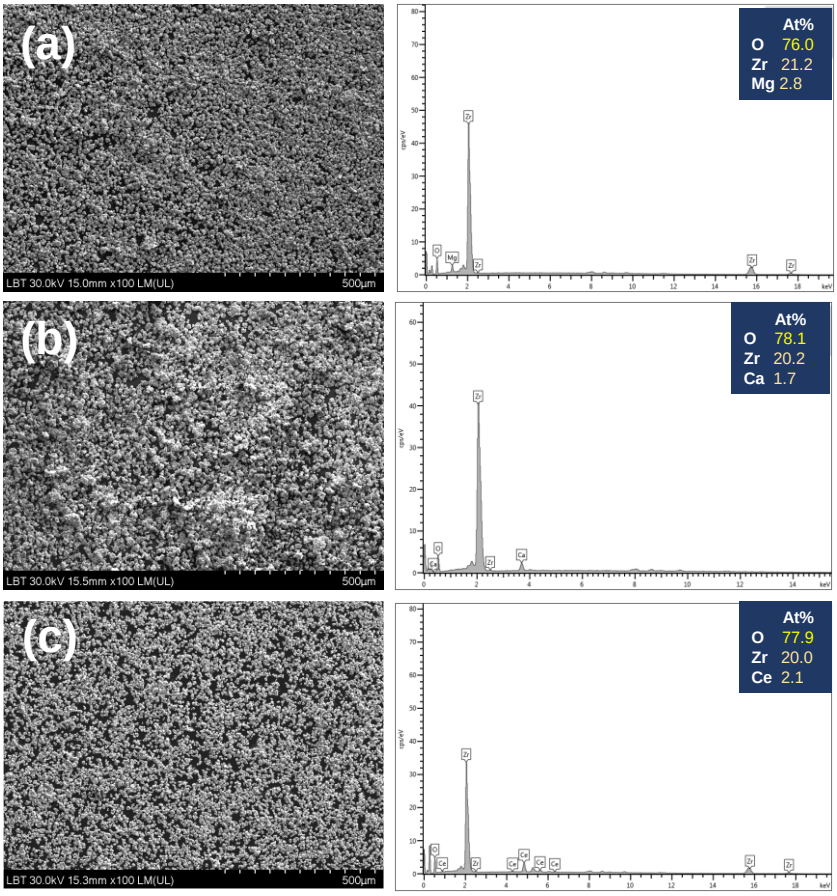


**Figure 5.** SEM images (left) under 100 X magnification and EDS (right) analysis for (a) Mg-PSZ, (b) Ca-PSZ and (c) Ce-PSZ.

The optical properties of the prepared compositions were considered in terms of UV-VIS DRS and the corresponding bandgaps ($E_g$) were calculated by Tauc plot using Kubelka-Munk function [19], as shown in **Figure 6a-d.** Depending on the types and chemical states of metal ions, the bandgaps of metal doped $ZrO_2$ varied, the differences being mainly associated with the electronic configurations of the ions, which control the energy levels in the $ZrO_2$. In our work, the determined bandgaps are 4.68 eV, 3.52 eV and 4.96 eV, for Mg-PSZ, Ca-PSZ, and Ce-PSZ, respectively. As know, $ZrO_2$ has a wide bandgap with the reported value of ~ 5.0 eV [20, 21]. The effects of Mg and Ca doping on the tetragonalization of the crystal structure and introduction of dopant states at the edge of the valence states below the Fermi level, as well as shifting the Fermi level towards the valence band maximum upon doping, have been previously demonstrated.

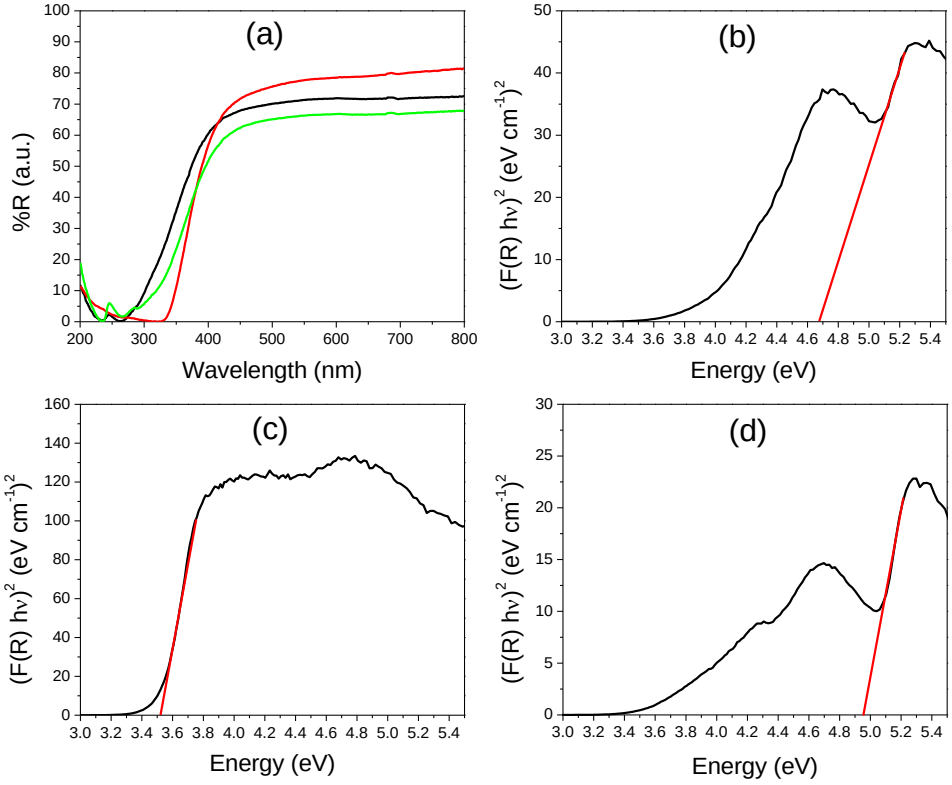


**Figure 6.** (a) UV-VIS DRS spectra of Mg-PSZ (black), Ca-PSZ (red) and Ce-PSZ (green) and corresponding Tauc plot for bandgap determination of (b) Mg-PSZ, (c) Ca-PSZ and (d) Ce-PSZ.

The reduced value of bandgaps on the doped zirconia may be due to the incorporation of the MgO, CaO or $CeO_2$. Recently, the role of oxygen vacancy in the RT stabilized *t*-$ZrO_2$ was investigated [22-25]. The presence of cerium stabilizes the metastable tetragonal phase at the expense of the monoclinic one [26]. Accordingly, the occupation of a regular crystal site by $Ce^{4+}$ induces the formation of discrete defect levels inside the material bandgap constituted by the empty localized 4f orbitals of the lanthanide ion, thus drastically improving the visible light absorption by a two-step photon absorption mechanism [26]. It should also be noted that the stabilization mechanisms of the dopants are different: MgO and CaO stabilize the *t*-$ZrO_2$ phase by introducing anionic oxygen vacancies similar to $Y_2O_3$, whereas $CeO_2$ stabilizes the *t*-$ZrO_2$ phase by dilating the cation network decreasing the strain energy and the relief of oxygen overcrowding [27,28].

## CONCLUSIONS

Bulk PSZ ceramic materials were successfully obtained by solid-state reaction at high temperature, followed by their characterization using laser diffraction, XRPD, FTIR, SEM/EDS and UV-VIS techniques. The structural analyses indicated the presence of both *m*- and *t*-$ZrO_2$ phases in different ratios, depending on the doping cation. Except for the Ca cation, which favoured the *m*-$ZrO_2$ phase formation, Mg and Ce played an important role in the tetragonalization of zirconia. Analysis by laser diffraction showed larger particle sizes compared to the calculated crystallite size, more pronounced in the Ca-PSZ, thereby confirming that this technique measures agglomerates and not individual particles. The SEM/EDS analysis confirmed the homogenous distribution of the elements through mixed oxide. Further, optical properties evaluated in terms of UV-VIS DRS spectra, revealed that the doped $ZrO_2$ samples showed a smaller bandgap compared with pure $ZrO_2$, which may be due to the incorporation of magnesia, calcia or ceria in the $ZrO_2$ matrix. Doping $ZrO_2$ represents an interesting approach to manipulating its bandgap, making these materials attractive in various applications, ranging from optoelectronics to prosthodontics, with the biomedical and bioengineering domains being of great importance.

## EXPERIMENTAL SECTION

The PSZ ceramic materials were prepared by solid state reaction at high temperature. To obtain 10 at% Mg, Ca or Ce in $ZrO_2$, starting powders of $ZrO_2$ (Riedel-de Haën AG, Germany, 99%), CaO (Alfa Aesar, Germany, 99.95%), MgO (Alfa Aesar, Germany, 99.99%) and $CeO_2$ (LOBA Feinchemie GmbH, Austria,

99.95%) were used as raw materials. The mixture of different oxides was grounded using an agate mortar and pestle, and then heated in an alumina crucible in air using an Nabertherm LHT 04/16 high-temperature furnace (Lilienthal, Germany), first at 900 °C and then at increasing temperatures from 1000 °C up to 1600 °C. At each time, the 12h annealings were followed by air quenching and regrinding of the mixtures.

Synthesized Mg-PSZ, Ca-PSZ and Ce-PSZ ceramics were further characterized using different methods.

The PSD of the prepared powdered ceramics was measured in suspension using a micro- and nanoparticle analyzer SALD-7101 (Shimadzu, Japan). For the measurements, the samples were immersed for 15 s in distilled water used as a solvent, with aggregation being reduced using treatment with ultrasounds.

XRPD analysis was performed to investigate the structure of the samples using a Shimadzu XRD-6000 diffractometer operating at 40 kV, 30 mA, with Ni-filter and graphite monochromator for CuKα (λ=1.54060 Å). The diffraction patterns were recorded in the 2θ range of 10–80° at a scan speed of 2 °/min.

FTIR measurements were performed using a Jasco FTIR 6200 spectrometer. The spectra were recorded from KBr pellets, with a spectral resolution of 4 $cm^{-1}$.

For the morphological analyses, the SEM/EDS images were obtained at 30 kV with different magnifications using a Hitachi SU8230 (Tokyo, Japan) microscope. The electron microscope was coupled with an Aztec X-Max 1160 EDX detector (Oxford Instruments).

UV-VIS spectroscopy was employed to characterize the influence of the dopants on the optical properties of the $ZrO_2$ ceramics. DRS spectra were registered with a double-beam JASCO V-650 (Japan) spectrophotometer, equipped with an ISV-722 Integrating Sphere, in the wavelength range from 200 to 800 nm, with a scan rate of 400 nm/min.

## ACKNOWLEDGMENTS

Authors gratefully acknowledge Assoc. Prof. Lucian Barbu-Tudoran for SEM/EDS measurements.

## REFERENCES

1. A.K. Chitoria; A. Mir; M.A. Shah; *Ceram. Int.,* **2023,** 49, 32343-32358.
2. L. Bizo, M; Mureşan-Pop; R. Barabás; L. Barbu-Tudoran; A. Berar; *Materials,* **2023**, *16*, 2680.

3. D. Yusuf; E. Maryani; D.F. Mardhian; A.R. Noviyanti; Molecules, **2023,** *28*, 6054.
4. K. Wahyudi; E. Maryani; F. Arifiadi; A. Rostika; D. Yusuf; R.J. Manullang, Suyanti; R. Septawendar; *Mater. Res. Express,* **2021,** *8*, 045022.
5. J. Cho; B. Yang; C. Shen; H. Wang; X. Zhang; *J. Eur. Ceram.*, **2023**, *43*, 3, 1098-1107.
6. J. Wang; D. Chu; H. Ma; S. Fang; Q. Chen; B. Liu; G. Ji; Z. Zhang; X. Jia; *Ceram. Int.*, **2021**, *47*, 15180-15185.
7. L. Zhao; S. Yao; L. Kang; H.Y. Sun; Q. Huang; *Sci. Adv. Mater.*, **2019**, *11*, 4, 483-488.
8. L. Hwanseok; J. Kanghee; L. Heesoo; *J. Surf. Sci. Eng*. **2021**, *6*, 38.
9. M.V. Peirani; E. Brandaleze; *Sch. J. Eng. Technol.* **2017**, *5,* 280-289.
10. Y.T. Sung; J.H. Son; S.S. Lee; D.S. Bae; *Korean J. Mater. Res.,* **2014**, *24*, 53-59.
11. A.A. Ali; S.A. Shama; A.S. Amin; S.R. EL-Sayed; *Mat. Sci. Eng. B*, **2021,** 269, 115167.
12. J. K. Mbae; Z.W. Muthui; *Helyon*, **2023,** *9*, e20998.
13. S.R. Gul; M. Khan; Y. Zeng; M. Lin; B. Wu; C.-T. Tsai; *Materials,* **2018**, *19*, 1238.
14. A.L. Patterson; *Phys. Rev.*, **1939**, *56*, 978-982.
15. M.S. Khan; M.S. Islam; D.R. Bates; *J. Mater. Chem.,* **1998,** *8*, 2299-2307.
16. G. Balakrishnan; R. Velavan; K.M. Batoo; E.H. Raslan; *Results Phys.*, **2020,** *16*, 103013.
17. S. Sagadevan; J. Podder; I. Das; *J. Mater. Sci.: Mater. Electron.* **2016,** 27, 5622–5627.
18. A. Berar; M. Mureșan-Pop; L. Barbu-Tudoran; R. Barabás; L. Bizo; *Studia UBB Chemia*, **2020**, *LXV, 2,* 221-232.
19. P. Kubelka; F. Munk-Aussig; *Physik*, **1931**, *12*, 593-601.
20. L. Xie; J. Wang; Y. Hu; S. Zhu; Z. Zheng; S. Weng; P. Liu; *RSC Adv.,* **2012,** *2*, 9881-9886.
21. H.M. Shinde; T.T. Bhosale; N.L. Gavade; S.B. Babar; K.M. Garadkar; *J. Mater. Sc.i: Mater. Electron.,* **2018,** *29*, 14055-14064.
22. D. Sangalli; A. Lamperti; E. Cianci; R. Ciprian; M. Perego; A. Debernardi; *Phys. Rev. B*, **2013,** *87*, 085206.
23. N. Shuai; Z. Peng; X. Qian; L. Zhengcao; Z. Zhengjun; *J. Phys. D: Appl. Phys*., **2013,** *46*, 445004.
24. Y. Xie; Z. Ma; L. Liu; Y. Su; H. Zhao; Y. Liu; Z. Zhang; H. Duan; J. Li; E. Xie; *Appl. Phys. Lett.,* **2010,** *97*, 141916.
25. G. Lucovsky; C.L. Hinkle; C.C. Fulton; N.A. Stoute; H. Seo; J. Lüning; *Radiat. Phys. Chem.* **2006,** *75*, 2097-2101.
26. E. Gaggero; P. Calza; E. Cerrato; M.C. Paganini; *Catalysts*, **2021**, *11*, 1520.
27. P. Li; I.-W. Chen; J.E. Penner-Hahn; *J. Am. Ceram. Soc.* **1994,** *77*, 1281-1288.
28. S.Y. Kwon; I.H. Jung; *J. Eur. Ceram. Soc.*, **2017,** *37*, 1105-1116.

STUDIA UBB CHEMIA, LXIX, 2, 2024 (p. 19-36)
(RECOMMENDED CITATION)
DOI:10.24193/subbchem.2024.2.02

# THERMAL AND SPECTROSCOPIC INVESTIGATIONS OF COMPLEXES OF THE SELECTED TRANSITION METAL IONS WITH A *β*-L-ASPARTYL AMIDE DERIVATIVE

**Carmen SACALIS[a,*], Igballe ABDIJI[b], Maria DAVID[c], Ahmed JASHARI[b]**

**ABSTRACT.** The aim of the presented research was to synthesize and characterize *via* elemental analysis, HRMS, thermogravimetric analysis, FTIR and EPR a novel series of transition metal complexes of Cu(II), Co(II), Ni(II) and Mn(II) with *β*-L-aspartyl-cyclohexyl amide as ligand. The HRMS recorded spectra confirm the obtaining of new compounds. The changes in the FTIR spectra of the metal complexes, compared to the ligand, support the complexation process. The thermal stability of the ligand and its metal complexes was discussed in the 20-800$^0$C temperature range, in air atmosphere. In all of the studied complexes, the aspartyl amide acts as a bidentate ligand, its coordination involving the carboxylate oxygen and the nitrogen atom belonging to the free amino group of the amino acid. Metal complexes are formed in the 1:2 (Metal:Ligand) ratio as found by the elemental analysis. Except the free ligand, all the metal complexes are hydrating with water molecules, and the thermal stability of these suggested whether the water molecules are inside or outside the coordination sphere. The shape of EPR spectrum for copper complex at room temperature suggests the presence of $CuN_2O_2$ monomeric species with a rhombic distortion around the metallic ion. The results indicate that their stability range obeys the Irving-Williams series.

***Keywords:*** *L-aspartic acid, aspartyl amide, metal complexes, thermal behavior, spectroscopic studies*

[a] *Babeş-Bolyai University, Faculty of Chemistry and Chemical Engineering, 11 Arany Janos Str., RO-400028, Cluj-Napoca, Romania*
[b] *University of Tetova, Faculty of Natural Sciences and Mathematics, Bldv.Ilinden, nn., 1200 Tetova, Republic of North Macedonia*
[c] *National Institute for Research and Development of Isotopic and Molecular Technologies, 67-103 Donath str. RO-400293, Cluj-Napoca, Romania*
** Corresponding author: carmen.sacalis@ubbcluj.ro*

## INTRODUCTION

L-aspartic acid is one of the 22 proteinogenic amino acids, that is used in the biosynthesis of proteins. It is a metabolite in the urea cycle and participates in gluconeogenesis. L-aspartic acid is a naturally-occurring amino acid and a component of the active center of some enzymes. Due to its biological importance L-aspartic acid or peptide containing aspartyl residue was chosen in a lot of complexation products [1-6].

Coordination compounds of amino acids, including aspartic acid, demonstrate an activity varying from marginal to significantly good antimicrobial properties. As a result of resistance to the drugs currently in use and the emergence of new diseases, there is a continuous need for the synthesis and identification of new compounds as potential antimicrobial agents. Metal complexes of aspartic acid with Cu(II), Co(II), Ni(II), Cd(II) or Mn(II) demonstrate antimicrobial activities against Gram-positive, Gram-negative bacteria or fungus [7].

Polymeric silver (I) complex with aspartic acid or asparagine showed a wide spectrum of antimicrobial activities against *E. coli, P. aeruginosa, B. subtilis, S. aureus, C. albicans and S. cerevisiae* [8].

L-aspartic acid contained in some biodegradable polyesters was tested as drug delivery in the cancer cell line with promises results [2].

Surfactants derived from amino and *α*-hydroxy acids were synthesized and tested for aquatic toxicity. Amide and ester derivatives of $C_{10}$-$C_{16}$ fatty acids with amino acids, including aspartic acid or *α*-hydroxy acids such as malic or citric acid, were synthetized and tested for potential aquatic toxicity using zebrafish larvae as experimental animals. The reported results indicated that all the surfactants derived from natural products can be classified as environmentally benign [9].

Mixed metal complexes of L-aspartic acid and *o*-phenanthroline with rare earth such as La(III), Eu(III), Tb(III), Dy(III) and Y(III) showed a strong inhibitory effect on *E.coli, S. aureus* and *C. albicans*, and a considerable destructive effect on cancer cells [10].

Recently, a theoretical study proposed the amino acids, including L-aspartic acid and L- asparagine, as a chelating agents to remove heavy metal cations like $Cd^{2+}$, $Cu^{2+}$, $Ni^{2+}$, $Hg^{2+}$, $Zn^{2+}$, $Mn^{2+}$ and $Fe^{3+}$ could represent a good way to reduce the metal pollution in soil and environments [11].

New macrocyclic ligand and its Mn(II) and Cu(II) nanocomplexes from macrocycles containing amide groups using L-aspartic acid and ethylene diamine was reported. The obtained results indicate that the complexes can act as a promising candidate as green emitting light materials in electroluminescent and optoelectronic devices. Antimicrobial studies showed that Cu(II) complex acts as an antimicrobial agent against fungal strains and Gram-positive or Gram-negative bacteria [12].

We previously reported the convenient preparation of *β*-L-aspartyl-cyclohexyl amide (Figure 1) as a potential ligand for transition metal complexes by an original method which involved 4 steps of synthesis, using *N*-carbethoxyphthalimide as protective amino reagent *via* a mild phthaloylation [13].

On the basis of the above results, we explored the synthesis, with thermal and spectroscopic investigations of Cu(II), Co(II), Ni(II) and Mn(II) and with aforementioned *β*-L-aspartyl amide as ligand. All these compounds were analyzed by spectral analysis (HRMS, FT-IR and EPR) and thermal studies. The results are in good agreement with the thermal stability range and obeys the Irving-Williams series [14].

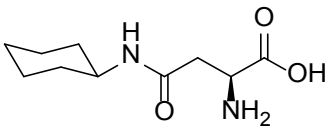


**Figure 1.** Structure formula of ligand (*S*)-2-amino-4-(cyclohexyl amino)-4-oxobutanoic acid (**HL**) or (**1**)

The objective of this study was to synthesize and analyze a new series of metal complexes of selected transition metal ions such as: Cu(II), Co(II), Ni(II), and Mn(II), using an aspartic acid amide as the organic ligand, previously prepared by our team, using a novel, more efficient method than those reported in the literature. Given that many drugs are administered in the form of metal complexes, we also conducted a study on their thermal behavior and stability upon heating, which could open new opportunities for testing these compounds in the medical field.

## RESULTS AND DISCUSSION

### *The structure of the metal complexes*

The complexation reaction of metal salts occurs in mild conditions and, in each case, yields a solid product. All the complexes are stable at room temperature. In our experiments, the metal complexes obtained as colored microcrystalline powder are characterized by elemental analysis, mass spectra, infrared spectral data, thermal studies and EPR data. Higher melting points of these products, as well their different colors when compared to that of the ligand, indicate the formation of metal complexes. Thermal analysis allowed us to evaluate the assumed position of crystallization water molecules in outer or inner spheres of complex coordination and determine the endo- or exothermic effects connected with each process such as dehydration, melting,

decarboxylation, fragmentation and finally pyrolysis of the organic rest. The EPR spectra gave us information about the local symmetry around the metal ions, especially in the case of the copper complex.

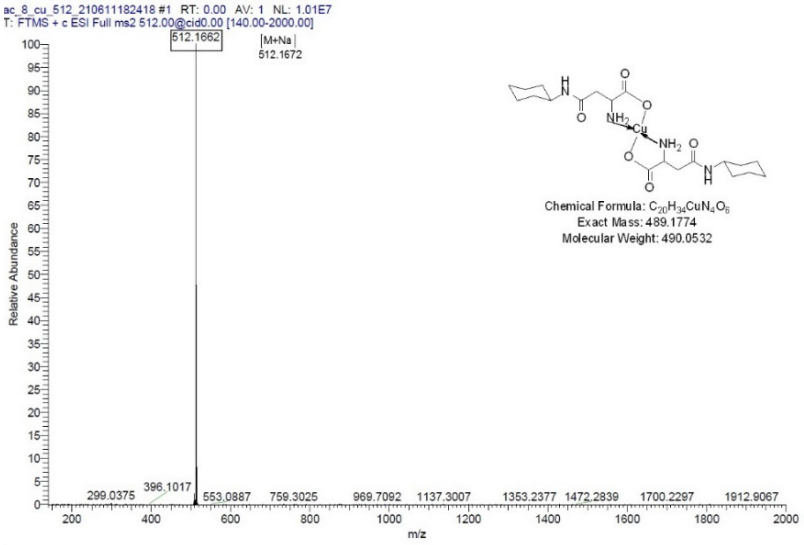


**Figure 2a.** HRMS spectrum (ESI) of copper complex (2)

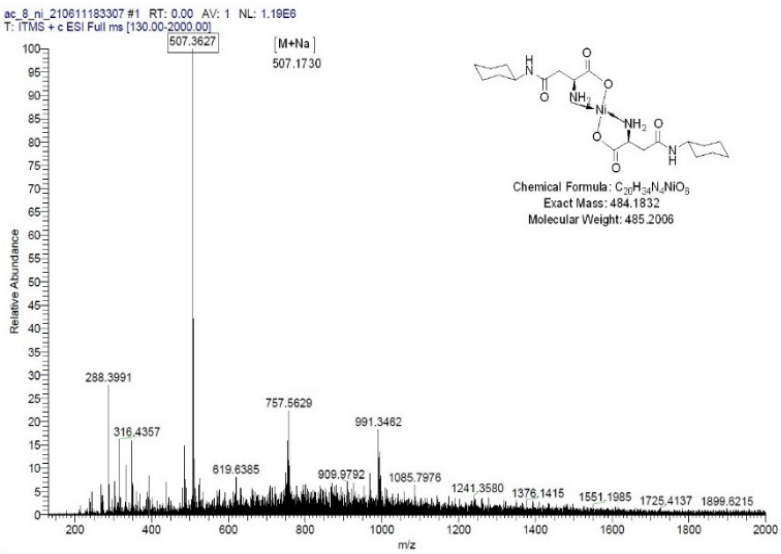


**Figure 2b.** HRMS spectrum (ESI) of nickel complex (4)

Another proof of the complexation is the HRMS spectrum for the metal complexes (Figure 2a-b). A peak of the highest intensity (100%), corresponding to the $[M+Na]^+$, supports the complexation idea with the transition metal ions, for each of the compounds.

Their elemental analysis data is in good agreement with the molar ratio Metal:Ligand=1:2, which indicates that the aspartyl amide acts as a bidentate ligand, its coordination involving the carboxyl group and the nitrogen atom belonging to the amino group of the aspartic acid fragment, fact also found in the case of other amino acid residues [7, 15-20]. As a result of elemental analysis, it was found that the ligand is anhydrous, but the metal complexes are hydrated, fact that is also confirmed by the thermal analysis data.

*Infrared spectra*

The FTIR spectra for the ligand and its metal complexes were recorded in the solid state in the wavenumber range of 400-4000$cm^{-1}$ with the aim of highlighting the $\nu_{(M-O)}$ and $\nu_{(M-N)}$ stretching vibrations, specific to metallic complexes. The IR spectra provide valuable information regarding the nature of the functional group attached to the metal atom.

Partial assignments of the IR absorption bands, observed for the free ligand and its transition metal complexes, are given in Table 1.

**Table 1.** Selected IR data ($cm^{-1}$) of the ligand (HL) and its metal complexes (2-5)

| Compound | $C_{10}H_{18}N_2O_3$ HL (1) | $C_{20}H_{36}CuN_4O_7$ $[Cu(L)_2]\cdot H_2O$ (2) | $C_{20}H_{38}CoN_4O_8$ $[Co(L)_2\cdot 2H_2O]$ (3) | $C_{20}H_{38}N_4NiO_8$ $[Ni(L)_2\cdot 2H_2O]$ (4) | $C_{20}H_{38}MnN_4O_8$ $[Mn(L)_2]\cdot 2H_2O$ (5) |
|---|---|---|---|---|---|
| $\nu$(O-H) | 3445(bb) | 3423(bb) | 3329(bb) | 3339(bb) | 3407(bb) |
| $\nu(NH_2)$ | 3296(s) | 3257(s) | 3297(s) | 3295(m) | signal covered by broadband |
| $\nu(CH_2$as) from cyclohexyl ring | 2930(vs) | 2930(vs) | 2930(s) | 2936(s) | 2927(w) |
| $\nu(CH_2$sym) from cyclohexyl ring | 2853(s) | 2854(m) | 2854(m) | 2854(m) | 2852(w) |
| $\nu(COO^-$as) | 1658(s) | 1651(vs) | 1650(vs) | 1650(s) | 1556(m) |
| $\delta$(NH) | 1620(vs) | 1589(vs) | 1622(vs) | 1573(vs) | 1526(s) |
| $\nu(COO^-$sym) | 1574(s) | 1561(vs) | 1558(vs) | 1588(s) | 1511(vs) |
| $\delta(CH_2)$ from cyclohexyl ring | 1429(vs) | 1405(m) | 1404(s) | 1418(m) | 1407(m) |
| $\nu$(NH) | 1310(m) | 1367(m) | 1389(m) | 1312(m) | 1373(vs) |
| $\nu$(M-N) | - | 588(m) | 531(m) | 562(m) | 457(w) |
| $\nu$(M-O) | - | 469(m) | 396(w) | 423(w) | 373(m) |

w: weak; m: medium; s: strong; vs: very strong; bb: broadband

The bonding of the ligand to different transition metal ions was investigated also by comparing the IR spectrum of the free ligand (1) with those of the metal complexes (2-5) (Figure 3).

In the spectral region of 3300-3450 $cm^{-1}$ a broadband formed by some overlapped bands is observed, that may be assigned to $\nu_{O-H}$ vibration due to intra- and intermolecular hydrogen bonding in the crystalline state. The broad envelope band with higher intensity in all those complexes could indicate the presence of weak hydrogen bonds that stabilize the structure of the metal compounds [16-17, 21].

For the ligand a smaller, but broad band at 3445 $cm^{-1}$ (Lit. [22], 3424$cm^{-1}$), was assigned to the *ν(O-H)* from carboxylic group [22-23]. The fact that the ligand is anhydrous can also be seen from the shape of the band which is smaller compared to the metal complexes. The intense board absorption band at 3339-3423 $cm^{-1}$ in the metal compounds indicates the presence of water molecules [24-25].

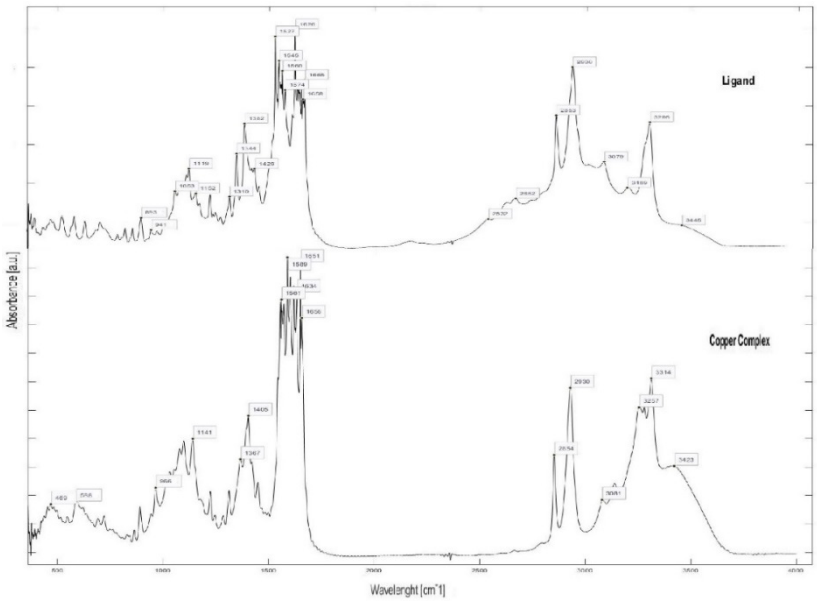


**Figure 3.** IR spectra of the ligand (1) and its copper complex (2)

The vibrational frequencies related to *ν(COO⁻as)* at 1658 $cm^{-1}$ (Lit. [26] at 1658 $cm^{-1}$ and Lit. [22] at 1637 $cm^{-1}$) and *ν(COO⁻sym)* at 1574 $cm^{-1}$ (Lit. [26] at 1570 $cm^{-1}$ and Lit. [22] at 1598 $cm^{-1}$) in ligand, is shifted toward lower value in the IR spectra of the compounds (2-5) after complexation. Also, the $\nu(NH_2)$ and *δ(NH)* frequencies in the metal complexes were shifted to lower value due to chelating with metal ions [7, 27].

The *v(CH₂as)* and *v(CH₂sym)* corresponding to the cyclohexyl ring keep roughly the same value. New bands in the spectra of the transition metal complexes at 457-588 $cm^{-1}$ were assigned to *v(M-N)* stretching frequencies. The participation of the lone pair of electrons on the N of the amino group in the ligand in coordination is supported by these bands. On the other hand, the bands in the region of 373-469 $cm^{-1}$ indicate the formation of M-O bond as a result of the coordination of the ligand to the central metal ions *via* the oxygen atom of the carboxylate rest. This band was assigned to *v(M-O)* stretching frequencies, as similar to other metal complexes [7,12, 27-30].

The *v(M-N)* and *v(M-O)* stretching bands are shifted progressively to higher frequencies as the metal is changed in the order:

*Mn(II) < Co(II) < Ni(II) < Cu(II)*

in good agreement with Nakamoto predictions for the amino acid complexes [27]. The shifts are dependent on the metal ions and the magnitudes of shifts follow the Irving-Williams series [14].

*Thermal analysis*

The thermal behavior of the ligand and its metal complexes was performed in air atmosphere in order to study the nature of water in the investigated compounds, their thermal stability, as well as decomposition modes under controlled heating rate. The analysis of the thermogravimetric curves demonstrates that, both for the ligand as well as for the metal compounds, they undergo gradual decomposition as the temperature increases.

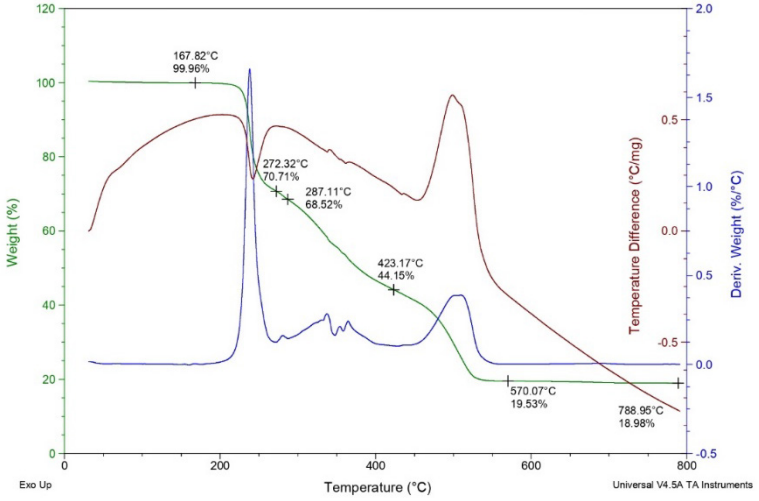


**Figure 4a.** TG-DTG-DTA diagram for the ligand (1)

The thermal behavior of the ligand (HL) or (1) and its metal complexes (2-5) are summarized in Table 2 and Figure 4a-e.

Thermal decomposition of the ligand (1) was achieved in three stages. The thermal analysis data, in good agreement with those of the elemental analysis, indicate that the ligand is anhydrous, so the small endothermic peak at 168$^0$C on DTA curve and a mass loss of only 0.04% corresponds to the water present in the air atmosphere. An endothermic peak at 231$^0$C and an exothermic peak at 272$^0$C was associated with a melting with decomposition.

The decarboxylation of the amino acid rest and degradation of the free amino group, with loss of a fragment (-$CH_3O_2N$) probably occurs in this stage. The experimental mass loss is 29.25%, close value to the calculated data of 28.48%. This violent burning process of the organic rest, as seen in the DTG curve, is generally specific to compounds with a high oxygen and nitrogen content [19, 31]. The second stage of decomposition occurs within the temperature range of 278-423$^0$C, being accompanied by a large board on DTA curve. Three exothermic peaks at 339$^0$C, 356$^0$C and 371$^0$C, respectively with an experimental mass loss of 24.37% (calcd. 25.69%) can be noted in this stage. It is expected to take place a new fragmentation of the organic rest, at the amidic bond and loss of a -$C_3H_4O$ radical. The last stage begins at 423$^0$C and is associated with a continuous degradation of the sample. The maximum mass loss for the three stages is at 489$^0$C. As can be seen in the Figure 4a, the organic compound is completely pyrolyzed until 570$^0$C, finally some ash remaining in the crucible.

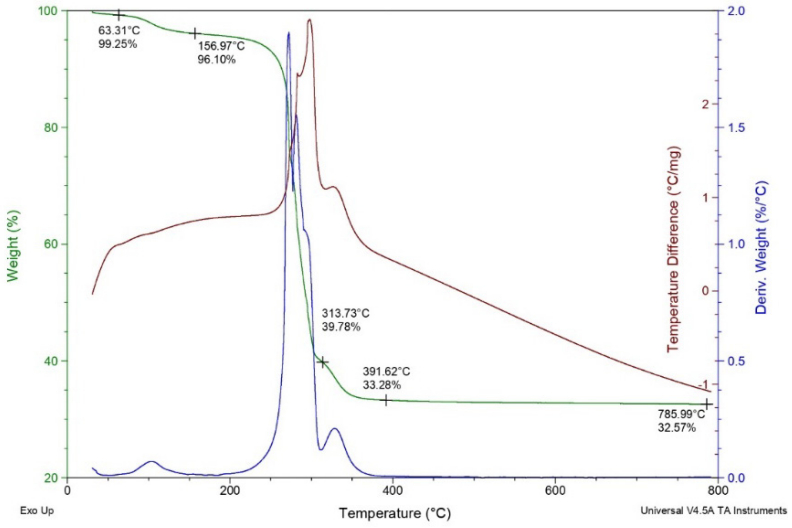


**Figure 4b.** TG-DTG-DTA diagram for the copper complex (2)

The aim of the thermal analysis of the metal complexes is to obtain information concerning their thermal stability and to decide whether the water molecules are inside or outside the coordination sphere [17-19].

For the thermal investigation of copper complex, a sample of 3.5790 mg was taken (Figure 4b). When heated, the complex starts to decompose at $104^0$C and loses one water molecule outside coordination sphere in the temperature range of 20-$186^0$C. This phenomenon is connected with an endothermic peak and a mass loss of 3.15% (calcd. 3.54%). The first endothermic peak at $63^0$C can be assigned to the moisture in the air and inside pores of the substance. In the second step, the metal complex is releasing partially organic ligand with a strong exothermic effect and a great mass loss of 56.32% (calcd. 58.13%). Three exothermic peaks at $271^0$C, $279^0$C and $296^0$C respectively, confirm this fragmentation process. Probably decarboxylation, the amidic split and the amino group degradation accompanies this step. The violent decomposition of the anhydrous complex is often encountered in the case of copper complexes [24]. The third-stage decomposition takes place at 307-$400^0$C with a small exothermic peak at $392^0$C, corresponding to the pyrolysis of organic rest and formation, ultimately, of CuO.

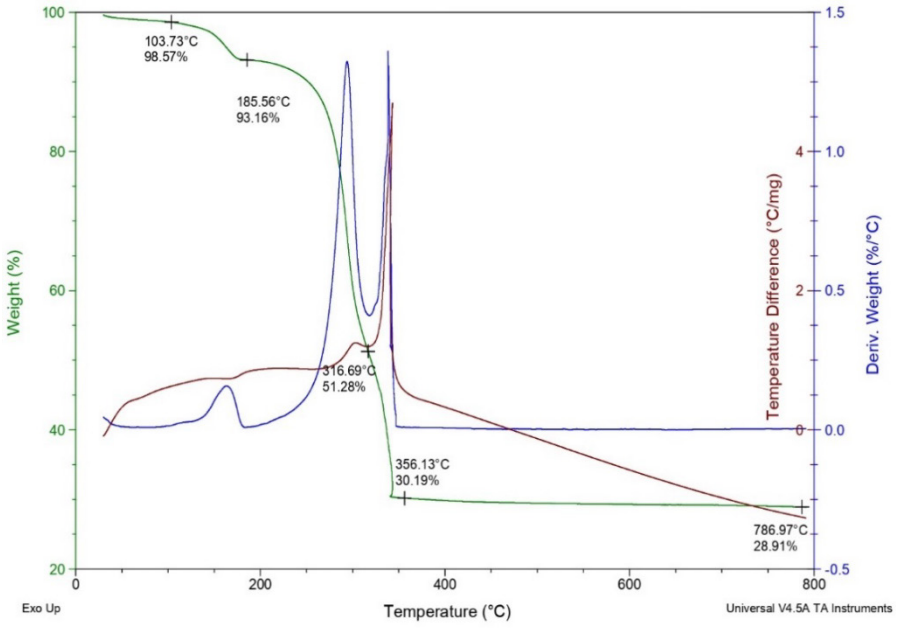


**Figure 4c.** TG-DTG-DTA diagram for the cobalt complex (3)

The thermal decomposition of the cobalt complex also occurs in three stages (Figure 4c). The first stage decomposition starts in the temperature range of 20-186$^0$C, with a mass loss of 6.84% (calcd. 6.90%), which corresponds to the loss of 2 mole of water. The higher temperature, 164$^0$C, is an indication that the water is inside the coordination sphere of the metal complex.

**Table 2.** Thermo-gravimetric data of the ligand (HL) and its metal complexes (2-5)

| Compd. | Stage | Heat effect on DTA | Temperature ($^0$C) | | | Mass loss (%) | | Assignment |
|---|---|---|---|---|---|---|---|---|
| | | | $T_i$ | $T_{max}$ | $T_f$ | Calcd. | Experim. | |
| HL | I | Endo | 20 | 168 | 278 | - | 0.04 | -residual water |
| (1) | | Endo | | 231 | | | | |
| | | Exo | | 272 | | 28.48 | 29.25 | -melting with decomp. |
| | II | Exo | 278 | 339 | 423 | | | -fragmentation the organic |
| | | Exo | | 356 | | | | rest at the amidic bond |
| | | Exo | | 371 | | 25.69 | 24.37 | -pyrolysis of organic rest |
| | III | Exo | 423 | 489 | 570 | | | -ash residue |
| | | Exo | | 570 | | | 26.81 | |
| | | | | | | 45.83 | 19.53 | |
| $[Cu(L)_2]\bullet H_2O$ | I | Endo | 20 | 63 | 186 | - | 0.75 | -residual water |
| (2) | | Endo | | 104 | | 3.54 | 3.15 | -1 mole of water |
| | II | Exo | 186 | 271 | 307 | | | - fragmentation the organic |
| | | Exo | | 279 | | | | rest |
| | | Exo | | 296 | | 58.13 | 56.32 | |
| | III | Exo | 307 | 392 | 400 | | 6.50 | -pyrolysis of organic rest |
| | | | | | | 38.33 | 33.28 | ash and CuO residue |
| $[Co(L)_2\bullet 2H_2O]$ | I | Endo | 20 | 32 | 186 | - | 1.43 | -residual water |
| (3) | | Endo | | 164 | | 6.90 | 5.41 | -2 mole of water |
| | II | Endo | 186 | 275 | 317 | - | - | -melting point with decompose |
| | | Exo | | 303 | | 42.90 | 41.88 | -decomp. of ligand |
| | III | Exo | 317 | 356 | 400 | 29.93 | 30.19 | pyrolysis of organic rest |
| | | | | | | | | -ash and CoO |
| | | | | | | 20.27 | 21.09 | |
| $[Ni(L)_2\bullet 2H_2O]$ | I | Endo | 20 | 175 | 284 | 6.91 | 6.88 | -2 mole of water |
| (4) | II | Exo | 284 | 360 | 392 | 66.96 | 65.79 | -total pyrolysis of metal complex |
| | | | | | | 26.13 | 27.33 | -ash and NiO |
| $[Mn(L)_2\bullet 2H_2O$ | I | Endo | 20 | 97 | 191 | 6.96 | 6.69 | -2 mole of water |
| (5) | II | Exo | 191 | 243 | 371 | | 3.40 | -gradually decomposition |
| | | Exo | | 354 | | | 14.99 | of organic rest |
| | III | Exo | 371 | 389 | 475 | 24.93 | 7.2 | |
| | IV | Exo | 475 | 532 | 768 | | 3.01 | |
| | | Exo | | 643 | | | 1.22 | |
| | | | | | | 39.18 | 36.51 | |
| | | | | | | 28.93 | 26.98 | -ash and MnO |

The second stage of decomposition was observed in the 186-317$^0$C range. A small endothermic peak at 275$^0$C can be assigned to the melting point with decompose, and an exothermic peak at 303$^0$C, with an experimental mass loss of 42.90% (calcd. 41.88%), corresponds to cleavage of amidic bond followed by possible decarboxylation and oxidation processes of organic fragments. The third stage decomposition takes place at 317-400$^0$C and highlights the rapid and progressive degradation of the organic residue until the metal oxide is obtained. The final products are CoO and some ash (20.27%, calcd. 21.09%).

Thermal decomposition of the nickel complex proceeds in two stages between 20-284$^0$C and 284-392$^0$C respectively (Figure 4d). First stage, with an endothermic peak at 175$^0$C, corresponds to the loss of water molecules inside the coordination sphere of the metal complexes. This phenomenon was achieved with an experimental mass loss of 6.67% (calcd. 6.91%). A strong exothermic effect was assigned to the total pyrolysis of metal complexes, a fact also found in the case of other metal complexes of amino acids or compounds with high percent of nitrogen [19, 32]. The final product is NiO and ash like the other metal complexes.

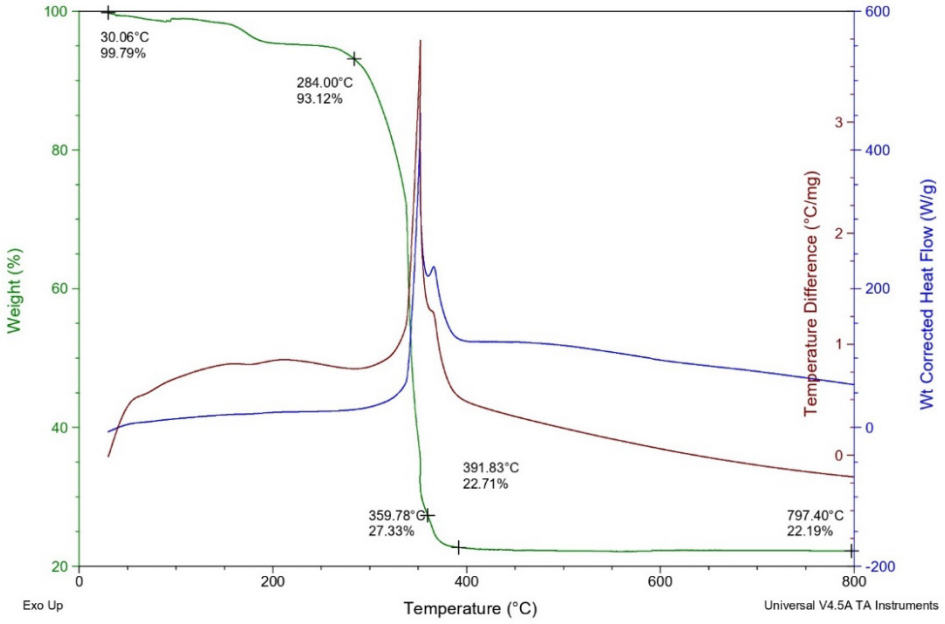


**Figure 4d.** TG-DTG-DTA diagram for the nickel complex (4)

The thermogram of manganese complex indicated four decomposition steps, occurred slowly like other Mn(II) complexes [23]. The first decomposition step, at temperature range 20-191$^0$C with an endothermic peak at 97$^0$C, corresponds to loss of water molecules outside of coordination sphere of complexes. The next three stages at temperature range 191-371$^0$C, 371-475$^0$C and 475-768$^0$C respectively, accompanied by exothermic peaks indicated the gradually decomposition of metal complex. The decomposition of the compound takes place progressively (Figure 4e), being probably accompanied by the breaking of the amidic bond, the destruction of the rest of the amine, oxidation or decarboxylation of the organic fragments leaving MnO and ash as a residue.

The decomposition of the compounds was not complete and the residue from 26.98% to 33.28% was observed, containing ash and metal oxide similarly to other compound with high nitrogen [17, 19, 32].

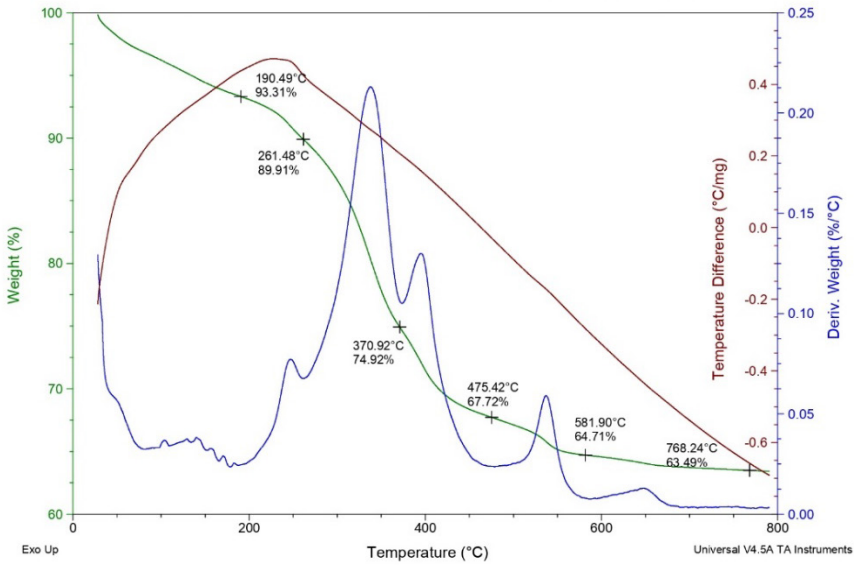


**Figure 4e.** TG-DTG-DTA diagram for the manganese complex (5)

*EPR data*

The EPR data are recorded at room temperature, in solid state, but just the cooper and manganese complexes provided relevant information, about the local symmetry found in compounds as a result of complexation. The experimental results are associated with the occurrence of paramagnetic Cu(II) for the compound (1).

The EPR spectrum of copper complex at room temperature, suggests the presence of $CuN_2O_2$ monomeric species. The shape of the spectrum corresponds to a S=1/2 system with rhombic **g** tensors. The principal values of **g** tensors ($g_1$=2.197, $g_2$=2.147 and $g_3$=2.051) indicate a rhombic distortion around the metallic ion (Figure 5).

The powder EPR spectrum of manganese complex is characterized by a quasi-isotropic **g** tensor ($\Delta B_{pp} \approx 400$ G) with the principal value g=2.074 due to the spin value of the $CuN_2O_2$ monomeric species [33-35].

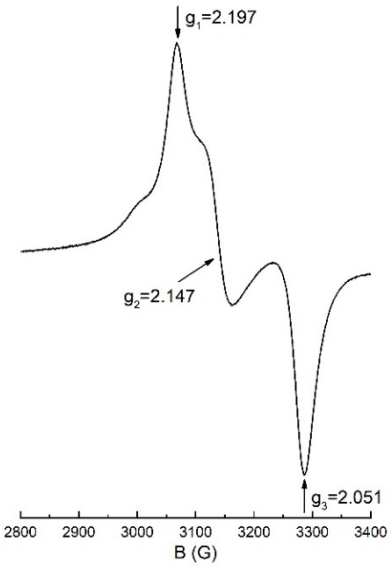


**Figure 5.** EPR spectrum of copper complex (2)

## CONCLUSIONS

In this paper, we presented the syntheses and investigations of new transition metal complexes using *β*-L-aspartyl-cyclohexyl amide as ligand.

Elemental and thermal analysis lead to the idea that the ligand is anhydrous, but its metal complexes are hydrating. This phenomenon can be explained by the working conditions, in aqueous solutions, for the synthesis of metal complexes. The cooper and manganese complexes are hydrated with water molecules outside the coordination sphere, but for the cobalt and nickel complexes the water molecules are located inside the coordination sphere.

On the other hand, the *v(M-N)* and *v(M-O)* stretching bands in the metal complexes IR spectra support the complexation idea. The thermal stability of selected *3d* transition metal complexes indicated that all the compounds decompose in multistage in the temperature domain 20-800$^0$C.

For the cooper complex the EPR data indicates a rhombic distortion around the metallic ion.

The aspartyl amide acts as a bidentate ligand in all the metal complexes, coordination involving the carboxylate oxygen and the nitrogen atom belonging to the free amino group of the amino acid.

Based on thermal and spectroscopic data, it was found that metal complexes stability:

$$[Mn(L)_2]\bullet 2H_2O < [Co(L)_2\bullet 2H_2O] < [Ni(L)_2\bullet 2H_2O] < [Cu(L)_2]\bullet H_2O$$

obeys the Irving-Williams series [14,17,19].

The obtained data allows us to propose the following structural formulas for the studied transition metal complexes (Figure 6).

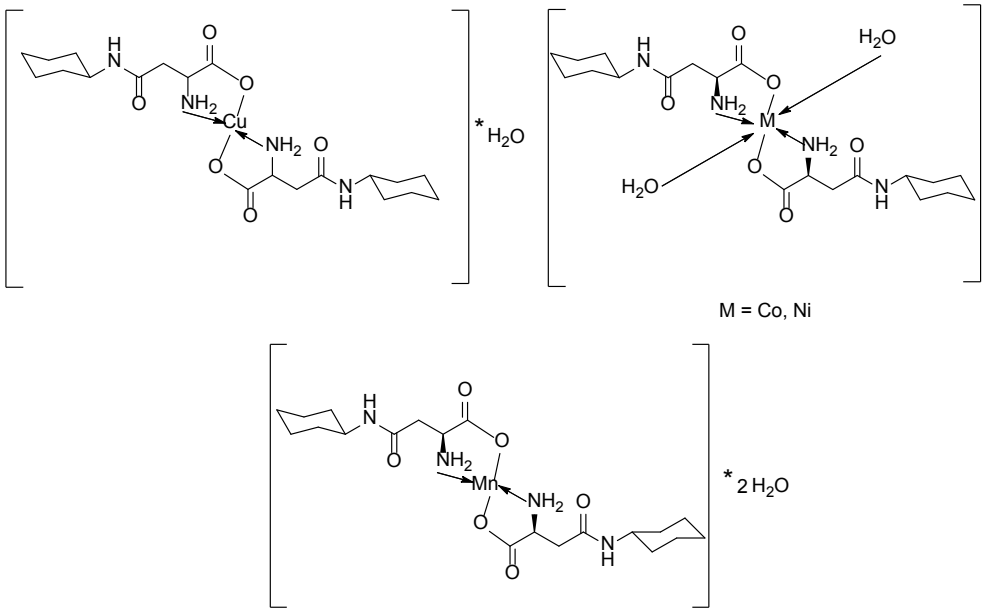


**Figure 6.** Suggested structures for the metal complexes

Since studies conducted with numerous organic ligands containing nitrogen and oxygen donor systems have demonstrated their antimicrobial activities or enzyme production inhibition, we propose that in the future, the new metal complexes synthesized by our team could be tested and find applications in

the medical field. Thermal analysis data have shown that the highest thermal stability is found in the case of the copper complex. On the other hand, the role of copper in numerous metabolic activities is well known, which could lead to promising results. Additionally, nickel, cobalt, and manganese are trace elements present in many biological systems, suggesting that their testing in the medical field should not be overlooked.

## EXPERIMENTAL SECTION

### *Material and instrumentation*

All reagents and chemicals were purchased from commercial sources and used as received. Melting points were measured on an ELECTROTHERMAL® instrument and were not corrected. CHNS analyses were determined on an elemental micro-analyzer Elementar vario MICRO Cube. Mass spectra were carried out on a LTQ ORBITRAP® XL (Thermo Scientific) instrument which was externally calibrated using the manufacturer's APCI or ESI(+) calibration mix. The samples were introduced into the spectrometer by direct infusion. IR spectra were recorded in KBr pellets on a JASCO® FT-IR 6200 Spectrometer which operates with $4cm^{-1}$ resolution. Thermogravimetry and differential thermal analysis (TG-DTG-DTA) curves were recorded with a Thermal Analyzer TA Instruments SDT Q600 V20.9 Build 20 on an interval of 20-800$^0$C, at a heating rate of 10$^0$C/min, in alumina crucibles and a dynamic air atmosphere. The ESR measurements were carried out on a Bruker Biospin EMX$^{micro}$ spectrometer operating at X-band (9-10 GHz) with continuous wave at X-band (≈9 GHz). The spectra were recorded at room temperature with a microwave frequency of 9.4353 GHz, microwave power of 2 mW, modulation frequency of 100 kHz, modulation amplitude of 2 G.

### *General procedure for the synthesis of the metal complexes*

The ligand namely (*S*)-2-amino-4-(cyclohexyl amino)-4-oxobutanoic acid (1 or HL) was prepared *via* a mild phthaloylation using the amide bond formation protocol [13].

Cu(II), Co(II), Ni(II) and Mn(II) complexes of the ligand were prepared by following a general method. The metal salt [$CuSO_4$•$5H_2O$, $CoSO_4$•$7H_2O$, $NiSO_4$•$7H_2O$ and $MnSO_4$•$4H_2O$] (1.30mmol) was dissolved in 7-8mL distilled water. The ligand (2mmol) was solved in a solution of $Na_2CO_3$ 1M until pH = 11.0 – 11.5. To a solution of solved ligand was slowly added, continuously stirring, dropwise during 40 min., the solution of the metal salt at room temperature.

By adding the solution of metal ions, immediate color change was observed to the ligand solution, depending on the metal ion. The mixture was let to stir at the room temperature about 12h to perform the reaction. The final pH changed to 7.5-8.5 for all the compounds. The isolated solid complexes were obtained by vacuum filtration, washed with distilled water and finally dried in a vacuum desiccator for 72h.

Finally, the obtained compounds were subjected to elemental, spectroscopic and thermal investigations.

$C_{10}H_{18}N_2O_3$ (1 or HL): White solid; MW=214.2651; Mp=231-233$^0$C; Elemental Analysis(%) Calcd.(Found) C: 56.06(56.81), H: 8.47(8.11); N: 13.07(12.88); MS (ESI, $CH_3OH$) [M+H]: 215.2693; Exact Mass: 214.1317; FTIR (KBr,cm$^{-1}$): $\nu_{max}$: 3445, 3296, 2930, 2853, 1658, 1620, 1574, 1429, 1310; Thermal Analysis: $T_{max}$: 168$^0$C (Endo) ($TG_{exp}$=0.04%), 231$^0$C (Endo) and 272$^0$C (Exo) ($TG_{calcd}$=28.48%, $TG_{exp}$=29.25%, 339$^0$C (Exo), 356$^0$C (Exo) and 371$^0$C (Exo) ($TG_{calcd}$=25.69%, $TG_{exp}$=24.37%), 489$^0$C (Exo) and 570$^0$C (Exo) ($TG_{calcd}$=45.83%, $TG_{exp}$=46.34%), residue 45.83% (calcd) 46.43 (exp).

$C_{20}H_{36}CuN_4O_7$ (2): Pale-blue solid; MW=508.0684; Mp=312-314$^0$C (decomp.); Yield: 82%; Elemental Analysis(%) Calc.(Found) C: 47.28(47.98), H: 7.14(6.91), N: 11.03(11.29); MS (ESI, $CH_3OH$, without coordination water) [M+Na]: 512.1662; Exact Mass: 489.1774; FTIR (KBr,cm$^{-1}$): $\nu_{max}$: 3423, 3257, 2930, 2854, 1651, 1589, 1561, 1405, 1367, 588, 469; Thermal Analysis: $T_{max}$: 63$^0$C (Endo) ($TG_{exp.}$=0.75%), 104$^0$C (Endo) ($TG_{calcd}$=3.54%, $TG_{exp}$=3.15%), 271$^0$C (Exo), 279$^0$C (Exo) and 296$^0$C (Exo) ($TG_{calcd}$=58.13%, $TG_{exp}$=56.32%), 392$^0$C (Exo) ($TG_{calcd.}$=38.33%, $TG_{exp}$=39.78%), residue 38.33% (calcd) 39.78 (exp); EPR: ($g_1$=2.179, $g_2$=2.147, $g_3$=2.051); Molar Ratio Cu : L : $H_2O$ = 1 : 2 : 1.

$C_{20}H_{38}CoN_4O_8$ (3): Pale-pink solid; MW=521.4709; Mp=273-275$^0$C (decomp.); Yield: 76%; Elemental Analysis(%) Calc.(Found) C: 46.06(46.78), H: 7.34(7.92), N: 10.74(11.03); MS (ESI, $CH_3OH$, without coordination water) [M+Na]: 508.1708; Exact Mass: 485.1810; FTIR (KBr,cm$^{-1}$): $\nu_{max}$: 3329, 3297, 2930, 2854, 1650, 1622, 1558, 1404, 1389, 531, 396; Thermal Analysis: $T_{max}$: 32$^0$C (Endo) ($TG_{exp}$=1.43%) 164$^0$C (Endo) ($TG_{calcd}$=6.90%, $TG_{exp}$=5.41%), 275$^0$C (Endo) (m.p.), 303$^0$C (Exo) ($TG_{calcd}$=42.90%, $TG_{exp}$=41.88%), 356$^0$C (Exo) ($TG_{calcd}$=29.93%, $TG_{exp}$=30.19%), residue 20.27% (calcd) 21.09% (exp); Molar Ratio Co : L : $H_2O$ = 1 : 2 : 2.

$C_{20}H_{38}N_4NiO_8$ (4): Greenish-white solid; MW=521.2311; Mp=291-293$^0$C (decomp.); Yield: 76%; Elemental Analysis(%) Calc.(Found) C: 46.09(46.67), H: 7.35(7.78), N: 10.75(10.18); MS (ESI, $CH_3OH$, without coordination water) [M+Na]: 507.3627; Exact Mass: 484.1832; FTIR (KBr,cm$^{-1}$): $\nu_{max}$: 3339, 3295,

2936, 2854, 1650, 1573, 1588, 1418, 1312, 562, 423; Thermal Analysis: $T_{max}$: 175$^0$C (Endo) ($TG_{calcd}$=6.91%, $TG_{exp}$=6.88%), 360$^0$C (Exo) ($TG_{calcd}$=66.96%, $TG_{exp}$=65.79%), residue 26.13% (calcd) 27.33% (exp); Molar Ratio Ni : L : $H_2O$ = 1 : 2 : 2.

$C_{20}H_{38}MnN_4O_8$ (5): Light-brown solid; MW 517.4758; Mp=238-240$^0$C (decomp.); Yield: 48%; Elemental Analysis(%) Calc.(Found) C: 46.42(45.93), H: 7.40(7.81), N: 10.83(11.04); MS (ESI, $CH_3OH$, without coordination water) [M+Na]: 504.3594; Exact Mass: 517.2070; FTIR (KBr,cm$^{-1}$): $\nu_{max}$: 3407, 2927, 2852, 1556, 1526, 1511, 1407, 1373, 457, 373; Thermal Analysis: $T_{max}$:97$^0$C (Endo) ($TG_{calcd}$=6.96%, $TG_{exp}$=6.69%), 243$^0$C (Exo), 354$^0$C (Exo) and 389$^0$C (Exo) ($TG_{calcd}$=24.93%, $TG_{exp}$=25.59%), 532$^0$C (Exo) and 643$^0$C (Exo) ($TG_{calcd}$=39.18%, $TG_{exp}$=36.51%), residue 28.93% (calcd) 26.98% (exp); EPR: g=2.07; Molar Ratio Mn : L : $H_2O$ = 1 : 2 : 2.

## REFERENCES


1. Y. M. Jamil; M. A. Al-Maqtari; F. M. Al-Azab; M. K. Al-Qadasy; A. A. Al-Gaadbi; *Eclet. Quim.,* **2018**, *43*(4), 11-24
2. M. Khuddus; M. Jayakannan; *Biomacromolecules*, **2023**, *24*, 2643-2660
3. Miller; A. Matera-Witkiewicz; A. Mikolajczyk; J. Watly; D. Wilcox, D. Witkowska; M. Rowinska-Zyrek; *Int. J. Mol. Sci.,* **2021**, *22*, 6971
4. Tomashevskii; O. A. Golovanova; S. V. Anisina; *Russ. J. Gen. Chem.,* **2021**, *91*(12), 2621-2626
5. N. Lihi; M. Lukacs; D. Szucs; K. Varnagy; I. Sovago; *Polyhedron*., **2017**, *133*, 364-373
6. M. Raics; D. Sanna; I. Sovago; C. Kallay; *Inorganica Chim. Acta*., **2015**, *426*, 99-106
7. T. O. Aiyelabola; D. A. Isabirye; E. O. Akinkunmi; O. A. Ogunkunle; I. A. O. Ojo; *J. Chem.,* **2016**, Article ID 7317015, https://doi.org/10.1155/2016/7317015
8. Nomiya; H. Yokoyama; *J. Chem.Soc., Dalton Trans*., **2002**, *12*, 2483-2490
9. D. Kalebic; K. Binnemans; P. A. M. de Witte; W. Dehaen; *RSC Sustainability,* **2023**, *1*, 1995-2005
10. Y. Hui; H. Qizhuang; Z. Meifeng; X. Yanming; S. Jingyi; *J. Chin. Rare Earth Soc.,* **2007**, *2*, 150-156
11. X. Liu; M. Wu; C. Li; P. Yu; S. Feng; Y. Li; Q. Zhang; *Molecules*, **2022**, *27,* 2407
12. M. Patyal; K. Kaur; N. Gupta; R. Kaur; A. K. Malik; *Prot. Met. Phys. Chem.*, **2023**, *59(2)*, 169-178
13. I. Abdiji; C. Sacalis; A. Shabani; A. Jashari; *J. Nat. Sci. Math.*, **2023**, *8(15-16)*, 72-81
14. H. Irving; R. J. P. Williams; *J. Chem. Soc.*, **1953**, 3192-3210

15. I. Sovago; E. Farkas; C. Bertalan; A. Lebkiri; T. Kowalik-Jankowska; H. Kozlowski; *J. Inorg. Biochem.*, **1993**, *51,* 715-726
16. L. Zapala; M. Kosinska; E. Woznicka; L. Byczynski; W. Zapala; *J. Therm. Anal. Calorim.*, **2016**, *124*, 363-374
17. C. Sacalis; F. Goga; C. Somesan; *Studia UBB Chemia*, **2018**, *63(4)*, 51-63
18. C. Sacalis; F. Goga; L. David; *Studia UBB Chemia*, **2017**, *62(4),* 181-192
19. C. Sacalis; S. Jahiji, A. Avram; *Studia UBB Chemia*, **2022**, *67(4)*, 337-352
20. M. Castillo; E. Ramirez; *Transit. Met. Chem.*, **1984**, *9*, 268-270
21. Z. K. Genc; S. Selcuk; S. Sandal; N. Colak; S. Keser; M. Sekerci; M. Karatepe; *Med. Chem. Res.*, **2014**, *23*, 2476-2485
22. P. S. Piispanen; P. M. Pihko; *Tetrahedron Lett.*, **2005**, *46*, 2751-2755
23. A. M. Hassan; B. H. Heakal; A. O. Said; W. M. Aboulthana; M. A. Abdelmoaz; *Egypt. J. Chem.*, **2020**, *63(7)*, 2533-2550
24. W. Ferenc; B. Cristovao; J. Sarzynski; P. Sadowski; *J. Therm. Anal. Calorim.*, **2012**, *110*, 739-748
25. I. Sakiyan; *Transit. Met. Chem.*, **2007**, *32*, 131-135
26. M. Tanaka; I. Yamashina; *Carbohydr. Res.*, **1973**, *27,* 175-183
27. K. Nakamoto; *Infrared and Raman Spectra of Inorganic and Coordination Compounds*, *Part. B: Applications in Coordination, Organometallic and Bioinorganic Chemistry*, John Wiley & Sons, Inc., Hoboken, New Jersey, Sixth Ed., **2009**, pp. 63-72
28. A. A. Osunlaja; N. P. Ndahil; J. A. Ameh; *Afr. J. Biotechnol.*, **2009**, *8(1)*, 4-11
29. O. F. Akinyele; A. B. Adesina; T. A. Ajayeoba; E. G. Fakola; *Sci. J. Chem.,* **2023**, *11(4)*, 137-145
30. T. H. Al-Noor; M. R. Aziz; A. T. AL-Jeboori; *J. Chem. Pharm. Res.*, **2014**, *6(4)*, 1225-1231
31. C. A. Terraza; L. H. Tagle; D. Munoz; A. Tundidor-Camba; P. A. Ortiz; D. Coll; C. M. Gonzalez-Henriquez; I. A. Jessop; *Polym. Bull.*, **2016**, *73*, 1103-1117
32. M. Worzakowska; M. Sztanke; K. Sztanke; *J. Therm. Anal. Calorim.,* **2022**, *147*, 14315-14327
33. L. D. Pinto; P. A. L. Puppin; V. M. Behring; D. H. Flinker; A. L. R. Merce; A. S. Mangrich; N. A. Rey; J. Felcman; *Inorganica Chim. Acta*, **2010**, *363*, 2624-2630
34. J. R. Pilbrow, *Transition ion electron paramagnetic resonance,* Clarendon Press, New York: Oxford University Press, **1990**, pp. 51-80
35. F. E. Mabbs; D. Collison; *Electron Paramagnetic Resonance of d Transition Metal Compounds,* Elsevier Science Publishers B.V. Amsterdam, Netherland, **2013**, pp. 83-124.

STUDIA UBB CHEMIA, LXIX, 2, 2024 (p. 37-47)
(RECOMMENDED CITATION)
DOI:10.24193/subbchem.2024.2.03

# DEVULCANIZED CRUMB RUBBER AS BITUMEN MODIFIER

**Gabriel VASILIEVICI[a,*], Andreea-Luiza MIRT[a], Simona GHIMIS[a], Emilian ZAHARIA[b], Mihaela BOMBOS[b], Dorin BOMBOS[b,c]**

**ABSTRACT.** The dispersion of crumb rubber in road bitumen is essential for enhancing the elasticity of asphalt coatings. However, elastomer cross-linking through vulcanization can reduce the colloidal stability of bitumen. This study aims to enhance compatibility by partially devulcanizing crumb rubber using a pulverulent catalyst, specifically phosphomolybdic acid, in a batch reactor at 270°C. The use of a molybdenum-based catalyst is preferred due to its effectiveness in catalyzing the devulcanization process. Additionally, further conditioning of the catalyst through grinding optimizes contact with crumb rubber, enhancing catalyst activity and improving overall compatibility with road bitumen.

***Keywords:*** *crumb rubber, desulfurization, molybdenum catalysts*

## INTRODUCTION

With the significant increase in the number of private vehicles, an estimated 17 million tons of waste tires are discarded worldwide each year, creating serious environmental problems due to difficulty in disassembly [1]. Generally, tires are made of rubber, carbon black, steel wire, sulfur compounds and synthetic fibers.

Technical experience has shown that rubber and fibers can improve the paving performance of asphalt mixtures in the road construction industry [2]. Traditional asphalt pavements struggle to achieve their planned service life

[a] *National Institute for Research Development for Chemistry and Petrochemistry-ICECHIM Bucharest, 202 Spl. Independenței, 060021, Bucharest, Romania*
[b] *ATICA Chemicals SRL, 202 Căzănești str., Râmnicu Vâlcea, 240414, Vâlcea, Romania*
[c] *Faculty of Petroleum Refining and Petrochemistry, Petroleum-Gas University, Bucharest Boulevard no. 39, Ploiesti, Prahova, RO 100680*
** Corresponding author: gvasilievici@icechim.ro*

under increased traffic volumes and high loads [3]. Therefore, there is an increasing trend to improve conventional asphalt to resist rutting, fatigue and other road deterioration. Modifying bitumen with crumb rubber (CR) is a concern for developed countries aiming to resolve the environmental problems associated with the improper disposal of used tires [4].

The process of modifying bitumen with CR was initially introduced in the 1960s. Since then, this technique has undergone substantial development and is now widely implemented across various regions. Several countries have even established their specifications for crumb rubber-modified bitumen (CRMB). It is widely accepted that CRMB has improved resistance to rutting and cracking compared to conventional bitumen [5].

One of the most widely used metals for devulcanization so far is ZnO, which has been extensively used in rubber vulcanization processes [6]. However, it is currently believed to be toxic in large quantities, especially to aquatic environments. Therefore, another metal that has taken its place is magnesium oxide, for which the exact mode of action and desulfurization are not yet fully understood [7]. In addition to these oxides, transition metal oxides such as $NiO_2$, $MoO_3$, $V_2O_5$, $TiO_2$, $WO_3$, $MnO_2$, $CeO_2$, and FeO have received significant attention [8-9]. Molybdenum-based catalysts are extensively studied due to their high activity involving multivalent metal transitions ($Mo^{5+}/Mo^{6+}$). However, these catalysts exhibit drawbacks like reduced activity with repeated use and loss of active components. Improvements in catalyst activity and stability are essential and can be achieved through modifications in loading mode, synthesis methods or incorporation of other elements [10].

The devulcanization process involves a series of steps, which can be outlined as follows: (i) shredding tires into small rubber particles; (ii) utilizing appropriate separators to remove fibers and steel; and (iii) further grinding the rubber to achieve a finer size, followed by mixing with various reclaiming agents [11-12]. The extensively researched devulcanization strategies encompass mechanical, chemical, physical, biological, microwave and ultrasonic processes [13-19].

The rubber can pass through industrial devulcanization either before its incorporation into asphalt mixtures (pre-devulcanized) or during the production of CRMB. The devulcanization and depolymerization of crumb rubber particles can occur within the binder at elevated temperatures and under high-shear mixing conditions [20]. The effectiveness of devulcanization and depolymerization tends to be greater when the binder is abundant in aromatic compounds [21].

Despite the advantages of CR bitumen modification, the process is still underutilized. There are studies that demonstrate the ecological sustainability of using CR in asphalt pavements, reducing the costs of managing end-of-life

tire waste and improving asphalt properties [22-24]. Unfortunately, in many countries, the adoption of CR modification was obstructed by the absence of standards and laws that support it.

This paper focuses on employing molybdenum-based catalysts for the devulcanization of CR, aiming to improve rubber compatibility with road bitumen. Molybdenum-based catalysts are chosen due to their unique properties, which contribute to their high catalytic activity. Additionally, these catalysts offer the potential to facilitate the desulfurization process of CR, enhancing its performance as a modifier for road bitumen. The study aims to explore the effectiveness of molybdenum-based catalysts in optimizing the properties of CR for use in asphalt applications, addressing key challenges related to rubber-bitumen compatibility.

## RESULTS AND DISCUSSION

The results of the thermogravimetric analysis of crumb rubber powder are shown in Table 1 and Figure 1. The mass losses in the first temperature range, starting from room temperature (R.T.) up to 125°C, are probably due to the presence of water in the rubber powder. Mass losses in the next range, up to 270°C, are the result of the evaporation of organic additives in the rubber such as mineral oils.

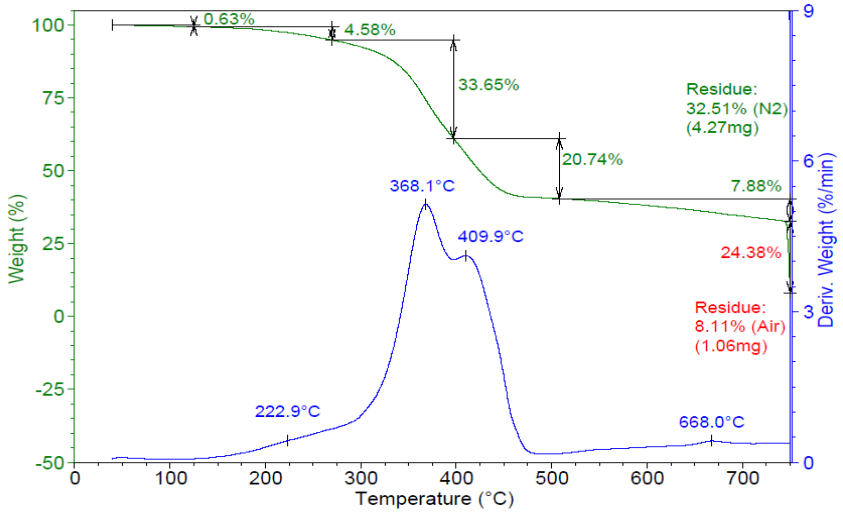


**Figure 1.** Thermogravimetric analysis (TGA) of crumb rubber powder

At temperatures above 270°C the pyrolysis reaction of the polyisoprene starts, which also occurs at higher temperatures (508°C). In the temperature range of 508 - 750°C thermal decomposition reactions of the carbonaceous materials from the previous steps as well as decomposition of inorganic rubber materials occur. The remaining residue represents 32.51% of the initial mass of the crumb rubber. The inert gas was changed to synthetic air at 750°C to highlight the type of residue left in the crucible. For 5 min at 750°C in the air (burning) the carbon black and other resulting carbonaceous materials were burned, leaving 8.11% residue. This ash consists of inorganic materials, probably silica which is used in the rubber industry together with carbon black for reinforcement.

**Table 1.** Results of thermogravimetric analysis of crumb rubber powder

| Domain, °C | Wt. loss, % | Tmax, °C |
|---|---|---|
| R.T. - 125°C | 0.63 | - |
| 125 - 270°C | 4.58 | 222.9 |
| 270 - 397°C | 33.65 | 368.1 |
| 397 - 508°C | 20.74 | 409.9 |
| 508 - 750°C | 7.88 | 668.0 |

The characteristics of the crumb rubber powder used in the experimental program are shown in Table 2.

**Table 2.** The characteristics of crumb rubber powder

| No. | Characteristics | Value |
|---|---|---|
| 1. | Particle sizes, mm | 1...2 |
| 2. | Density, kg/m$^3$ | 441 |
| 3. | Total sulfur content (Grote combustion method), % wt. | 2.34 |

A nanopowder of phosphomolybdic acid catalyst (sample code PMo) obtained by grinding in a planetary ball mill was used for the catalytic desulphurization of crumb rubber powder. Size distribution analysis of the catalyst dispersed in toluene was carried out using the Dynamic Light Scattering (DLS) method. An average particle size of 79.26 nm and a narrow nanoparticle size distribution were observed, as shown in Figure 2.

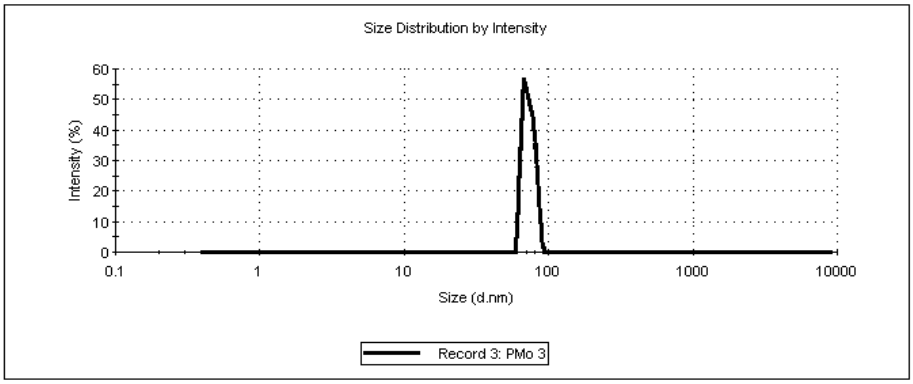


**Figure 2.** Particle size analysis (DLS) of ground PMo catalyst

Acid strength and distribution of acid sites on the PMo catalyst were characterized using diethylamine thermodesorption. The diethylamine thermodesorption curve, shown in Figure 3, provided insights into the acid strength profiles – weak, medium and strong centers. Table 3 presents the concentrations of acid sites with varying strengths and temperature ranges, as determined from the thermodesorption analysis of diethylamine.

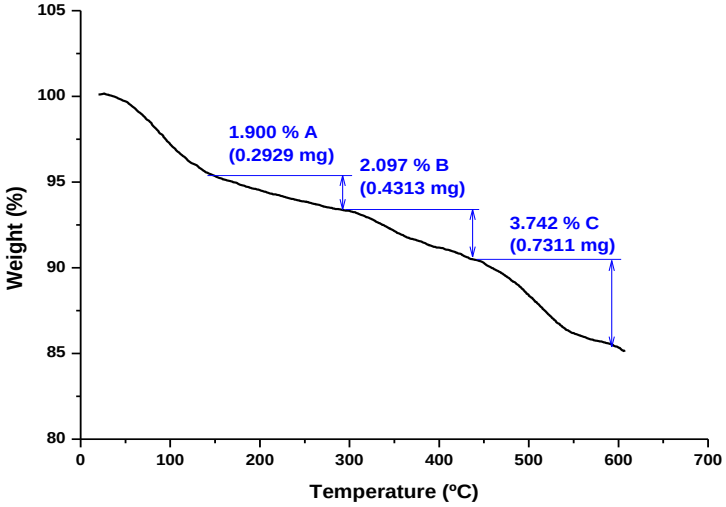


**Figure 3.** Thermodesorption curve for calculating the acid strength of PMo catalyst

**Table 3.** The proportion of acid centers of the PMo catalyst

| **Acid centers** | **Temperature range,** ºC | **Value,** mEq/ g analyzed sample |
|---|---|---|
| Weak | 160 – 300 | 0.2598 |
| Medium | 300 – 440 | 0.2867 |
| Strong | 440 - 580 | 0.5116 |

A high proportion of strong acid centers is observed (48.4%), with the proportion of weak and medium acid centers being smaller and approximately equal.

The temperature selected for desulfurization of the crumb rubber was 270ºC. From the thermogravimetric curve (Figure 1) it can be seen that at higher temperatures the pyrolysis of the elastomer starts, with a negative influence on the elastic characteristics of the bitumen modified with it.

The total sulfur content of crumb rubber after the catalytic desulfurization process in a batch system at 270ºC for 3 hours was 1.08% wt and the calculated conversion with equation (1) was higher with ground phosphomolybdenic acid 47.06 % compared with non-ground catalyst (Table 4).

**Table 4.** Performance of the catalytic desulfurization process of crumb rubber powder in batch system

| **Catalyst** | **Catalyst conc., % wt.** | **Time, h** | **Temperature, ºC** | **Conversion, %** |
|---|---|---|---|---|
| Phosphomolybdenic acid | 1.05 | 3 | 270 | 36.89 |
| Ground phospho-molybdenic acid | 1.05 | 3 | 270 | 47.06 |

The homogeneity of the CRMB was evaluated by determining the composition after short-term storage in a narrow tube, and by determining the asphaltene and elastomer content in the upper and lower zones of the tube. The values obtained are shown in Table 5.

**Table 5.** Asphaltene content of modified road bitumen sample

| **Sample** | **Asphaltene content, %** | |
|---|---|---|
| | **Upper zone** | **Lower zone** |
| Sample 1 | 19.35 | 19.47 |

The asphaltene content of road bitumen modified with devulcanized crumb rubber in the two areas of the bitumen sample is close, the observed differences being of the order of the error of the determination method.

## CONCLUSIONS

In conclusion, the desulfurization of crumb rubber was effectively facilitated by a nanostructured phosphomolybdenic acid catalyst. Thermogravimetric analysis of crumb rubber derived from used tires revealed its limited thermal stability above 280°C. Grinding the phosphomolybdenic acid produced a nanopowder with a narrow, monomodal particle size distribution, averaging 79.26 nm in diameter, and an acid strength exceeding 1 mEq/g. Using this catalyst, the desulfurization of crumb rubber dispersed in catalytic cracking oil at 270°C for 3 hours achieved a conversion rate of 47.06%. The resulting bitumen modified with devulcanized crumb rubber demonstrated high homogeneity, evidenced by consistent asphaltene content across different bitumen layers.

## EXPERIMENTAL SECTION

### *Materials*

Crumb rubber powder results from ground rubber from used tire waste, with a particle size in the range of 1-3 mm, a density of 441 kg/m$^3$, with a sulfur content of 2.34%, determined by the Grote combustion method. In the experimental program were used catalytic cracking oil and bitumen type D20/30 (Rompetrol), phosphomolybdic acid, diethylamine (Merck), Pluronic® P123 (Sigma-Aldrich), toluene, heptane (Chimopar S.A), hydrogen peroxide solution 3%, sodium carbonate (Chimreactiv SRL).

The main characteristics of the road bitumen and catalytic cracking oil used in the experimental program are shown in Tables 6 and 7.

**Table 6.** Specification of bitumen grade D20/30*

| No. | Specification | Unit | Value | Method |
|---|---|---|---|---|
| 1. | Penetration (25ºC), | 1/10 mm | 27 | SR EN 1426:2015 |
| 2. | Softening Point (Ring & Ball) | ºC | 59 | SR EN 1427:2015 |
| 3. | Ductility (25ºC) | cm | 110 | SR EN 13589:2015 |
| 4. | Fraass point | ºC | -12 | SR EN 12593:2015 |

*from the technical sheet of the product

**Table 7.** The characteristics of the catalytic cracking medium oil fraction*

| No. | Specification | Unit | Value |
|---|---|---|---|
| 1. | Appearance | - | viscous liquid, reddish brown |
| 2. | Relative density at 20°C | g/cm$^3$ | 0.882 |
| 3. | Boiling range | ºC | 400-450 |
| 4. | Flashpoint (closed cup) | ºC | 78 |
| 5. | Dynamic viscosity at 20°C | mPa·s | 40.8 |

***** from the technical sheet of the product

### *Characterization Methods*

Thermogravimetric analysis (TGA) of crumb rubber was performed with a Q5000IR (TA Instruments, USA), with the following parameters - 100 µL platinum crucible, 1-nitrogen purge gas (99.999%) with a flow rate of 50 mL/min, 2- synthetic air purge gas (99.999%) with a flow rate of 50 mL/min. Working method: 1) heating rate 10°C/min up to 750°C; 2) exchange gas 1 (nitrogen) with gas 2 (synthetic air); 3) isotherm for 5min.

Dynamic light scattering (DLS) was employed to analyze the particle size and particle size distribution of PMo using a NanoZS Zetasizer device from Malvern Instruments, UK. The sample was prepared by dispersing 0.005g ground phosphomolybdic acid in 25 mL of toluene

Acid strength and acid strength distribution of PMo was carried out by thermal desorption of diethylamine [25] using a DuPont Instruments apparatus. Before analysis, the test sample was placed in a vacuum oven at 120ºC for 12 hours to remove moisture.

### *Laboratory experiments*

#### *Preparation of phosphomolybdenic acid catalyst*

Phosphomolybdic acid was dry ground using a laboratory planetary mill in the presence of an anti-caking additive at 1% concentration (Pluronic-P123) for the preparation of the nanoparticle catalyst. A planetary ball mill (Fritsch Pulverisette 6) equipped with a 500 mL stainless steel bowl and 10 stainless steel balls (ϕ20 mm) was used for the laboratory experiments

***Catalytic devulcanization of crumb rubber powder***

The experiments were carried out in a 1L stainless steel autoclave Parr 4520 series, with thermostatic electric heating, at a temperature of 270ºC, with stirring at 160 rpm, in an inert gas atmosphere (nitrogen 5.0), and a crumb rubber/aromatic solvent mass ratio of 1/10 for 3 hours.

The conversion in the desulfurization process of crumb rubber with the phosphomolybdic acid was calculated by determining the total sulfur content by the Grote combustion method before and after experiments with equation (1):

$$Conversion, \% = \frac{TSCi - TSCf}{TSCi} \cdot 100 \quad (1)$$

*TSCi* = initial total sulfur content of the crumb rubber sample;

*TSCf* = final total sulfur content of the crumb rubber sample after the desulfurisation.

**The modification of road bitumen type D20/30** was done in a glass autoclave with a volume of 1 liter equipped with a thermostatic electric jacket and stirring. Working parameters were: temperature 160°C, stirrer speed 180 rpm, reaction time 5 hours, the concentration of the crumb rubber conditioned in aromatic oil 3%, and the mass ratio bitumen/ dispersion of 4/1.

**The stability of the modified bitumen** with devulcanized crumb rubber was assessed by determining its composition after short-term storage in a narrow tube for 24 hours. After preparation of the modified bitumen and cooling to 80ºC, it was placed in a cardboard tube, fixed in an upright position, and closed at the bottom. After storage for 24 hours in an oven at 80ºC, followed by cooling to room temperature, samples of modified bitumen (approx. 5 g) were taken from the area of the two ends of the tube to evaluate homogeneity. The homogeneity test of the modified bitumen was carried out by determining the asphaltene plus rubber content by the precipitation method in the presence of heptane. After adding about 5 g of modified bitumen to 50 ml of heptane and stirring, the mixture was left in the dark for 24 hours. The mixture was filtered and asphaltenes and non-dispersed rubber (insoluble in heptane) remained on the filter paper. The filter paper was brought to constant mass and weighed, thus calculating the asphaltene and polymer content of the modified bitumen sample analyzed.

## ACKNOWLEDGMENTS

This work was supported by a grant of the Ministry of Research, Innovation and Digitization, CCCDI - UEFISCDI, project number PN-III-P2-2.1-PTE-2021-0552, within PNCDI III.

## REFERENCES

1. A.M. Moasas; M. N. Amin; K. Khan; W. Ahmad; M. N. A. Al-Hashem; A. F. Deifalla; A. Ahmad; *Case Stud in Constr Mat,* **2022,** *17*, e01677.
2. J. Xu; M. Zheng; X. Ding; R. Qiao; W. Zhang; *Constr. and Build Mat.*, **2023,** *403,* e 133204.
3. Z. Qi-sen; C. Yu-liang; L. Xue-lian; *GeoHunan Intl. Conf*., **2009**.
4. M. Genever; K. O'Farrell; P.Randell; ***2017***, National market development strategy for used tyres 2017-2022, https://assets.sustainability.vic.gov.au/asset-download/Report-National-Market-Development-Strategy-Tyres-2018.pdf accessed nov. 2023.
5. D Lo Presti; *Constr. Build. Mater.***, 2013,** *49*, 863–881.
6. S. Mostoni; P. Milana; B. Di Credico; M. D'Arienzo; R. Scotti; *Catalysts,* **2019**, 9, 664.
7. A. A. da Silva; M. A. V. de Souza; A. M. F de Sousa; N. M. F. Carvalho; C. R. G. Furtado; *J. Appl. Polym. Sci.* **2024**, 141(7).
8. L. Chen; Z.P. Hu; J.T. Ren; Z. Wang; Z.Y. Yuan; *Microporous Mesoporous Mater.*, **2021**, 315.
9. L.-A. Mirt; D. Bombos; S. Ghimiș; M.M. Bombos; G. Vasilievici; *STUDIA UBB CHEMIA*, LXVIII, **2023,** 1, 225-238.
10. T. Yuming; L. Tenghui; Y. Guojia; W. Lui; T. La; Z. Zhiyong; R. Zhongqi; *Energy & Fuels*, **2019,** 33 (9), 8503-8510.
11. F.J.P. Navarro; F. Partal; C. Martinez-Boza; C. Valencia; C. Gallegos; *Chem. Eng. J.,* **2002**, *89*, 53–61.
12. B. Adhikari; D. De; S. Maiti; *Prog. Polym. Sci.*, **2000**, *2*, 909–948.
13. L. Asaro; M. Gratton; S. Seghar; N. A. Hocine; *Res. Cons. and Recycl.,* **2018,** *133,* 250-262.
14. I. Mangili; M. Lasagni; M. Anzano; E. Collina; V. Tatangelo; A. Franzetti; P. Caracino; A.I. Isayev; *Polym. Degrad. Stab.*, **2015**, *121*, 369–377.
15. B. Adhikari; D. De; S. Maiti; *Prog. Polym. Sci.*, **2000**, *2*, 909–948.
16. Mark; B. Erman; M. Roland; Recycling of Rubber, in *The Science and Technology of Rubber,* A.I. Isayev, Academic Press: Cambridge, MA, USA, **2013**; pp. 697–764.
17. Q. Lv; W. Huang; M. Zheng; Y. Hu; C. Yan; J. Wang; *Constr. and Build. Mat.,* **2022**, *348*,128716.
18. A. S. Mohamed; Z. Cao; X. Xu; F. Xiao; T. Abdel-Wahed; *J. Clean. Prod.,* **2022**, *373*, 133896.

19. I. Gawel; R. Stepkowski; F. Czechowski; *Ind. Eng. Chem. Res.,* **2006**, *4*, 3044–3049.
20. J.I. Gumede; B.G. Hlangothi, M. Briswell; C.D. Woolard; S.P. Hlangothi; *J. Clean. Prod.* **2022**, 362.
21. T.C. Billiter, J.S. Chun; R.R. Davison; C.J. Glover; J.A. Bullin; *Pet. Sci. Technol.,* **1997**, *15*, 445-469.
22. N. Herisanu; V. Bacria; *Appl. Mech. Mater,* **2013**, *430,* 257–261.
23. M. Liangş X. Xin; W. Fan; H. Luo; X. Wang; B. Xing; *Constr. Build. Mater.,* **2015**, *74*, 235–240.
24. D. Lo Presti; *Constr. Build. Mater.*, **2013**, *49,* 863–881.
25. D. Ion, M. Bombos, G. Vasilievici, A. Radu, P. Rosca, Rev.Chim. (Bucharest), **2019**, 70, 4266-4274.

STUDIA UBB CHEMIA, LXIX, 2, 2024 (p. 49-66)
(RECOMMENDED CITATION)
DOI:10.24193/subbchem.2024.2.04

# THE INHIBITORY PROPERTIES OF THE *FAGOPYRUM ESCULENTUM* GROATS BOILING EXTRACTS ON CORROSION OF THE MILD STEEL IN ACIDIC ENVIRONMENTS

**Pavel Anatolyevich NIKOLAYCHUK**[a,b,*]

**ABSTRACT.** The inhibitory ability of the boiling extracts from the groats of *Fagopyrum esculentum* on the corrosion of mild steel EN Fe37-3FN in 0.5 M hydrochloric acid and 0.5 M sulphuric acid media was investigated using gravimetric, electrochemical, and EIS methods. It was shown that the addition of 100 mg/l of the *Fagopyrum esculentum* groat extract reduces the corrosion rate by 50%, and that of of 1 g/l and more – by 75%. The adsorption of the extract components on a steel surface follows the Langmuir adsorption model, and the nature of adsorption is physical. The *Fagopyrum esculentum* groats extract shows itself as perspective and environmentally friendly substance for reducing the steel corrosion rate in acidic environments.

***Keywords:*** *Fagopyrum esculentum, common buckwheat, acid medium corrosion inhibition, gravimetric study, electrochemical study, Langmuir adsorption isotherm.*

## INTRODUCTION

The usage of industrial side products and wastes [1], expired drugs [2], food and biomass waste [3, 4] and compounds extracted from natural products [4] attract a growing interest of the corrosion engineers around the globe. By employing environmentally degradable natural compounds one could drastically reduce the costs and the ecological impact of both production of inhibitors, and their subsequent utilization. A plant's roots, leaves, aerial parts, fruits, and seeds are frequently used as the source of extracted compounds [4].

[a] *Kurganskij gosudarstvennyj universitet, Sovetskaya 63/4, 640020 Kurgan, Russian Federation*
[b] *Novosibirskij gosudarstvennyj universitet, Pirogova 2, 630090 Novosibirsk, Russian Federation*
** Corresponding author: pavel.nikolaychuk@kgsu.ru*

Common buckwheat (*Fagopyrum esculentum*) is a pceudocereal plant cultivated widely for its grain-like seeds, as a cover crop, as a green manure, as a plant for erosion control or as wildlife cover and feed [5]. The porridge made from the ground and roasted buckwheat groats is common for East Europe and Central Asia. During the cooking the groats are boiled in water, which is then usually discarded. However, the cotyledons of the buckwheat plant contain diverse phytochemicals, including rutin [6], tannins, catechin-7-O-glucoside, fagopyrins [7–10], salicylaldehyde and some other aromatic aldehydes [11, 12]. However, both aldehydes, flavonoids and phenols [13, 14] exhibit inhibitory properties on metal oxidation. Moreover, antioxidant activity of the compounds extracted from the buckwheat groats was already reported [15, 16], and there is a clear dependency between the antioxidant and inhibition properties of natural compounds [17]. Therefore, the compounds extracted into the boiling water from *Fagopyrum esculentum* groats during the cooking might be useful and environmentally friendly corrosion inhibitors.

Acidic environments are often employed for the study of the effectiveness of inhibitors, because acids give the most demonstrative results [14]. In addition, the study of the acidic corrosion of metals is important for oil and gas industry, the galvanic electroplating of metals, the development of the solutions for the metal pickling, and for the rust removal [14]. Usually both hydrochloric acid as the non-oxidising acid, and sulphuric acid as the oxidising acid are used for the acidic corrosion testing. Therefore, in the present study, the inhibitory properties of the boiling extracts of the *Fagopyrum esculentum* groats on the corrosion of mild steel EN Fe37-3FN in 0.5 M hydrochloric acid and 0.5 M sulphuric acid media are aimed to be investigated.

## RESULTS AND DISCUSSION

### *Gravimetric studies*

From the measured weight losses ($\Delta m = m_0 - m$, mg, where $m_0$ and m are the weights of the steel sample before and after immersion into corrosive medium, respectively), sample surfaces (S, $cm^2$), and immersion times (t, h) the average corrosion rates (ω, $mg/(cm^2 \cdot h)$) were estimated [14]:

$$\omega = \Delta m / (S \cdot t). \quad (1)$$

An inhibitory ability of the compound according to gravimetric measurements ($IE_{grav}$, %) was estimated from the ratio of the corrosion rates in the absence ($\omega_0$) and in the presence (ω) of the inhibitor [14]:

$$IE = (\omega_0 - \omega) / \omega_0 \cdot 100\%. \quad (2)$$

The dependence of the measured inhibition efficiencies at the different inhibitor concentrations ($c_{inh}$, g/l) is presented in Table 1. The results show that upon addition of the *Fagopyrum esculentum* groats extract the weight loss of the steel plates significantly reduces that confirms its inhibitory effect.

**Table 1.** The results of the gravimetric measurement of the corrosion rates

| **Medium** | **0.5 M HCl** | | **0.5 M $H_2SO_4$** | |
|---|---|---|---|---|
| **$c_{inh}$, g/l** | **ω, mg/(cm² · h)** | **$IE_{grav}$, %** | **ω, mg/(cm² · h)** | **$IE_{grav}$, %** |
| 0 | 0.89 ± 0.08 | – | 1.1 ± 0.1 | – |
| 0.1 | 0.42 ± 0.05 | 52.6 | 0.54 ± 0.05 | 51.2 |
| 0.3 | 0.26 ± 0.04 | 71.2 | 0.40 ± 0.05 | 63.8 |
| 1 | 0.17 ± 0.03 | 80.9 | 0.32 ± 0.04 | 71.0 |
| 3 | 0.14 ± 0.02 | 84.2 | 0.25 ± 0.04 | 77.2 |
| 10 | 0.12 ± 0.02 | 86.3 | 0.20 ± 0.03 | 81.4 |

### *Polarisation studies*

An open circuit potential ($E_{corr}$, mV) was recorded during 30 min. The results are presented in Figure 1.

As could be seen, the addition of the inhibitor shifts both the initial and the equilibrium values of the open circuit potentials of steel in acid in the more positive direction. This implies that the the *Fagopyrum esculentum* groats extract acts as the anodic type inhibitor, and primarily decreases the rate of the anodic dissolution of metal.

For the measurement of the linear polarisation resistance the polarisation curves were presented in the coordinates E(*i*), and the polarisation resistances ($R_p$, Ohm · cm²) were evaluated as the slopes of these curves using the least squares technique:

$$R_p = dE / di. \qquad (3)$$

The inhibitory ability of the compound according to the linear polarization resistance ($IE_{LPR}$) was estimated from the ratio of the polarisation resistances in the presence ($R_p$) and in the absence ($R_{p,0}$) of the inhibitor [14]:

$$IE_{LPR} = (R_p – R_{p,0}) / R_p \cdot 100\%. \qquad (4)$$

The results are presented in Figure 2 and in Table 2.

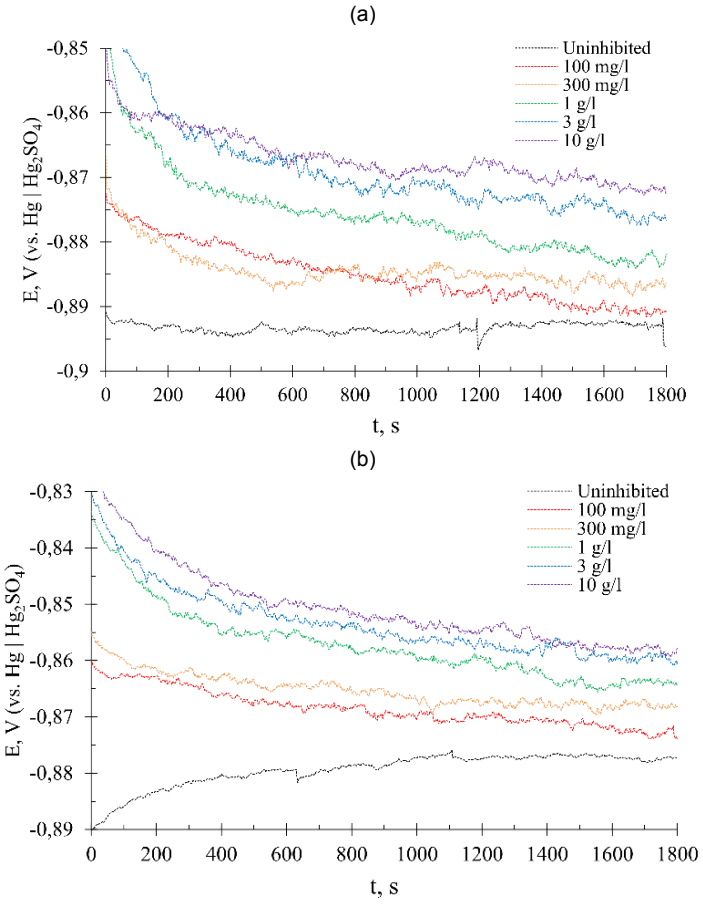


**Figure 1.** The open circuit potential of steel in (a) 0.5 M HCl, and (b) 0.5 M $H_2SO_4$ with the different additions of the *Fagopyrum esculentum* groats extract after 30 min of exposure.

**Table 2.** The measured polarisation resistance of the steel in the solutions of hydrochloric and sulphuric acids with the different additions of the inhibitor

| **Medium** | **0.5 M HCl** | | **0.5 M $H_2SO_4$** | |
|---|---|---|---|---|
| **$c_{inh}$, g/l** | **$R_p$, Ohm · cm²** | **$IE_{LPR}$, %** | **$R_p$, Ohm · cm²** | **$IE_{LPR}$, %** |
| 0 | 630 ± 10 | – | 410 ± 10 | – |
| 0.1 | 1420 ± 20 | 55.8 | 810 ± 10 | 49.5 |
| 0.3 | 2430 ± 40 | 74.1 | 1150 ± 20 | 64.2 |
| 1 | 3420 ± 50 | 81.6 | 1340 ± 20 | 69.4 |
| 3 | 4370 ± 70 | 85.6 | 1770 ± 30 | 76.7 |
| 10 | 5460 ± 90 | 88.5 | 2810 ± 50 | 85.3 |

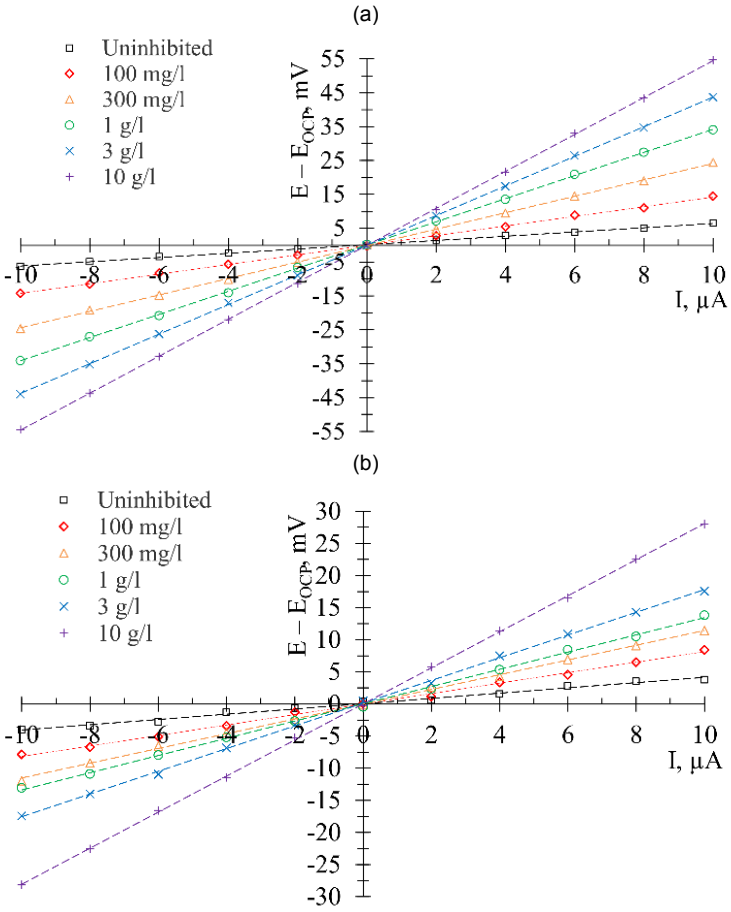


**Figure 2.** The linear polarisation resistance curves of steel in (a) 0.5 M HCl, and (b) 0.5 M $H_2SO_4$ with the different additions of the *Fagopyrum esculentum* groats extract

For the measurement of the Tafel slopes [18] and the corrosion current density the polarisation curves were presented in the coordinates $E$(lg $i$), and the Tafel slopes (b, mv/dec) and the corrosion current density ($i_{corr}$, A/cm$^2$) were evaluated from them [19]. Subsequently, the polarisation resistances ($R_p$, Ohm · cm$^2$) were estimated from the Tafel slopes and the corrosion current densities using the Stern – Geary equation [20, 21]:

$$R_p = b_a \cdot |b_c| / (ln\ 10 \cdot i_{corr} \cdot (b_a + |b_c|)), \quad (5)$$

where $b_a$ and $b_c$ are the slopes of the anodic and cathodic branches of the polarisation curve. The inhibitory ability of the compound according to the corrosion current densities ($IE_{CCD}$) was estimated from the ratio of the corrosion current densities in the absence ($i_0$) and in the presence ($i$) of the inhibitor [14]:

$$IE_{CCD} = (i_0 - i) / i_0 \cdot 100\%, \quad (6)$$

and also from the ratio of the polarisation resistances in the presence (R) and in the absence ($R_0$) of the inhibitor using equation (4). The results are presented in Figure 3 and in Table 3.

**Table 3.** The results of the electrochemical measurement of the corrosion rates

| $c_{inh}$, g/l | $E_{corr}$, mV | $b_a$, mV/dec | $b_c$, mV/dec | $i_{corr}$, μA/cm$^2$ | $IE_{CCD}$, % | $R_p$, Ohm·cm$^2$ | $IE_{LPR}$, % |
|---|---|---|---|---|---|---|---|
| 0.5 M HCl with additions of *Fagopyrum esculentum* groats extract | | | | | | | |
| 0 | –896 | 98.9 | –118.8 | 38.4 | – | 611 | – |
| 0.1 | –891 | 75.6 | –127.1 | 17.4 | 54.7 | 1185 | 48.4 |
| 0.3 | –886 | 72.6 | –130.0 | 9.9 | 74.0 | 2037 | 70.1 |
| 1 | –882 | 70.5 | –134.4 | 7.0 | 81.6 | 2852 | 78.5 |
| 3 | –877 | 75.5 | –130.1 | 4.9 | 87.1 | 4183 | 85.4 |
| 10 | –873 | 64.3 | –146.5 | 3.9 | 89.7 | 4895 | 87.5 |
| 0.5 M $H_2SO_4$ with additions of *Fagopyrum esculentum* groats extract | | | | | | | |
| 0 | –877 | 55.1 | –117.3 | 38.8 | – | 319 | – |
| 0.1 | –874 | 37.6 | –115.8 | 21,3 | 45.2 | 579 | 44.8 |
| 0.3 | –868 | 31.9 | –121.4 | 15.0 | 61.3 | 730 | 56.2 |
| 1 | –864 | 30.9 | –126.2 | 11.9 | 69.4 | 903 | 64.5 |
| 3 | –860 | 32.1 | –128.6 | 10.2 | 73.8 | 1281 | 75.0 |
| 10 | –857 | 33.1 | –128.9 | 7.8 | 79.9 | 1511 | 78.8 |

As could be seen from the results, the Tafel slopes of the anodic branches of polarisation curves significantly decrease upon addition of the buckwheat groats extract, whereas the slopes of the cathodic branches of polarisation curves slightly increase. This confirms that the extract acts as the anodic type inhibitor, and decreases the rate of metal anodic dissolution, whereas the rate of the hydrogen production at the cathode remains practically the same. The values of the linear polarisation resistances obtained experimentally and estimated by the Stern–Geary equation coincide well, which confirms the integrity of the experimental data.

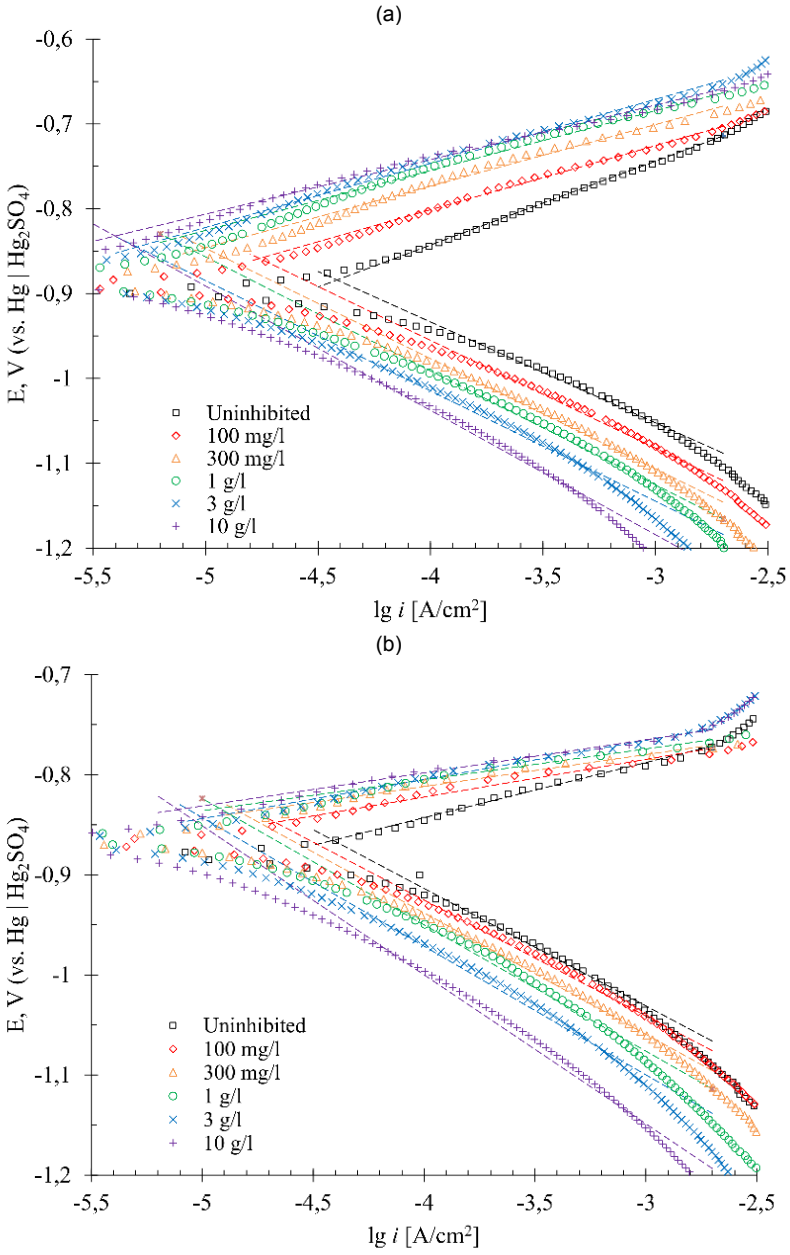


**Figure 3.** The polarisation curves of steel in (a) 0.5 M HCl, and (b) 0.5 M $H_2SO_4$ with the different additions of the *Fagopyrum esculentum* groats extract after 30 min of exposure.

### *EIS studies*

For EIS tests, the obtained results were presented in the form of Bode and Nyquist plots [22]. For the estimation of the impedance parameters, a simplified Randles equivalent electrical circuit [23], containing the solution resistance $R_s$, the consecutive charge transfer resistance $R_{ct}$ of the passivation layer, and the parallel constant-phase element representing the double electric layer, was employed. The impedance ($Z$, Ohm) of the Randles equivalent circuit is expressed by the equation [22]:

$$Z = R_s + 1 / ((1 / R_{ct}) + P \cdot (i \cdot \omega)^n), \quad (7)$$

where ω, Hz is the frequency of the alternate current, i is an imaginary unit, and P and n are the parameters of the constant phase element.

The fitting of the equivalent circuit parameters to the experimental impedance values was performed using the free software EIS Spectrum Analyser [24]. In addition, the capacitance ($C_{dl}$, F) and the thickness (d, m) of the double electric layer were estimated [25]:

$$C_{dl} = P^{1/n} \cdot (R_s \cdot R_{ct} / (R_s + R_{ct}))^{(1-n)/n}, \quad (8)$$

$$d = (S \cdot \varepsilon_0 \cdot \varepsilon) / C_{dl}, \quad (9)$$

where $S$, $m^2$ is the electrode surface, ε is the dielectric constant of water, and $\varepsilon_0 = 8.85 \cdot 10^{-12}$ F/m is the dielectric constant of vacuum.

The inhibitory ability of the compound according to the electrochemical impedance spectroscopy ($IE_{EIS}$) was estimated from the ratio of the charge transfer resistances in the presence ($R_{ct}$) and in the absence ($R_{ct,0}$) of the inhibitor [14]:

$$IE_{EIS} = (R_{ct} - R_{ct,0}) / R_{ct} \cdot 100\%. \quad (10)$$

The results are presented in Figure 4 and in Table 4.

The Nyquist plots demonstrate a semicircle behaviour typical for the Rangles equivalent circuit. With addition of the inhibitor the semicircle diameter increases, but the form of the plot does not change, which implies that the inhibitor does not alter the corrosion mechanism (which is also confirmed by the almost constant value of the constant phase element parameter n) but increases the resistance of the charge transfer through the metal surface. The constant phase element parameter P decreases upon addition of the buckwheat groats extract, which means the decrease of the double layer capacitance, and the increase of the double layer thickness.

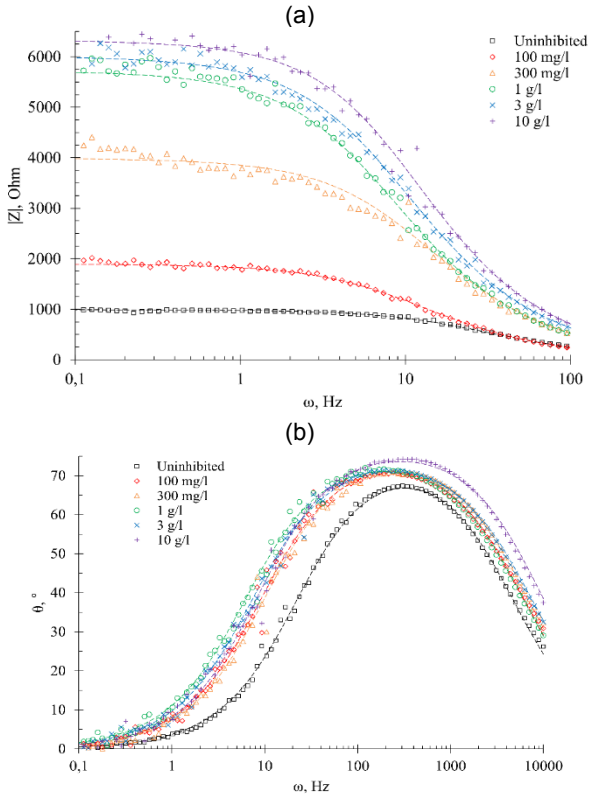


**Figure 4ab.** The Bode plots of steel in (a), (b) 0.5 M HCl with the different additions of the *Fagopyrum esculentum* groats extract after 30 min of exposure.

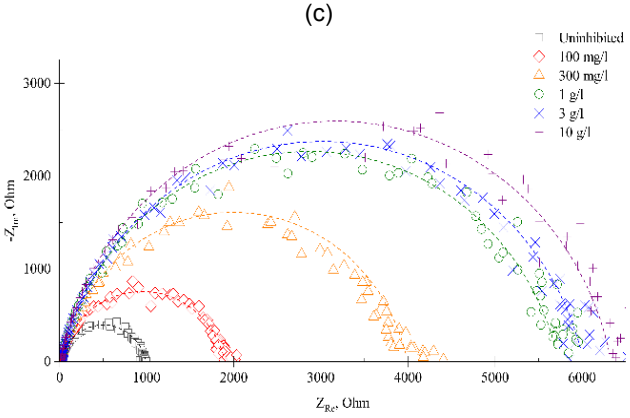


**Figure 4c. T**he Nyquist plots of steel in 0.5 M HCl with the different additions of the *Fagopyrum esculentum* groats extract after 30 min of exposure.

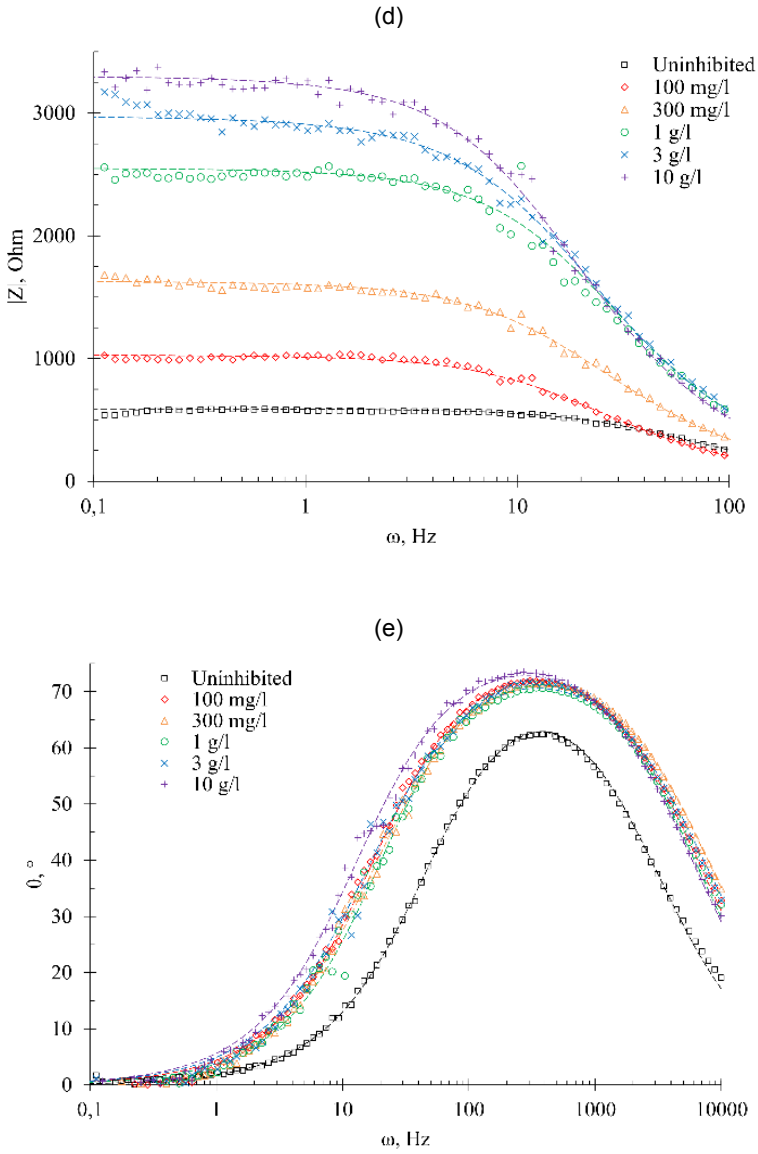


**Figure 4de.** The Bode plots of steel in (d), (e) 0.5 M $H_2SO_4$ with the different additions of the *Fagopyrum esculentum* groats extract after 30 min of exposure.

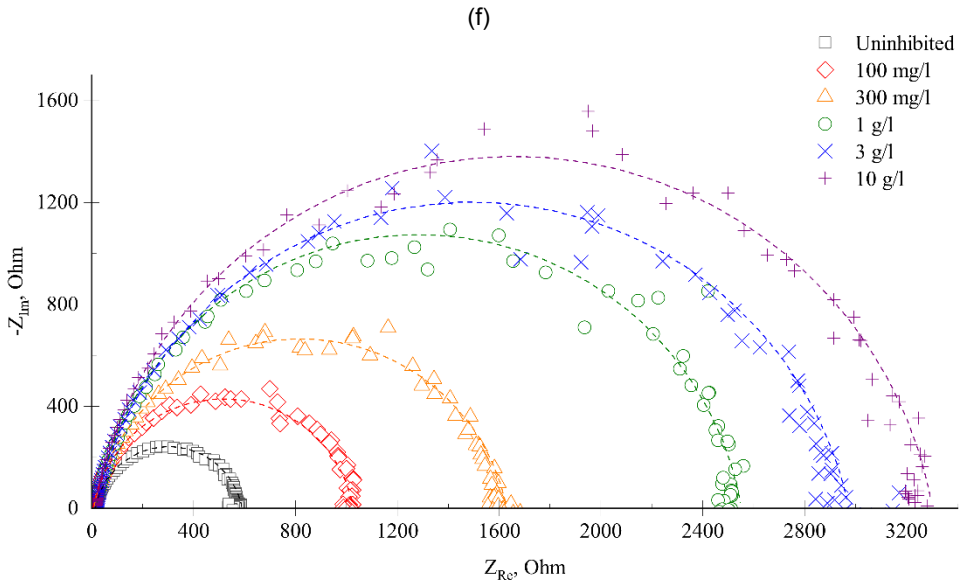


**Figure 4f.** the Nyquist plots of steel in 0.5 M $H_2SO_4$ with the different additions of the *Fagopyrum esculentum* groats extract after 30 min of exposure.

**Table 4.** The results of the EIS measurement of the corrosion rates

| $c_{inh}$, g/l | $R_s$, Ohm | P, $\mu Ohm^{-1} \cdot s^n$ | n | $C_{dl}$, μF | d, nm | $R_{ct}$, Ohm | $IE_{EIS}$, % |
|---|---|---|---|---|---|---|---|
| 0.5 M HCl with additions of *Fagopyrum esculentum* groats extract | | | | | | | |
| 0 | 9.8 | 142.6 | 0.86 | 710 | 3.91 | 983.3 | – |
| 0.1 | 7.1 | 162.6 | 0.85 | 739 | 3.75 | 1891.3 | 48.0 |
| 0.3 | 14.4 | 69.2 | 0.87 | 347 | 7.99 | 3979.4 | 75.3 |
| 1 | 15.9 | 77.1 | 0.85 | 354 | 7.83 | 5717.9 | 82.8 |
| 3 | 16.3 | 63.8 | 0.85 | 285 | 9.74 | 6002.9 | 83.6 |
| 10 | 13.4 | 48.8 | 0.88 | 246 | 11.30 | 6319.5 | 84.4 |
| 0.5 M $H_2SO_4$ with additions of *Fagopyrum esculentum* groats extract | | | | | | | |
| 0 | 14.8 | 110.6 | 0.89 | 663 | 4.17 | 575.8 | – |
| 0.1 | 5.2 | 150.8 | 0.89 | 828 | 3.34 | 1022.8 | 43.7 |
| 0.3 | 7.8 | 97.9 | 0.87 | 472 | 5.86 | 1622.4 | 64.5 |
| 1 | 15.2 | 51.6 | 0.89 | 283 | 9.77 | 2535.8 | 77.3 |
| 3 | 13.9 | 61.6 | 0.87 | 302 | 9.16 | 2959.6 | 80.5 |
| 10 | 14.1 | 60.4 | 0.89 | 335 | 8.26 | 3287.3 | 82.4 |

### *Langmuir adsorption model*

The description of the adsorption of the groats extract components on the steel surface was performed in terms of the Langmuir adsorption model [26]. The Langmuir adsorption isotherm equation was linearised in the form:

$$c_{inh} / \theta = 1 / K_{ads} + c_{inh}, \quad (11)$$

where $c_{inh}$, g/l is the concentration of the *Fagopyrum esculentum* groats extract solution, $K_{ads}$, l/g is the adsorption-desorption equilibrium constant, and θ is the percentage of the surface covered by the inhibitor, which assumed to be equal to the inhibition efficiency. The dependencies of $c_{inh}/\theta$ on $c_{inh}$ are presented in Figure 5 and in Table 5.

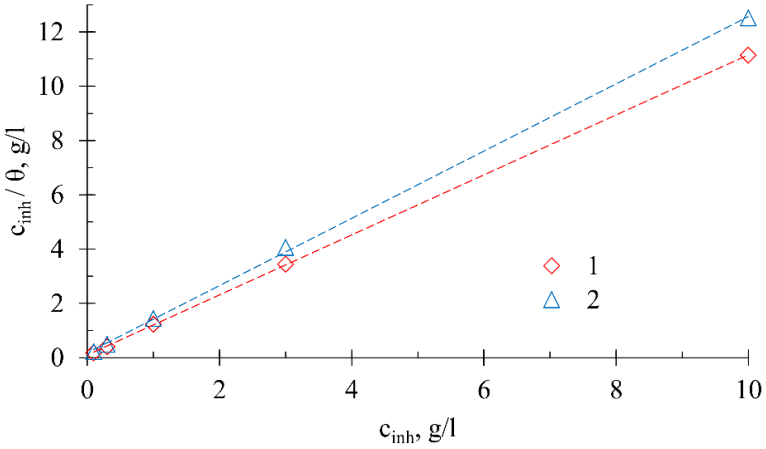


**Figure 5.** The plots of $c_{inh}$ / θ vs. $c_{inh}$ for the adsorption of the *Fagopyrum esculentum* groats extract on the steel surface from the solution of (1) 0.5 M HCl, (2) 0.5 M $H_2SO_4$.

The data were processed using the least squares technique [27], and the equilibrium constants $K_{ads}$ were estimated as the intercepts of the regression equations. The Gibbs energy changes of the sorption ($\Delta_{ads}G$, J/mol) were estimated from the equation:

$$\Delta_{ads}G = -RT \ln (K_{ads} \cdot c_{water}), \quad (12)$$

where $c_{water} = 10^3$ g/l is the water concentration in the extracts. The results are presented in Table 5. The results show that the Langmuir adsorption model describes the inhibitor sorption on the metal surface quite well. The

calculated Gibbs energies of sorption do not exceed –20 kJ/mol for both hydrochloric and sulphuric acids, which means the physical nature of the sorption.

**Table 5.** The parameters of the Langmuir adsorption model

| $C_{inh}$, g/l | θ | $C_{inh}$ / θ, g/l | Regression equation | $K_{ads}$, l/g | $\Delta_{ads}G$, kJ/mol |
|---|---|---|---|---|---|
| 0.5 M HCl with additions of *Fagopyrum esculentum* groats extract | | | | | |
| 0.1 | 0.547 | 0.183 | $c_{inh}$ / θ = (1.106 ± 0.003) · $c_{inh}$ + (0.09 ± 0.02); $R^2$ = 0.999 | 11 ± 2 | –23 ± 1 |
| 0.3 | 0.740 | 0.405 | | | |
| 1 | 0.816 | 1.225 | | | |
| 3 | 0.871 | 3.444 | | | |
| 10 | 0.897 | 11.148 | | | |
| 0.5 M $H_2SO_4$ with additions of *Fagopyrum esculentum* groats extract | | | | | |
| 0.1 | 0.452 | 0.221 | $c_{inh}$ / θ = (1.24 ± 0.01) · $c_{inh}$ + (0.18 ± 0.07); $R^2$ = 0.998 | 7 ± 3 | –21 ± 2 |
| 0.3 | 0.613 | 0.489 | | | |
| 1 | 0.694 | 1.441 | | | |
| 3 | 0.738 | 4.065 | | | |
| 10 | 0.799 | 12.516 | | | |

The results of the open circuit potential measurements show that with the addition of a *Fagopyrum esculentum* groats extract the potential of the mild steel both in the solution of 0.5 M HCl and 0.5 M $H_2SO_4$ shifts to the more positive values. In addition, the Tafel slopes of the anodic branches of the polarisation curves decrease with alteration of the extract concentration, whereas the slopes of the cathodic branches only slightly increase. This implies that in the solutions of both acids the buckwheat groats extract acts as the anodic-type inhibitor [28, 29].

The values of the inhibition efficiencies estimated from the data of gravimetric ($IE_{grav}$), electrochemical ($IE_{LPR}$ and $IE_{CCD}$) and EIS experiments ($IE_{EIS}$) coincide well and show the similar trend. The values of the polarisation resistance of the absorbed inhibitor estimated from the data of linear polarisation and from the Tafel slopes also coincide well, which confirms the integrity of the data.

With the increase of the extract concentration from 0.1 to 1 g/l its inhibition efficiency on the corrosion of mild steel EN Fe37-3FN in a 0.5 M hydrochloric acid medium rises from ~50% to ~80%, but the further concentration increase gives no significant improvement of the inhibition efficiency. In contrast, the inhibition efficiency of the extract on the corrosion of the same steel in a 0.5 M sulphuric aicd medium continues to increase with the rise of extract concentration, and approaches ~80% when the concentration of 10 g/l is achieved.

The adsorption of the extracted components on the steel surface fairly obeys the Langmuir adsorption model. The calculated Gibbs energies of sorption are in the range ~ –20 kJ/mol for both hydrochloric and sulphuric acids, which means that the nature of the adsorption is physical due to the electrostatic interactions [30].

Despite the experimental values of the inhibition efficiencies may vary significantly with alteration of both the solution composition and temperature [31], the groats extracts of *Fagopyrum esculentum* showed itself as a perspective natural corrosion inhibitor for steels in acidic environments. The addition of buckwheat groats extracts to a corrosive environment can be used to protect equipment from corrosion in pickling areas of metal processing industries, and in electroplating baths, and also be part of products for removing corrosion products from steel surfaces [32, 33].

## CONCLUSIONS

The inhibitory ability of the *Fagopyrum esculentum* groats boiling extracts on the corrosion of mild steel EN Fe37-3FN in 0.5 M hydrochloric acid and 0.5 M sulphuric acid media was investigated using gravimetric, electrochemical, and EIS methods. It was shown that the addition of 100 mg/l of the extract reduces the corrosion rate in HCl by 50% and in $H_2SO_4$ by 50%, whereas the addition of 10 g/l of the extract further reduces the corrosion rate by 80%. The adsorption of the extract components on a steel surface follows the Langmuir adsorption model, and the nature of adsorption is physical. The *Fagopyrum esculentum* groats extract shows itself as perspective and environmentally friendly substance for reducing the steel corrosion rate in acidic environments.

## EXPERIMENTAL SECTION

### *Reagents and Equipment*

Ethanol (analytical grade) and hydrochloric and sulphuric acids (pure grade) were purchased from LLC “Sigma Tek” (Khimki, Russia). Steel electrodes were manufactured from cylindrical ingots made of mild steel EN Fe37-3FN (containing no more than 0.14% C, 0.3% Ni, Cu, and Cr, 0.05% Si, 0.4% Mn, 0.05% P and 0.04% S). The unused flat end surface of the ingots was sealed by the epoxy resin, and the cylindrical working surface immersed in the solution was equal to 0.04 $cm^2$.

Weighting of the samples was performed using the analytical balance EX224/AD (Ohaus Corp., Parsippany, USA). Electrochemical and EIS measurements were conducted using the potentiostat-galvanostat PS-50 (LLC "SmartStat", Chernogolovka, Russia). The mercury-mercurous sulphate reference electrode by Schott Instruments GmbH (Meinz, Germany) was used. A water for solution preparation was first distilled using the aquadistiller AE-15 (LLC "Livam", Belgorod, Russia) and then deionized using the water purification system AkvaLab S18 (LLC "Akvalab", Moscow, Russia). The magnetic stirrer MS-200 LT (LLC "Labtex", Moscow, Russia) was used for stirring and heating the solutions. The single-channel laboratory pipettes manufactured by Thermo Fisher Scientific (Waltham, USA) were used for pipetting the solutions. A laboratory glassware of 2nd grade was used.

***Preparation of the extracts***

The buckwheat grain is collected usually after 90–110 days after seeding, separated from grain shells, processed by steam under the temperature of 120 $^{o}$C and pressure of 0.6 MPa during 10 minutes, then air-dried and ground.

The dried and ground groats of the common buckwheat are produced in Russia at the industrial scale, and are commercially available. They were purchased from LLC "Kamelot-A" (Tomsk, Russia).

A total of 100 g of dried and ground *Fagopyrum esculentum* groats were weighted, immersed into a litre of the deionised water, heated and boiled under the reflux condenser during 3 h. The boiling extracts were cooled, the groat material was removed, and the solid residues were filtered off through the filter paper with the pore diameter of 12 μm.

A total of 10 ml of each extract were taken, placed in a beaker and heated to dryness in order to determine the masses of the dissolved substances and the initial concentrations of the extract solutions. Then the working solutions of the *Fagopyrum esculentum* groats extract with the concentrations ranging from 0.2 to 20 g/l were prepared by the appropriate dilutions. The solutions were then equally diluted by 1 M hydrochloric acid or by 1 M sulphuric acid to finally produce a series of acidic solutions of *Fagopyrum esculentum* groats extract in 0.5 M HCl or 0.5 M $H_2SO_4$ with concentrations ranging from 0.1 to 10 g/l.

***Gravimetric studies***

For gravimetric tests, rectangular flat plates made of EN Fe37-3FN mild steel with thickness 3 mm, width 20 ± 2 mm, and height 30 ± 2 mm (the plate surface is 15 cm$^2$) were polished using the P2500 emery paper and degreased by ethanol. The weighted plates were immersed into corrosive media for 2 h, then washed with distilled water, dried, and reweighted. Each experiment was performed in triplicate.

### *Electrochemical and EIS studies*

For electrochemical and EIS tests, electrodes made of EN Fe37-3FN mild steel and sealed with the epoxy resin with the working surface of 0.04 $cm^2$ were polished using the P2500 emery paper and degreased by ethanol. The measurements were conducted in a standard three-electrode electrochemical cell, consisting of the working electrode (steel sample), auxiliary electrode from the porous graphite, and the mercury-mercurous sulphate reference electrode. An open circuit potential was recorded during 30 min. For the measurement of the linear polarization resistance the polarization curves were recorded in galvanodynamic mode in the current ranges from –10 μA and to +10 μA with the current sweep rate of 2 μA/s. For the measurement of the Tafel slopes [18] and the corrosion current density the polarisation curves were recorded in both directions in the potential ranges from the measured open circuit potential to –500 mV and to +500 mV relatively to it with the potential sweep rate of 10 mV/s. An impedance values were recorded at the open circuit potential value in the alternate current frequency interval from 100 mHz to 10 kHz with the potential amplitude of 10 mV. Each experiment was performed in triplicate.

## ACKNOWLEDGMENTS

This work was supported by the state assignments of the Ministry of Science and Higher Education of the Russian Federation (Project Reg. No. 1023041400091-5-3.2.10;2.4.2 and FSUS-2022-0022) and the strategic academic leadership program “Prioritet 2030”.

## REFERENCES

1. R. Haldhar; S. C. Kim; E. Berdimurodov; D. K. Verma; C. M. Hussain; Corrosion inhibitors: industrial applications and commercialization. In *Sustainable corrosion inhibitors II: Synthesis, design, and practical applications*, ACS Symposium Series, American Chemical Society, USA **2021**, Volume 1404, pp. 219-235. doi: 10.1021/bk-2021-1404.ch010.
2. N. Vaszilcsin; A. Kellenberger; M. L. Dan; D. A. Duca; V. L. Ordodi; *Materials*, **2023**, *16(16)*, 5555. doi: 10.3390/ma16165555.
3. A. Thakur; S. Sharma; R. Ganjoo; H. Assad; A. Kumar; *J. Phys. Conf. Ser.*, **2022**, *2267(1)*, 012079. doi: 10.1088/1742-6596/2267/1/012079.
4. S. Marzorati; L. Verotta; S. P. Trasatti; *Molecules*, **2018**, *24(1)*, 48. doi: 10.3390/molecules24010048.

5. T. Björkman; R. R. Bellinder; R. R. Hahn; J. Shail; *Buckwheat Cover Crop Handbook*, Cornell University, Ithaca, New York, USA **2008**.
6. S. Kreft; M. Knapp; I. Kreft; *J. Agric. Food Chem.*, **1999**, *47(11)*, 4649–4652. doi:10.1021/jf990186p.
7. K. Eguchi; T. Anase; H. Osuga; *Plant Prod. Sci.*, **2009**, *12(4)*, 475–480. doi:10.1626/pps.12.475.
8. L. Ožbolt; S. Kreft; I. Kreft; M. Germ; V. Stibilj; *Food Chem.*, **2008**, *110(3)*, 691–696. doi: 10.1016/j.foodchem.2008.02.073.
9. E. Tavčar Benković; D. Žigon; M. Friedrich; J. Plavec; S. Kreft; *Food Chem.*, **2014**, *143*, 432–439. doi: 10.1016/j.foodchem.2013.07.118.
10. S. Kreft; D. Janeš; I. Kreft; *Acta Pharm.*, **2013**, *63(4)*, 553–560. doi:10.2478/acph-2013-0031.
11. D. Janes; S. Kreft; *Food Chem.*, **2008**, *109(2)*, 293–298. doi: 10.1016/j.foodchem.2007.12.032.
12. D. Janes; D. Kantar; S. Kreft; H. Prosen; *Food Chem.*, **2009**, *112(1)*, 120–124. doi: 10.1016/j.foodchem.2008.05.048.
13. N. Bhardwaj; P. Sharma; V. Kumar; *Cor. Rev.*, **2021**, *39(1)*, 27-41. doi: 10.1515/corrrev-2020-0046.
14. A. Kadhim; A. A. Al-Amiery; R. Alazawi; M. K. S. Al-Ghezi; R. H. Abass; *Int. J. Cor. Scale Inh.*, **2021**, *10(1)*, 54-67. doi: 10.17675/2305-6894-2021-10-1-3.
15. M. Watanabe; *J. Agric. Food Chem.*, **1998**, *46(3)*, 839-845.
16. I. Sedej; M. Sakač; A. Mandić; A. Mišan; V. Tumbas; J. Čanadanović-Brunet; *J. Food Sci.*, **2012**, *77(9)*, C954-C959. doi: 10.1111/j.1750-3841.2012.02867.x.
17. V. I. Vorobyova; M. I. Skiba; A. S. Shakun; S. V. Nahirniak; *Int. J. Cor. Scale Inh.*, **2019**, *8(2)*, 150-178. doi: 10.17675/2305-6894-2019-8-2-1.
18. J. Tafel; *Z. Phys. Chem.*, **1905**, *50(1)*, 641-712. doi: 10.1515/zpch-1905-5043.
19. F. Mansfeld; *Corrosion*, **1973**, *29(10)*, 397-402. doi: 10.5006/0010-9312-29.10.397.
20. M. Stern; *Corrosion*, **1958**, *14(9)*, 60-64. doi: 10.5006/0010-9312-14.9.60.
21. M. Stern; A. L. Geary; *J. Electr. Soc.*, **1957**, *104(1)*, 56-63. doi: 10.1149/1.2428496.
22. X. Z. Yuan; C. Song; H. Wang; J. Zhang; EIS equivalent circuits. In *Electrochemical Impedance Spectroscopy in PEM Fuel Cells: Fundamentals and Applications*, X. Z. Yuan et al. Eds.; Springer, Berlin, Germany, **2010**, pp. 139-192. doi: 10.1007/978-1-84882-846-9_4.
23. J. E. B. Randles; *Disc. Faraday Soc.*, **1947**, *1*, 11-19. doi: 10.1039/DF9470100011.
24. A. S. Bondarenko; G. A. Ragoisha; Inverse problem in potentiodynamic electrochemical impedance spectroscopy. In *Progress in Chemometrics Research*, A. L. Pomerantsev Ed.; Nova Science Publishers, New York, USA, **2005**, pp. 89–102, http://www.abc.chemistry.bsu.by/vi/analyser.
25. A. Lasia; *Electrochemical Impedance Spectroscopy and its Applications*, Springer, New York, USA, **2014**. doi: 10.1007/978-1-4614-8933-7.
26. I. Langmuir; *J. Am. Chem. Soc.*, **1918**, *40(9)*, 1361-1403. doi: 10.1021/ja02242a004.

27. R. Adrain; *The Analyst; Or Mathematical Museum*, **1808**, *1(4)*, 93-109.
28. S.-I. Pyun; *ChemTexts*, **2021**, *7(1)*, 2. doi: 10.1007/s40828-020-00121-y.
29. X. Xie; R. Holze; *ChemTexts*, **2018**, *4(1)*, 5. doi: 10.1007/s40828-018-0057-0.
30. A. Kokalj; *Cor. Sci.*, **2022**, *196*, 109939. doi: 10.1016/j.corsci.2021.109939.
31. A. B. Kičenko; V. M. Kušnarenko; *Praktika protivokorrozionnoj zaŝity*, **2005**, *4(38)*, 17-22.
32. T. J. Harvey, F. C. Walsh; A. H. Nahlé; *J. Mol. Liq.*, **2018**, *266*, 160-175. doi: 10.1016/j.molliq.2018.06.014.
33. M. Goyal; et al. *J. Mol. Liq.*, **2018**, 256, 565-573, doi: 10.1016/j.molliq.2018.02.045.

STUDIA UBB CHEMIA, LXIX, 2, 2024 (p. 67-80)
(RECOMMENDED CITATION)
DOI:10.24193/subbchem.2024.2.05

# CHARACTERIZATION OF SOME PLANT EXTRACTS BY ULTRASOUND-ASSISTED EXTRACTION IN SUNFLOWER OIL USING THIN LAYER CHROMATOGRAPHY AND SPECTROPHOTOMETRY UV-VIS

**Mălina FIASTRU-IRIMESCU[a,b*], Diana ENE[a], Denisa MARGINĂ[b]**

**ABSTRACT**. The purpose of this work was to prove the enrichment of sunflower oil with active principles (polyphenolic acids, flavones, flavonoids) from plants, using the ultrasounds-assisted extraction (UAE) process. The analytical technique used for qualitative characterization of the UAE samples is thin layer chromatography (TLC), a relatively simple technique, which under certain separation and detection conditions highlights the bioactive components of the plants studied in our study. UV-VIS spectrophotometry was used to evaluate the level of flavonoids. The UAE samples in sunflower oil were also characterized by determining the alpha-tocopherol content through a gas-cromatographic method (GC-MS), and by evaluating the antioxidant activity through an indirect DPPH spectrophotometric method. The oily plants extracts were obtained to be used as raw material in the formulation of a dermato-cosmetic product, and thus the characterisation performed herein is very useful in supporting the effects of the above-mentioned products.

***Keywords****: sunflower oil, ultrasound-assisted extraction, TLC, UV-VIS, GC-MS*

## INTRODUCTION

In recent years, people have begun to appreciate the gifts of nature again, taking advantage of the beneficial content of plants: flavones and their glycosides, polyphenolic compounds, carotenoids, triterpenes, chlorophylls, essential oils.

[a] *Biotehnos SA, 3-5 Gorunului,Otopeni, Iflov, Romania*
[b] *"Carol Davila" University of Medicine and Pharmacy, Faculty of Pharmacy, Biochemistry Department, 6 Traian Vuia, Bucharest, Romania*
** Corresponding author: malina.fiastru@gmail.com*

All these compounds can be extracted by maceration in solvents (ethanol) or edible oils (sunflower oil, olive oil) [1]. Over time, studies have been carried out on the effectiveness of sunflower oil on the skin. It was chosen for its emollient action and to restore the stratum corneum, creating a protective barrier and maintaining hydration of the epidermis. In its composition, sunflower oil has an important amount of alpha-tocopherol, a fat-soluble antioxidant, responsible for reducing the oil autooxidation and for protecting the cell membranes against peroxidation [2].

Most of the studies were carried out in disadvantaged areas, on newborns and on children suffering from severe acute malnutrition, demonstrating the fact that, although it is a cheap product, topical therapy with sunflower oil was beneficial as an adjuvant therapy, improving the skin's barrier function, reducing the risk of skin infections [3-5].

Over time, numerous products based on sunflower oil have been reported: emulsions, soap, creams [6, 7]. It has been proven that these products have an anti-inflammatory, anti-acne, moisturizing and protective effect.

Several procedures are known for extracting active principles from plants: maceration (hot maceration, cold maceration), ultrasounds-assisted extraction, microwave-assisted extraction, liquid $CO_2$ extraction, solvent extraction [8]. Ultrasounds-assisted extraction is a fast process (minutes to several hours), compared to conventional maceration (7-15 days) [9-11].

The aim of the current study is to evaluate some bioactive compounds extracted to sunflower oil by ultrasound-assisted procedure from Calendula officinalis, Hypericum perforatum, Galium verum, Taraxacum officinale, Achillea millefolium, Equisetum arvense and Rubus idaeus. These plants were chosen because they are an easy to find raw material, inexpensive and for their anti-inflammatory, wound-healing, antioxidant properties, and for the effect of skin regeneration [12-15]. They are all well characterized regarding their effects by traditional medicine use in rural zones of Romania. Also, this study includes a short characterization of a dermatocosmetic cream formulation containing the above plant extracts.

## RESULTS AND DISCUSSION

### *TLC Identification*

Figures 1a and 1b represent the images obtained after the TLC analysis. Each UAE sample to sunflower oil is characterized by a fingerprint similar to that of the plant with which the oil was enriched, under the proposed TLC conditions. The bioactive compounds were identified based on the

comparison of retention factors (Rf) values with those for the standards separated in the same chromatographic conditions. To eliminate possible interferences, a sample of sunflower oil used in UAE process was also applied.

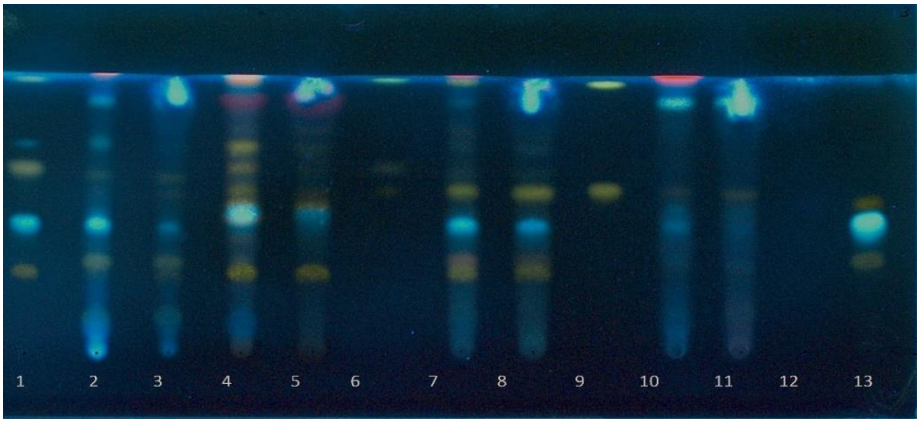


**Figure 1a**: Standard 1 - Rutin, Chlorogenic acid, Apigenin-7-glucoside, Apigenin (1); Calendula officinalis plant - Calendula officinalis UAE sample(2,3); Hypericum perforatum plant - Hypericum perforatum UAE sample (4,5); Standard 2 - Isoquercetin, Kaempferol, Kaempferol-3-glucoside (6); Galium verum plant –Galium verum UAE sample (7,8); Standard 3 - Luteolin, Luteolin-7-glucoside (9); Taraxacum officinale plant - Taraxacum officinale UAE sample (10,11); Sunflower oil (12); Standard 4-Izoramnetin-3-rutinoside, Chlorogenic acid, Hyperoside (13)

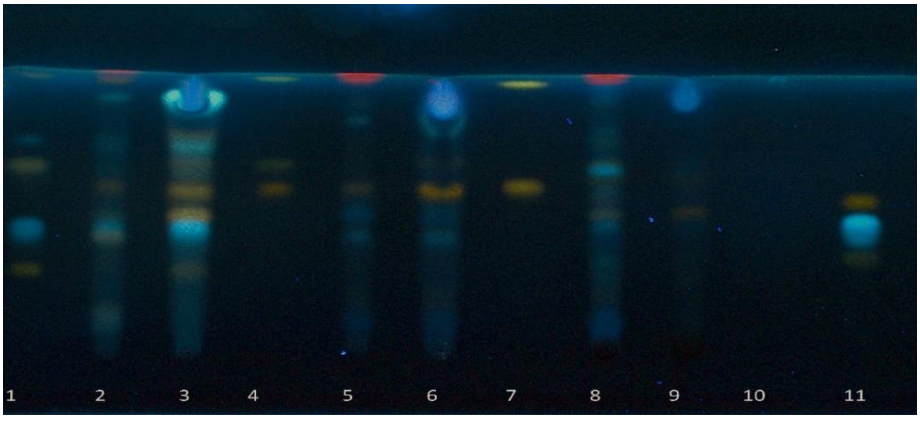


**Figure 1b**: Standard 1 - Rutin, Chlorogenic acid, Apigenin-7-glucoside, Apigenin (1); *Achillea millefolium* plant - *Achillea millefolium* UAE sample (2,3); Standard 2 - Isoquercetin, Kaempferol, Kaempferol-3-glucoside (4); *Equisetum arvense* plant - *Equisetum arvense* UAE sample (5,6); Standard 3 - Luteolin, Luteolin-7-glucoside (7); *Rubus idaeus* plant –*Rubus idaeus* UAE sample (8,9); *Sunflower* oil (10); Standard 4-Izoramnetin-3-rutinoside, Chlorogenic acid, Hyperoside (11).

The results of the TLC analysis show the polyphenolic acid composition of all the UAE samples, but also the presence of various flavones and their glycosides: rutin in *Calendula officinalis* and *Achillea millefolium* UAE samples; luteolin in *Hypericum perforatum*, *Galium verum, Achillea millefolium* and *Equisetum arvense* UAE samples; hyperoside in *Calendula officinalis*, *Taraxacum officinale* and *Rubus idaeus* UAE samples; apigenin glycoside or kaempferol in *Achillea millefolium* and *Equisetum arvense* UAE samples.

### *Quantitative determination of total flavonoids content (TFC) by spectrophotometry in UAE samples*

*Method Validation for UAE sample from Calendula officinalis to sunflower oil*

The method validation was carried out according to the requirements of ICH Q2(R1) [16] for a new product by evaluation the typical validation characteristics as linearity, accuracy, precision and robustness.

*Linearity*: The calibration curve for rutin, based on which the flavonoid content was determined from the UAE samples, is represented in figure 2 and was plotted in the concentration range 2.2µg/mL-176.6µg/mL.

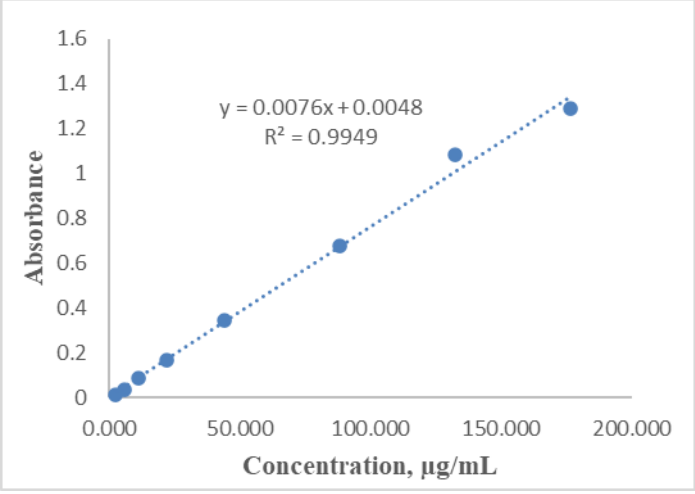


**Figure 2.** Calibration curve for rutin

ANOVA test showed that there was a proportionality relationship between the absorbance and concentration at 95% confidence level. The correlation coefficient of the regression line is 0.9949. The confidence interval of the intercept includes zero value. The statistical significance of the slope is checked by the Student test ($t_{calculated} > t_{critical}$), thus demonstrating the linearity

of the curve. An additional element confirming the linearity of the method is the fulfilment of the condition that the experimental value of the Fisher test is greater than the critical value. Limit of detection (LOD) and limit of quantification (LOQ) were calculated based on the residual standard deviation of the calibration curve (SD) and the slope of the calibration curve (b), where LOD=3.3xSD/b and LOQ=10xSD/b [17].

The results of linearity are summarized in Table 1.

**Table 1.** Linearity verification by ANOVA test

| **Statistical characteristics of the regression** | **Acceptability criteria** | **Rutin** |
|---|---|---|
| Regression line equation | - | y=0.0076x+0.0048 |
| Correlation coefficient | >0.9900 | 0.9949 |
| Determinations, n | - | 8 |
| Degrees of freedom, n-2 | - | 6 |
| Standard error of regression | - | 0.0385 |
| Standard error of slope | - | 0.00022 |
| Student's test $t_{n-2}(1-\alpha/2)$ | $t_{calculated} > t_{critical} = 2.4469$ | 34.12 |
| Confidence interval for slope (95% confidence) | does not include zero value | 0.00704÷ 0.00813 |
| Standard error of intercept | - | 0.01911 |
| Confidence interval for intercept (95% confidence) | include zero value | -0.04196÷0.05158 |
| Fisher test (95% confidence) Fcritical=$F_{1,n-2}(1-\alpha)$= 5.9874 | $F_{calculated} > F_{critical}$ | 1164.2 |
| LOQ (µg/mL) | | 11.7391 |
| LOD (µg/mL) | | 3.8645 |

*Accuracy*

A known amount of standard stock solution of rutin was added at different levels in a placebo solution. The placebo solution was prepared the same way as the samples for analysis by spectrophotometry, but sunflower oil was used instead of UAE sample. Recovery values of 83-88% were achieved for rutin (table 2).

**Table 2.** Accuracy

| **Accuracy** | **Theoretical concentration of rutin, µg/mL** | **Obtained concentration of rutin, µg/mL** | **Recovery, %** | **Acceptability criteria** |
|---|---|---|---|---|
| Level 1 | 11,213 | 9,325±0,01 | 83,16 | R=80-110% |
| Level 2 | 44,851 | 39,711±0,02 | 88,54 | |
| Level 3 | 89,702 | 79,250±0,10 | 88,35 | |

*Precision*

Precision was investigated using six UAE samples from *Calendula officinalis* to sunflower oil prepared and analysed. The result is presented as the average of the measurements and precision expressed as relative standard deviation, RSD=0.71% (Acceptability criteria: RSD ≤ 5%).

*Robustness*

For testing the method robustness, the reaction time was varied, starting from 5min to 60min. In the interval 40-50min, a stable absorbance value was observed.

By meeting all the validation requirements, the analytical method is suitable for quantifying the total flavonoids content in the UAE samples.

The results for TFC of the plants and of UAE samples in sunflower oil, as well as the respective extraction yields, are shown in Table 3.

**Table 3.** Total Flavonoid Content in the plants and UAE samples to sunflower oil

| **Name** | **TFC determined in the ground plant, mg rutin /g average±SD, n=3** | **TFC determined in the UAE sample reported to the plant, mg rutin /g average±SD** | **Extraction Yield %** |
|---|---|---|---|
| *Calendula officinalis* | 5.118±0.073 | 0.448±0.025 (n=6) | 8.75 |
| *Hypericum perforatum* | 5.730±0.007 | 0.717±0.002 (n=3) | 12.51 |
| *Galium verum* | 4.257±0.202 | 0.466±0.018 (n=3) | 10.95 |
| *Taraxacum officinale* | 2.737±0.105 | 0.287±0.010 (n=3) | 10.49 |
| *Achillea millefolium* | 4.638±0.062 | 0.373±0.020 (n=3) | 8.04 |
| *Equisetum arvense* | 3.125±0.126 | 0.540±0.010 (n=3) | 17.28 |
| *Rubus idaeus* | 18.961±0.109 | 1.303±0.015 (n=3) | 6.87 |

After analyzing the individual UAE samples and observing the potential of each one, we prepared an UAE mixture that includes all 7 plants, keeping the plant:oil ratio of 1:10 (w/w). This mixture was used in the formulation of a cream along with a professional cream base which was bought from Ellemental. A mixture solution of 30%sodium benzoate-15%potassium sorbate was added as a preservative.

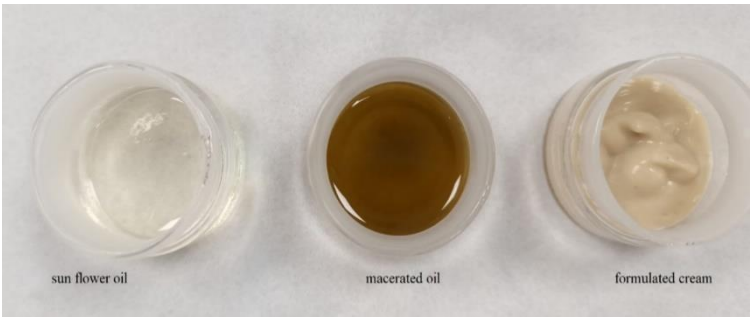


**Figure 3.** Physical properties: Appearance, color

The topical formulation was evaluated for some physicochemical properties: appearance, color, texture, phase separation, homogeneity, viscosity and Ph. The results are expressed as greenish-brown, semisolid, opaque cream (figure 3), with characteristic odour of plants, with smooth texture, and with a homogeneous distribution free from phase separation and foreign particulate matter. The pH is 6.03 and the viscosity is 1538.38cP.

***Formulated cream TLC identification***

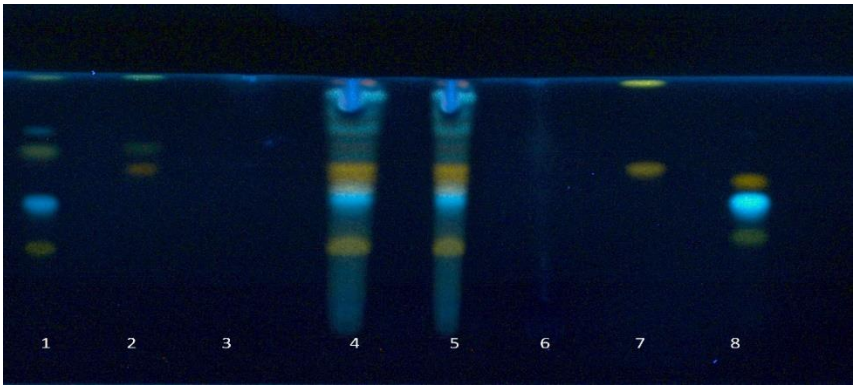


**Figure 4.** Standard 1 - Rutin, Chlorogenic acid, Apigenin-7-glucoside, Apigenin (1), Standard 2 - Isoquercetin, Kaempferol, Kaempferol-3-glucoside (2), Sunflower oil (3), UAE Mixture (4), Formulated cream (5), Cream base (6), Standard 3 - Luteolin, Luteolin-7-glucoside (7), Standard 4-Izoramnetin-3-rutinoside, Chlorogenic acid, Hyperoside (8)

The TLC fingerprint of the cream is similar to the fingerprint of the UAE mixture, demonstrating the presence of polyphenolic compounds and flavonoids in the cream composition.

The content of alpha-tocopherol was determined by a GC-MS method and the evaluation of the antioxidant activity was performed by applying the DPPH indirect spectrophotometric method. The test results for alpha-tocopherol and for the antioxidant activity can be found in table 4.

The results in Table 4 indicates the following aspects: (1) The pure sunflower oil contained 1.15(±0.011) mg/g of alpha-tocopherol, while the mixture of plants in oil 1.53(±0.012) mg/g, which was a significant increase of 33% and (2) Hypericum perforatum and Calendula officinalis UAE samples have the lowest values for EC50 meaning better antioxidant activity than the rest of the selected plants.

**Table 4.** Alpha-tocopherol and antioxidant activity results

| Name | Alpha-tocopherol content (GC-MS), mg/g | DPPH ($EC_{50}$mL) |
|---|---|---|
| *Calendula officinalis UAE sample* | 1.35±0.012<br>RSD = 0.8% | 1,512± 0.016<br>RSD = 0.3% |
| *Hypericum perforatum UAE sample* | 1.28±0.015<br>RSD = 1.2% | 1,415± 0.015<br>RSD = 1.6% |
| *Galium verum UAE sample* | 1.17±0.006<br>RSD = 0.5% | 5,141±0.021<br>RSD = 0,9% |
| *Taraxacum officinale UAE sample* | 1.18±0.006<br>RSD = 0.5% | - |
| *Achillea millefolium UAE sample* | 1.22±0.010<br>RSD = 0.8% | 6.425±0.017<br>RSD = 1.2% |
| *Equisetum arvense UAE sample* | 1.21±0.017<br>RSD = 1.4% | - |
| *Rubus idaeus UAE sample* | 1.28±0.015<br>RSD = 1.2% | - |
| *Sunflower oil* | 1.15±0.011<br>RSD = 0.9% | 8.490±0.045<br>RSD = 1.8% |
| *UAE Mixture* | 1.53±0.012<br>RSD = 0.7% | 0.089±0.011<br>RSD = 1.1% |
| *Cream base* | - | - |
| *Formulated cream* | 0.49±0.006<br>RSD = 1.2%<br>(Recovery = 87%) | 0.5g formulated cream reduces DPPH by 15% |

Also, it can be seen that only a volume of 0.089mL of UAE of the plants mixture reduces DPPH by 50%, which means almost 17 times lower compared to the volume of the pure sunflower oil. Therefore, if the compounds responsible for the antioxidant activity are liposoluble, an increase in the antioxidant activity of our UAE mixture was expected.

Regarding the results for UAE samples, to the best of our knowledge, there is no literature data on the bioactive compounds ultrasound-assisted extraction to sunflower oil from any medicinal plants. In a survey of past literature reports we found studies of extraction from an edible wild plant - *Crithmum maritimum* L. [18] or from a brown macroalga - Pelvetia canaliculate L. [19] to sunflower oil during ultrasound-assisted treatment, with the purpose of increasing the nutritional value and oxidative stability of the oil. In both studies, the extraction yields of flavonoids to the oil were rather low, ranging from 1.9% to 3.4% and from 0.85% to around 9.40%, respectively for different concentration of each lyophilized plant added to sunflower oil (5-20% m/v). These results were explained by the presence of low soluble flavonoid compounds of C. maritimum and of *P. canaliculata* in the oil which acts as a non-polar solvent. Also, the authors reported higher antioxidant activity in supplemented sunflower oil samples

from Crithmum maritimum and Pelvetia canaliculate, respectively than in the non-supplemented oil, indicating that the compounds with antioxidant activity that migrated from the plants studied to the oil are mainly non-polar.

## CONCLUSIONS

Our study presents, for the first time, the extraction of bioactive compounds from the selected medicinal plants to sunflower oil by non-pollutant ultrasound-assisted technique and the evaluation of total flavonoid content, alpha-topherol content of these extracts, as well as their antioxidant activity.

TLC fingerprints showed the chemical composition similarity of the plants extracts obtained by ultrasound-assisted extraction in sunflower oil with the plants studied in this work, concerning the presence of characteristic polyphenolic acids and flavonoids. UV-VIS spectrophotometry and GC-MS analysis were used to quantify total flavonoids and alpha-tocopherol content.

The antioxidant potential was investigated by DPPH assay. The UAE sample of the all plants mixture showed a higher antioxidant activity compared to the pure sunflower oil, probably due to a synergistic effect of phenolic and flavonoid compounds with the antioxidant molecules of α-tocopherol.

The active principles from the selected plants incorporated by ultrasounds-assisted extraction into sunflower oil, are found in the cream formulation presented in this work. This fact was demonstrated by the presence of the same bioactive compounds as in the UAE sample of the plants mixture revealed by TLC analysis and by a level of 87% of alpha-tocopherol which makes the cream preparation a good candidate for repairing the epidermis. Also, due to the oily plant extract, formulated cream has a certain antioxidant activity (0.5g reduces DPPH by 15%).

Thus, this green approach of ultrasound-assisted extraction is of great interest providing a good alternative to conventional extractions; it can be used for the extraction of valuable compounds from a large number of plants. The use of sunflower oil as natural solvent facilitates the application of the ultra-assisted extracts from medicinal plants for dermatocosmetic preparations.

## EXPERIMENTAL SECTION

Materials: We used cold-pressed sunflower oil from a local producer from Horezu, Valcea area and 7 dried and crushed plants (aerial parts and leaves) bought from Dacia Plant: *Calendula officinalis, Hypericum perforatum, Galium verum, Taraxacum officinale, Achillea millefolium, Equisetum arvense* and *Rubus idaeus.*

Reagents: polyphenolic acid standards - Chlorogenic acid (Sigma), flavones: Apigenin (Toronto Research Chemicals), Isoquercetin (Chromadex), Kaempferol (Santa Cruz), Luteolin (Santa Cruz) and glycosides of flavones (flavonoids) - Rutin ( Sigma), Kaempferol-3-glucoside (Santa Cruz), Apigenin-7-glucoside (EP), Luteolin-7-glucoside (Sigma), Izoramnetin-3-rutinoside (PhytoLab), Hyperoside (TRC); Methanol (Carlo Erba, HPLC grade); Aluminum chloride (Sigma,); Ethyl acetate (Carlo Erba); Formic acid (Merck, 99%); Sodium acetate (Sigma, 99%); Diphenylboric acid aminoethyl ester (Merck); Macrogol 400 R (Merck), Alpha-tocopherol (Sigma), Hexane (Merck), Dimethylsulfoxide (DMSO, Sigma), 2,2-Diphenyl-1-Picrylhydrazyl (DPPH, Sigma).

Ultrasound-assisted extraction: Each crushed plant sample is covered with sunflower oil in a plant-oil ratio of 1:10(w/w) and is ultrasonicated at room temperature (23–25°C) for 3hours, in a ultrasonic bath Bandelin Sonorex (ultrasounds were applied with a frequency of 35 kHz). Each extract is filtered and stored at 4 °C in airtight brown containers until further use.

***Samples for thin layer chromatography analysis***

Every extract was homogenized in methanol (HPLC grade) by ultrasonication, then centrifuged. An aliquot of the methanol layer was applied on the chromatographic plate.

For comparison, each crushed plant sample was mixed with methanol (HPLC grade), ultrasonicated, filtrated, and the filtrate was used for TLC analysis.

For identification, four mixtures of standard substances were prepared: Standard 1 - Rutin, Chlorogenic acid, Apigenin-7-glucoside, Apigenin; Standard 2 - Isoquercetin, Kaempferol, Kaempferol-3-glucoside; Standard 3 - Luteolin, Luteolin-7-glucoside; Standard 4-Izoramnetin-3-rutinoside, Chlorogenic acid, Hyperoside.

*Samples for UV-VIS spectrophotometry analysis*: Every UAE sample was mixed with purified water, ultrasonicated for 15 minutes for flavonoids extraction, then transferred into a separation funnel for layers separation. The aqueous layer was filtrated through 0.45µm Nylon syringe filter and used for quantitative UV-VIS spectrophotometry analysis.

In parallel, an amount of each crushed plant was mixed with purified water, ultrasonicated for 15 minutes, filtrated through 0.45µm Nylon syringe filter and used for analysis.

***Qualitative analysis by thin layer chromatography (TLC)***

The analysis method was adapted, starting from the European Pharmacopoeia method (11$^{th}$ edition, monograph 1297 "Calendula flower (Calendula flos)"[20-22].

TLC separation was performed on HPTLC Silicagel 60 F254 chromatographic plates, 2-10µm, 20x20cm (Merck). 4µL of each sample prepared for TLC analysis were applied. Then, the plates were developed in the mobile phase: anhydrous formic acid - water - ethyl acetate (10:10:80 v/v/v) on a migration distance of 70mm from the lower edge of the plate. The plates were dried for 5 minutes in air flow, at room temperature and then heated at 100-105°C for 5 minutes. The detection was carried out immediately by spraying with a solution of aminoethyl diphenylboric acid ester 10g/L in methanol R, and then with a solution of macrogol 400 R 50g/L in methanol, after which it was left to dry in the air for 1 minute. Finally, the plates were visualized by ultraviolet examination at a wavelength of 366nm.

***Quantitative analysis of TFC by UV-VIS spectrophotometry***

TFC was determined using aluminium chloride in a colorimetric method described in the Romanian Pharmacopoeia X [23] modified for this work .

The determination was based on a complexation reaction of flavonoids with aluminum chloride and measuring the complex absorbance at a wavelength of 430nm [24, 25]. UV-VIS measurements were carried out on Specord 250 Plus instrument using 10mm optical path cells.

To a volume of 5mL of each sample for UV-VIS spectrophotometry analysis 5mL of sodium acetate solution 100g/L was added, then filtered on a 0.45µm nylon filter membrane. In each test tube 5mL of this filtrate were mixed with 2mL of $AlCl_3$ 25g/L solution and 3mL of purified water. The complex was stirred for 5 seconds, left to rest for 45 minutes and then the absorbance was measured at 430nm against a control sample in which aluminium chloride is replaced by purified water. The total flavonoid content was calculated using a calibration curve for rutin as standard. The result is expressed as mg rutin equivalents per gram and reported as the mean ± standard deviation (Mean±SD, n=3).

***Quantitative analysis of alpha-tocopherol***

The determination of the content in alpha-tocopherol is based on its separation by gas chromatography with mass spectrometry detection. Quantification was performed by the method of the external standard. Identification is based on the retention time of standard substance and confirmed with the help of the NIST mass spectra library. The equipment used was a 7890A gas chromatograph coupled with MSD 5975C (“Mass Selective Detector”; electron impact ionization source and quadrupole mass analyzer).

Chromatographic separation was achieved on a capillary column ZB-5MS (60mx0.25mmx0.25µm) [26], using helium with a flow rate of 1.2mL/min and sample injection in split mode (split ratio of 20:1). The mass spectra were

acquired in full scan mode with mass range of 50-600 a.m.u. The oven program increases from 100°C to 300°C with a rate of 10°C /min, where it stays for 30 min. The inlet temperature was 250°C, the interface temperature 260°C, ionization source temperature: 230°C and quadrupole temperature 150°C.

All samples were solubilized in hexane by ultrasonication for 10 min and centrifugation for 15min at 20°C. 1µL of the hexane layer was injected into the GC-MS. The concentration of alpha-tocopherol was calculated on from a calibration curve plotted in the concentration range 0.102-0.340mg/mL ($R^2$=0.9908). The limit of quantification LOQ was 0.102mg/mL. The result is expressed as mg alpha-tocopherol per gram and reported as the mean ± standard deviation (Mean±SD, n=3).

***Antioxidant/antiradical activity***

The evaluation of the antioxidant/antiradical activity of the plant extracts in sunflower oil was performed by applying the indirect DPPH spectrophotometric method, according to M. Rahmani et all [27], which involves recording the decrease in absorbance at wavelength λ= 520nm (maximum DPPH absorption). This decrease is proportional to the concentration of free radicals reduced in solution. The ability of extracts to capture the DPPH* radical is determined by the magnitude of the oxidation-reducing potential of molecules with antioxidant properties present in the composition of the extract. Antiradical activity (AAR) was defined as the amount of antioxidant needed to reduce the initial concentration of DPPH* by 50% and represents the effective concentration, EC50. The absorbance was recorded using a PerkinElmer Lambda 25 UV-Vis spectrophotometer equipped with a sample thermostat system.

All samples were solubilized in DMSO, then different volumes of sample solution were incubated for 30min with 0.004% DPPH solution. After 30min, the absorbance was measured at wavelength λ = 520nm. A curve is plotted for different sample volumes and the absorbance measured values. The volume required for EC50 inhibition was estimated based on this curve. The antioxidant activity is expressed as $EC_{50}$ in mL. The results are reported as the mean ± standard deviation (Mean±SD, n=3).

***Physicochemical tests for the formulated cream***

Physical appearance and color were evaluated by visual observation. Homogeneity and texture were tested by pressing a small quantity of the formulated cream between the thumb and index finger. The consistency of the formulation and presence of coarse particles (*particule grosiere*) were used to evaluate the texture and homogeneity of the formulation.

### *Viscosity Measurement*

A Brookfield viscometer DV-I (Brookfield Engineering Laboratories, Middleboro, MA) was used with a concentric cylinder spindle to determine the viscosity of the formulated cream. The tests were carried out at 21°C. The spindle was rotated at 0, 0.5, 1, 2, 2.5, 4, 5, 10, 20, 50, and 100 rpm values. All measurements were made in triplicate.

### *pH Values*

The pH was determined using a pH-meter (Mettler-Toledo Seven470). Measurements were made in triplicate. The InLaB ISM sensor was calibrated with standard buffer solutions (pH 2, 4, 7 and 9.21) before each use.

## ACKNOWLEDGMENTS

The author Mălina Fiastru-Irimescu gratefully acknowledge Prof. Denisa Margină, for support and guidance, and Biotehnos SA for material support.

## REFERENCES

1. F. Kantawong, S. Singhatong, A. Srilamay, K. Boonyuen, N. Mooti, P. Wanachantararak, T. Kuboki, *Bioimpacts*, **2017**, *7(1),* 13-23
2. B. Arabsorkhi, E. Pourabdollah, M. Mashadi, *Food Chem. Adv.*, **2023**, *2*, 100246
3. K.M. Shahunja, T. Ahmed, M.I. Hossain, M. Mahfuz, L. Kendall, X. Zhu, K. Singh, J.M. Crowther, S. Singh, R.A. Gibson, G.L. Darmstadt, *J Glob Health.*, **2020**, *10(1),* 010414
4. I. B. Karakoç, B. Ekici, *Advances in Skin & Wound Care*, **2022**, 35(12), 1-8
5. T.K. Lin, L Zhong, J.L. Santiago, *Int J Mol Sci.*, **2017** ,*27*, 19(1), 70
6. A. Ahmad Warra, N. G. Anka, *Pathogens.American J. Ethnomedicine*, *1(3),* 147-151
7. J. Pavlačková, K. Kovacsová , P Radiměřský, P Egner , J. Sedlaříková , P Mokrejš, *Brazilian Journal of Pharmaceutical Sciences*, **2018**, *54(3),* 17693
8. A. E. Ince, S. Sahin, G. Sumnu, *J. Food Sci. Technol.*, **2014**, *51*, 10, 2776–2782
9. V. Perceval Soares, M. Bittencourt Fagundes, D. Rigo Guerra, Y. Sena Vaz Leães, C. Sefrin Speroni, S. Sasso Robalo, T. Emanuelli, A. J. Cichoski, R. Wagner, J. Smanioto Barin, D. Assumpção Bertuol, C. Augusto Ballus, *Food Res. Int.*, **2020**, 135
10. O. Jović, I. Habinovec, N. Galić , M. Andrašec, *Hindawi J. Spectroscopy*, **2018,** 9
11. Y. Moustakime, Z. Hazzoumi, K. Amrani Joutei, *Grain & Oil Sci. Technol.*, **2021**, *4*, 108–1244
12. D. Turcov, A.S Barna, A.Trifan, A.C. Blaga, A.M Tanas˘a, D. Suteu*, Plants*, **2022**, *11*, 2454

13. K. M. Alsaraf, I S. Abbas, E F. Hassan, *IOP Conf. Ser.: Mater. Sci.Eng*., **2019**, 571.
*14.* F. Scotti, K. Löbel, A. Booker, M. Heinrich, *Frontiers in Plant Science*, **2019**, *9*
*15.* T. Belwal, H. Prasad Devkota, M. Kumar Singh, R. Sharma, S. Upadhayay, C. Joshi, K. Bisht, J. Kumar Gour, I. D. Bhatt, R. S. Rawal, V. Pande, *Academic Press*, **2019**, 415-432
16.ICH Q2(R1) guideline
17.S. L. R. Ellison, V. J. Barwick, T. J. Duguid Farrant - *Practical Statistic for the Analytical Scientist*, **2009**
18. G. Sousa, M.I. Alves, M. Neves, C. Tecelão, S. Ferreira-Dias, *Foods*, **2022**, *11*, 439
19. G. Sousa, M. Trifunovska, M. Antunes, I. Miranda, M. Moldão, V. Alves, R. Vidrih, P.A. Lopes, L. Aparicio, M. Neves, **Foods**, **2021**, *10*, 1732
20. European Pharmacopoeia 11, 1297
21. H. Wagner, S. Bladt, *Plant Drug Analysis: A Thin Layer Chromatography Atlas*, Springer, **1996**
22. Li ZH, Guo H, Xu WB, Ge J, Li X, Alimu M, He DJ, *J Chromatogr Sci*., **2016** *54(5),* 805-10
23. Romanian Pharmacopoeia X
24. R.T.M. Ramos, I.C.F. Bezerra, M.R.A. Ferreira, L.A.L. Soares, *Pharmacognosy Res.*, **2017**, *9(3),* 253-260
25. L. Fagundes Soares, L. C. Machado, E. J. Pelegrini dos Santos, D. Gonçalves Bezerra, L. L. Borges, V. C. Santana Amaral, J. Realino de Paula, J. A. Marciano de Paula, *Res. Society Development*, **2022**, *11*, 3
26. R.Zhang, W. Shen X. Wei, F. Zhang, C. Shen, B. Wu, Z. Zhao, H. Liu , X. Deng, *Anal. Methods*, **2016**, *8*, 7341-7346
27. M. Rahmani, L. Hamel, F. Toumi-Benali, M.M. Dif, F. Moumen, H. Rahmani, *J. Mater. Environ. Sci.*, **2018** ,*9*, 6, 1656-1661.

STUDIA UBB CHEMIA, LXIX, 2, 2024 (p. 81-96)
(RECOMMENDED CITATION)
DOI:10.24193/subbchem.2024.2.06

# GOLD NANOPARTICLES SYNTHESIZED WITH NATURAL COMPOUNDS: ASSESMENT OF ANTIOXIDANT ACTIVITY AFTER *IN VITRO* DIGESTION

**Dalina Diana ZUGRAVU (POP)[a], Teodora MOCAN[a], Andrei Vasile POP[b], Valentina MOROSAN[c*], Luminita DAVID[c], Simona Valeria CLICHICI[a]**

**ABSTRACT.** Currently, gold nanoparticles (GNPs) are considered an ideal delivery system due to their physiological stability, high bioactivity, and controlled release of biological component. Our primary objective was to comprehend the behavior of gold nanoparticles obtained with specific natural compounds in the gastrointestinal tract. We investigated the conduct of GNPs synthesized with natural compounds from *Cornus mas* L. (GNPs-CM) or *Sambucus nigra* (GNPs-E) fruits, during the oral, gastric, and intestinal phases of the *in vitro* simulated gastrointestinal digestion. Additionally, we assessed their antioxidant capacity, phenolic content, and their potential to mitigate damages caused by nitro-oxidative stress after each phase of *in vitro* digestion. Results indicated that both GNPs-CM and GNPs-E maintained stability throughout simulated digestion, with some observed differences between them. Upon measuring antioxidant capacity, the GNPs-CM exhibited the lowest percentage of inhibition from hydrogen donor measurements (12.08%) after the simulated intestinal phase. Conversely, the GNPs-E displayed the highest inhibition percentage (65.3%) after the simulated oral phase. Concerning phenolic content, GNPs-CM showed a polyphenol content of 39.53 mg of gallic acid equivalents (GAE)/L, decreasing during gastrointestinal phases. GNPs-Eexhibited a polyphenol content of 100.99 mg GAE /l, also decreasing during gastrointestinal phases.

[a] *Department of Physiology, Faculty of Medicine, "Iuliu Haţieganu" University of Medicine and Pharmacy, 8, V. Babeş Str., 400012, Cluj-Napoca, Romania.*
[b] *2nd Medical Department, "Iuliu Haţieganu" University of Medicine and Pharmacy, Cluj-Napoca, Romania.*
[c] *Department of Chemistry, Faculty of Chemistry and Chemical Engineering, "Babeş-Bolyai" University, 11, A. Janos Str., 400028, Cluj-Napoca, Romania*
* *Valentina Moroşan valentina.morosan@ubbcluj.ro*

***Keywords:*** *gold nanoparticles, simulated gastrointestinal digestion, Cornus mas L., Sambucus nigra L., nitro oxidative stress, antioxidant capacity, phenolic content.*

## INTRODUCTION

Gold nanoparticles (GNPs) have emerged as a versatile and promising platform in the realm of nanotechnology for a multitude of applications, particularly in the field of drug delivery and therapeutics [1,2]. Their unique physicochemical properties, including size, shape, and surface characteristics, make them ideal candidates for functionalization with biocompatible ligands [3,4].

In recent years, the integration of natural compounds, derived from plants and recognized for their inherent biocompatibility and diverse biological activities, has significantly advanced the capabilities of GNPs in the context of medical applications. The gastrointestinal tract, encompassing the stomach, small intestine, and large intestine, represents a critical portal for the oral administration of drugs and therapeutic agents [3,4]. Effective delivery of these agents to specific sites within the gastrointestinal system relies on understanding and harnessing the behavior of nanoparticles in this dynamic and complex environment.

Factors including pH gradients, enzymatic activity, mucosal barriers, and transit times present substantial challenges to the efficacy of nanoparticle-based drug delivery systems. Consequently, there is a pronounced need for strategic approaches tailored to augment nanoparticle stability and bioavailability to overcome these challenges.

Joining nanoparticles and bioactive compounds promises to revolutionize the field of oral drug delivery. This offers opportunities for tailored therapies that exhibit enhanced bioavailability, reduced side effects, and improved patient compliance. It can contribute to the development of personalized medicine, where therapies can be fine-tuned to individual patient needs and conditions. For instance, a recent study demonstrated the synthesis of GNPs with different sizes and morphologies using a single LTCC-based microfluidic system for point-of-care use in personalized medicine. The study showed that depending on the temperature, residence time, and citrate concentration chosen during synthesis, a range of nanoparticle sizes and shapes were consistently produced. This indicates that the process could be suitable for the production of nanoparticles for personalized medicine [3].

The behavior of GNPs functionalized with natural compounds in the gastrointestinal tract opens a gateway to innovative approaches in pharmaceutical science, with far-reaching implications for drug delivery.

Nanotherapy is a cutting-edge therapeutic approach that uses nanoparticles to deliver drugs into specific targeted cells. The process is based on nanoparticles specific characteristics including their size, core composition, shape and surface functionalization. Due to their capacity to cross numerous biological barriers and release a therapeutic load in the ideal dosage range, nanoparticles drug delivery systems (5-250 nm) have the potential to revolutionize current disease therapies. [5]

Nanostructured coatings and surface tailoring can be applied to the outside of a matrix to improve or enhance its efficiency. Gold nanoparticles can deliver a variety of drug molecules, from tiny ones to large biomolecules like peptides, proteins, or nucleic acids like DNA or RNA. Numerous molecules with the proper functional groups could be used to functionalize gold nanoparticles. The synthesis of GNPs is achieved with nontoxic effects, obtaining unique biological, physiochemical, and optical features [6,7].

In various *in vitro* and *in vivo* experiments, multiple studies have consistently observed no adverse biological effects associated with GNPs. It is noteworthy that certain observed effects are attributed to compounds linked to the GNPs, rather than the GNPs themselves. Recent research has showcased the anti-inflammatory effects of GNPs functionalized with natural compounds in mice, evidencing a reduction in IL-6 mRNA and TNF-α levels [8]. Investigations on gold nanoparticles (GNPs) have underscored the significance of composition, surface derivatization, charge, size, and shape in determining their interaction with biological systems. The toxicity of GNPs is influenced by surface functionalization, necessitating individual evaluation of each unique nanomaterial. The application of DNA-GNPs for genetic regulation and amine-functionalized conjugates for drug delivery exemplify the potential of GNPs, with toxicity lower than polymer delivery systems. The field of functionalized gold nanoconjugates continues to evolve, offering potential applications in biology and medicine [9].

Belonging to the Cornaceae family, *Cornus mas* is native to South-West Asia and South-East Europe. Employed in traditional medicine for over a millennium, it has been particularly utilized for addressing digestive disorders [10]. The therapeutic potential of *Cornus mas* is substantial, primarily owing to its remarkable antioxidant capabilities derived from a rich composition of phytochemical compounds [11,12]. Noteworthy among these are significant amounts of phenolic compounds such as caffeic acid, ellagic acid, anthocyanins, and flavonoids [13]. *Cornus mas* finds widespread application in treating various conditions, including gastrointestinal disorders, diabetes, malaria,

inflammatory processes, and obesity [14]. The consumption of CM is deemed safe with no reported side effects, as indicated by toxicity studies. However, before categorizing CM as an herbal drug, it is essential to conduct extensive toxicity research and evaluate the effects of high doses [15].

Given its positive impact on gastrointestinal disorders coupled with its antioxidant and anti-inflammatory attributes, we explored the potential synergies by associating *Cornus mas* phytocomponents with GNPs. The aim was to leverage the combined effects of natural compounds of *Cornus mas* fruits and GNPs. Building on this premise, we investigated the behavior of nanoparticles synthesized with *Cornus mas* fruit extract in the digestive tract [16].

Elderberry, scientifically known as *Sambucus nigra* L., is a prevalent species within the Caprifoliaceae family, thriving in sunlit areas across Europe, Asia, North Africa, and the USA. The concentrated presence of health beneficial compounds in elderberries suggests that their consumption may contribute to the prevention of various degenerative illnesses, including diabetes, cancer, inflammatory diseases, and cardiovascular conditions [17]. *Sambucus nigra* assumes significance in medicine due to its chemical composition, encompassing phenolic acids, essential oils, flavonoids, free fatty acids, glycosides, vitamins, carotenoids, and minerals [18].

Phenolic acids represent key metabolites found in elderberry flowers and fruits, displaying significant antioxidant activities both *in vivo* and *in vitro* [19]. These compounds exhibit diverse biological effects, including antiviral, anti-carcinogenic, vaso-protective, anti-allergic, and anti-inflammatory properties [20]. Noteworthy for their antibacterial and antiproliferative activities, these compounds contribute to the antioxidant role of *Sambucus nigra* compounds. Given its antiproliferative and antioxidant properties, *Sambucus nigra* fruits emerged as a suitable candidate for our study [21,22].

To effectively apply gold nanoparticles in the real biological context, a deeper understanding of the potential interactions between biomolecules and gold nanoparticle materials, both *in vivo* and *in vitro*, is imperative. A key focus of research involves exploring the interactions among various biomolecules and nanoparticle materials. These interactions play a pivotal role in influencing the biological activity, stability, outcomes, and toxicity of nanoparticle bioconjugate materials in both *in vitro* and *in vivo* settings [23].

**Aim:** Our primary objective was to elucidate the behaviour of gold nanoparticles synthesized with specific natural compounds within the gastrointestinal tract. We investigated the conduct of GNPs obtained with either *Cornus mas* L. or *Sambucus nigra* fruits extracts throughout the oral, gastric, and intestinal phases, employing simulated gastrointestinal fluids. The secondary aim was to evaluate their antioxidant capacity following each phase of *in vitro* digestion, along with assessing their phenolic content.

## RESULTS AND DISCUSSION

### *I. Synthesis and characterization of gold nanoparticles*

The synthesis of gold nanoparticles was achieved by reducing gold ions from the tetrachloroauric acid by natural compounds from *Cornus mas* and *Sambucus nigra* fruits extracts.

The development of the gold ions reduction reaction and the formation of colloidal gold was spectroscopically monitored. In both cases, the UV-Vis spectrum of the biosynthesized gold nanoparticles exhibits the characteristic SPR band for metallic gold: $\lambda_{max}$ = 541 nm for GNPs-CM and 543 nm for GNPs-E (Figure 1).

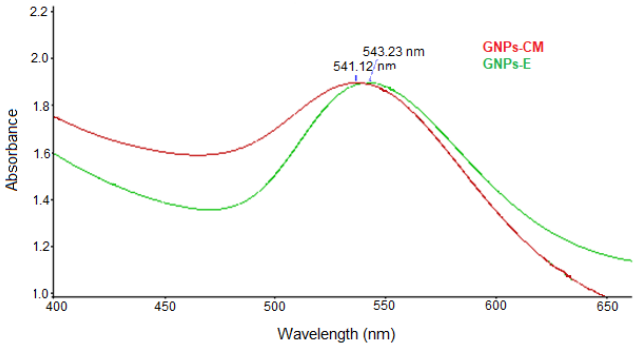


**Figure 1.** UV-Vis spectra of green synthesized gold nanoparticles

Transmission electron microscopy was used to determine the size and shape of newly obtained gold nanoparticles which, according to TEM images (Figure 2), were almost spherical, with a mean diameter of 42 ± 2.42 nm (GNPs-CM) and 44 ± 1.48 nm (GNPs-E), respectively.

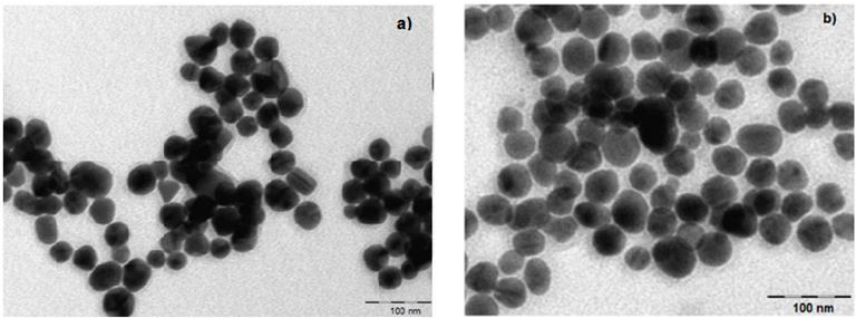


**Figure 2.** TEM images of: a) GNPs-CM; b) GNPs-E

### *II. In-vitro simulation*

#### *II.1. Macroscopic observation*

Phytoreduced nanomaterial GNPs-CM demonstrated physical stability across all three phases of *in vitro* digestion. No color shifts were observed across phases. (Figure 3) No visible sediment, as a mark of particle aggregation, could be detected following the individual phases of *in vitro* simulated digestion for GNPs-CM / GNPs-E. Progressive dilution protocol resulted in decreased color intensity as the experiment moved toward the last step. However, color range remained stable, no significant red of blue shift could be observed across phases.

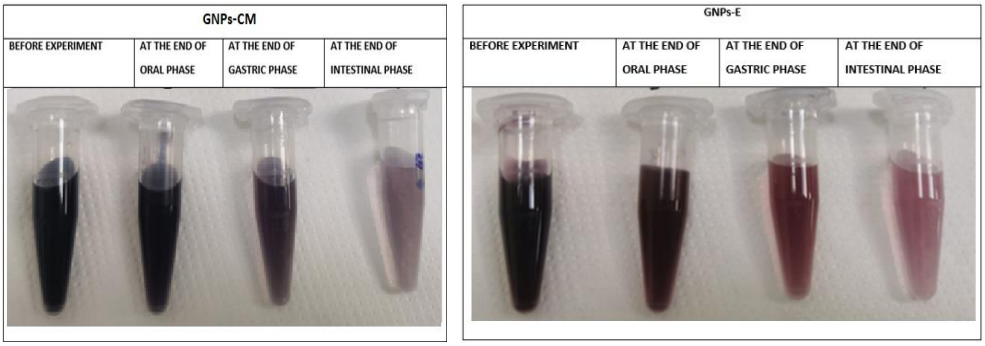


**Figure 3.** Macroscopic aspect of GNPs-CM and GNPs-Esolutions at various steps of *in vitro* gastrointestinal transit simulation.

#### *II.2. UV-Vis Spectroscopy Evaluation*

The UV-Vis spectra demonstrate stability for both structures across the digestive transit simulation (Figure 4 and 5).

#### *II.3. Dynamic Light Scattering*

Dynamic Light Scattering (DLS) analysis before the digestive *in vitro* simulation as well as at the end of each phase reveals a polydispersed solution. The pre-digestion sample of GNPs-CM presented a polydispersity index (PdI): 0.696, Peak 1: 294.9 ±67.20 nm cumulating 70.9 % of particles, Peak 2: 76.76±12.76 nm cumulating 29.1%. Following the oral phase, the obtained values were: PdI: 0.411, Peak 1: 514.0±99.56 nm cumulating 85.6% of nanostructures, Peak 2: 182.2±35.39 nm joining 14.4% of nanoparticles. At the end of the gastric phase, we obtained PdI: 0.488, Peak 1: 288.8± 165.8

nm cumulating 98.7% of nanostructures, Peak 2: 5289± 411.3 nm for 1.3% of nanoparticles. At the end of the experiment, PdI: 0.572, the initial Peak 1: 125.2± 39.35nm is found as cumulating 62.8%, Peak 2: 457.8± 124.5 nm appeared cumulating 27.7%, and Peak 3: 24.03± 4.42 nm cumulating 7.8% of nanoparticles. The complete disappearance of the smaller population, visible before the intestinal phase was observed. (Figure 5a).

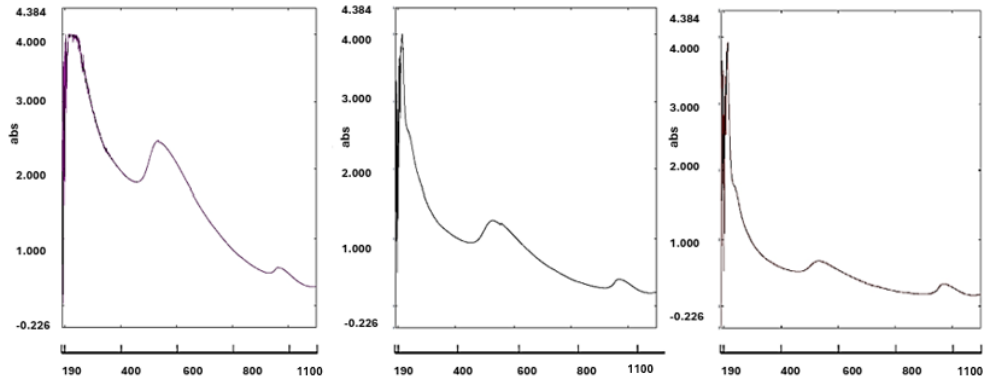


a)

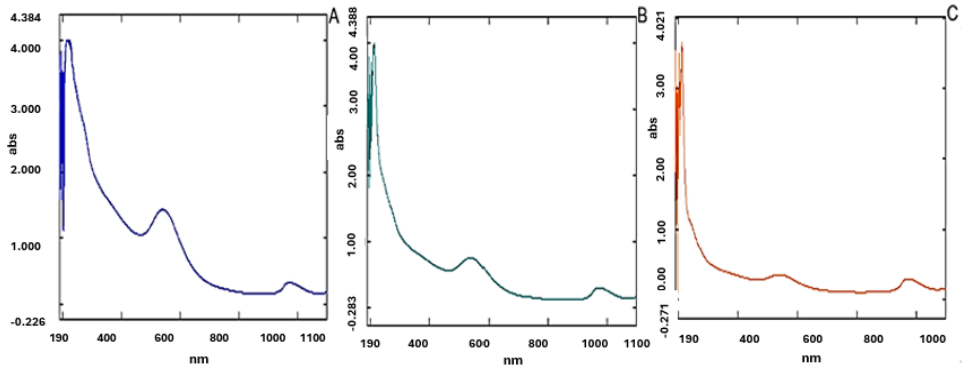


b)

**Figure 4.** UV-VIS spectra of a) GNPs-CM and b) GNPs-E samples resulting from *in vitro* digestive exposure steps. A. Sample at the end of SSF exposure. B. Sample at the end of SSF and SGF exposure steps, in respective order. C. Sample at the end of SSF, SGF and SIF exposure steps, in respective order.

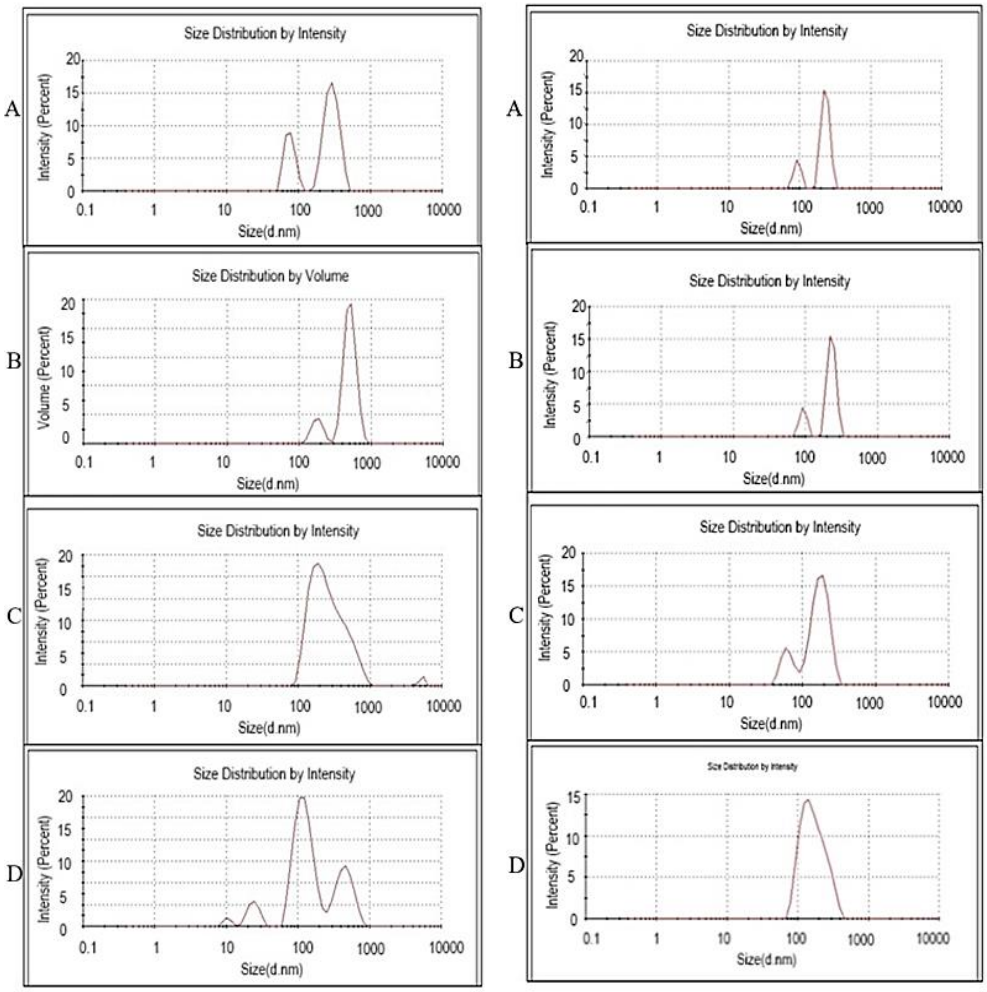


**Figure 5.** DLS analysis of samples following exposure of: a) GNPs-CM and b) GNPs-E to digestive simulated fluids. A. Sample before exposure to simulated digestive fluids. B. Sample at the end of SSF exposure. C. Sample at the end of SSF and SGF exposure steps, in respective order. D. Sample at the end of SSF, SGF and SIF exposure steps, in respective order.

For GNPs-E, DLS analyses before the digestive *in vitro* simulation as well as after each phase of the *in vitro* digestion process reveal a polydispersed solution. A small population of nanoparticles is also visible.

Control sample returned a polydispersity index (PdI): 0.314, Peak 1: 153.1± 36.30 nm cumulating 98.1% of particles. Following the oral phase values remained similar: PdI: 0.411, Peak 1: 233.4± 31.06 nm cumulating 82.1% of nanostructures, Peak 2: 93.5± 9.52nm nm joining 17.9% of nanoparticles. At the end of gastric phase, we have obtained PdI: 0.488, Peak 1: 180.2± 47.18 nm cumulating 80.1% of nanostructures, Peak 2: 64.08± 13.13nm for 19.9% of nanoparticles. Interestingly, the last intestinal step in digestive *in vitro* simulation induced a modification of the hydrodynamic diameter. At the end of the experiment, PdI: 0.572, the initial Peak 1: 174.6±69.66nm is found as cumulating 100%. Disappearance of the smaller population, visible before the intestinal phase was also observed at the end of the experiment (Figure 5b).

### *II.4. Assessment of Antioxidant Capacity through DPPH Inhibition*

After measuring the antioxidant capacity, the lowest percentage of inhibition of DPPH from the measurements of hydrogen donors was presented by the GNPs-CM (12.08%) after simulated intestinal phase, followed by GNPs-CM exposed at simulated gastric phase (13.76%) and GNPs-CM exposed to simulated salivary fluids (20.79%) (Figure 8). It was observed that the GNPs-E after simulated oral digestion presented the highest inhibition percentage (65.3%), followed by GNPS-E before digestion (50.5%) and GNPs-E after simulated gastric phase (33.39%). A close percentage of inhibition was determined for both GNPs-CM (21.68%) and GNPs-E(22.57%) exposed at simulated intestinal fluid (Figure 6).

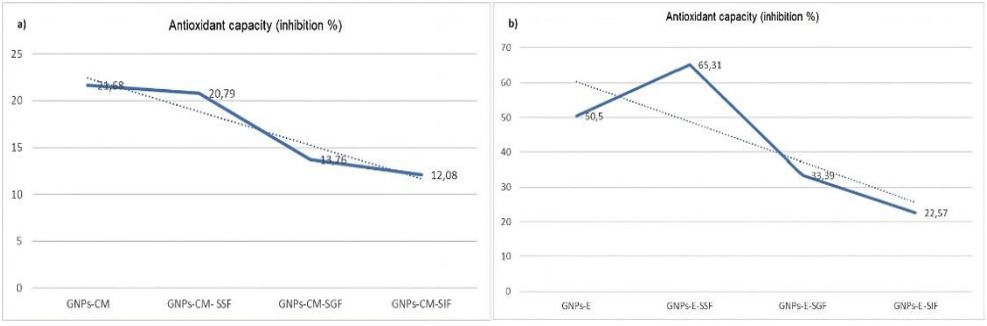


**Figure 6.** Inhibition percentage for: a) GNPs-CM and b) GNPs-E during gastrointestinal phases; GNPSs-CM, GNPs-E= gold nanoparticles before digestion; GNPs-CM-SSF, GNPs-E-SSF = gold nanoparticles exposed to simulated salivary fluid; GNPs-CM-SGF, GNPs-E-SSF = gold nanoparticles after simulated gastric digestion; GNPs-CM-SIF, GNPs-E-SSF = gold nanoparticles exposed to simulated intestinal fluid

*II.5. Polyphenolic content*

Regarding the polyphenolic content, our results showed that GNPS-CM have a polyphenol content in the amount of 39.53 mg of gallic acid equivalents (GAE)/L, this amount decreasing during the gastrointestinal phases, after exposure at SSF being 24.25 mg GAE/L, after exposure at SGF being 18.65 mg GAE/L and after the final phase of digestion being 8.43 mg GAE/L (Figure 7).

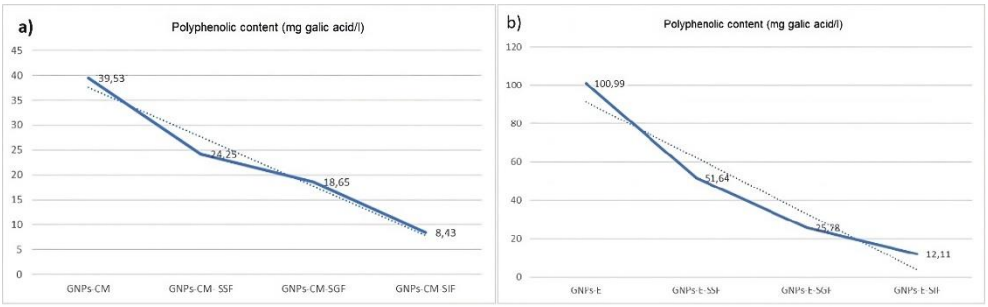


**Figure 7.** Phenolic content of: a) GNPs-CM and b) GNPs-Eduring gastrointestinal phases.

As far as GNPs-E is concerned, it has a polyphenol content of 100.99 mg gallic acid equivalents/L, also decreasing during the gastrointestinal phases: SSF 51.64 mg GAE/L, SGF 25.78 mg GAE/L, and SIF 12.11 mg GAE/L.

Both GNPs-CM and GNPs-E were stable across simulated digestion. However, differences were observed between the two. GNPs-E demonstrates stable interactions between natural compounds from the fruit extract and metallic component. It furthermore slightly increased the hydrodynamic diameter of the particles along the experiment, up to the end of the intestinal phase. Detachment of natural compounds from the metallic core is observed in the gastric stage. End-experiment sizes of particles are slightly larger than the pre-experiment dimensions. All data suggest a stabilization and reattachment of extract molecules in the intestinal phase, following a previous separation during the gastric phase.

By contrast, GNPs-CM nanoparticles transiently increase their dimension during the salivary phase, most likely by attachment of amylase onto the surface of the metallic core. Next, the gastric phase is associated with a decrease in hydrodynamic diameter, as a sign of detachment of extract's biomolecules from the nanoparticles' surface. This aspect is similarly present in most

nanoparticles (98.7%). Following this step, the intestinal phase induces a different result. Multiple particle populations are seen at the end of the experiment. A distinct fraction of components has small dimensions, the aspect suggesting detachment of extract molecules from the metallic surface of nanoparticles.

Up to now, we have found *in vitro* digestive studies only on other nanoparticles (NPs) such as Ag and ZnO NPs exposed to the salivary fluid. A study conducted by Pokrowiecki et al. [24] showed that this type of nanoparticles, when placed in salivary fluid for over 24 hours, presented high destabilization due to the salivary composition. In our study the exposure to salivary fluid was for 2 minutes to avoid the long persistence of GNPS in the salivary fluid. In the study conducted by Pokrowiecki et al., when nanoparticles were introduced into the artificial saliva, they agglomerated rapidly, which is different from our study where this agglomeration of gold nanoparticles was not present [24].

To the best of our knowledge, the assessment of GNPs-CM in the gastrointestinal tract has not been previously studied. Although the behavior GNPs in gastric condition, or in intestinal fluid has been reported, the complexity of *in vitro* digestive transit simulation could provide valuable information regarding GNPs stability and behavior in oral administration applications [25].
The results of our study align with existing literature, showing a high total phenolic content in *Sambucus nigra* (ranging from 91.09 to 746.63 mg gallic acid/l) [26].

## CONCLUSION

Good stability of investigated GNPs along exposure to different simulated digestive fluids was observed on the analyzed nanoparticles. Along the transit, the gold nanoparticles have the tendency to additionally attach *Cornus mas* and *Sambucus nigra* functional moieties on their surface, increasing their diameter while proportionally reducing the free *Cornus mas* and *Sambucus nigra* molecule fraction in the solution. The significantly improved hydrodynamic diameter homogeneity of solution at the end of the experiment represents a consequence of this phenomena, providing the evidence for a good potential of the nanomaterial in human application with involving oral administration. Our study showed that *Sambucus nigra* contained more

abundant phenolic compounds than *Cornus mas*. This study has shown that elderberries can be an important source of antioxidant.

## EXPERIMENTAL SECTION

### *I. Synthesis of nanoparticles*

Due to their high content in antioxidant compounds, the fruits of *Cornus mas* L. and *Sambucus nigra* L. fruits are valuable sources of reducing agents of the gold ions and of capping agents of the obtained gold nanoparticles. The green synthesis of gold nanoparticles was achieved according to the protocol applied by Moldovan and co-workers [27]. Thus, the fruit extract was mixed under stirring with boiling 1 mM solution of tetrachloroauric acid in a 1:4 (vol/vol) ratio. After 15-30 minutes, the mixture's colour changed from red to purple, indicating the formation of colloidal gold. The *Cornus mas* fruit extract was prepared according to the method of Baldea et al. [28]. Obtaining the fruit extract of *Sambucus nigra* followed the same procedure, except for the amount of fruits used, which was twice as low as in the case of *Cornus mas* fruits.

### *II. Characterization of metallic nanoparticles*

The monitoring of the formation of gold nanoparticles was achieved by UV-Vis spectroscopy (using a Perkin Elmer Lambda 25 double beam spectrometer), while transmission electron microscopy (TEM), was used to investigate their shape and size (by a Hitachi Automatic H-7650 microscope operated at 120 kV).

### *III. In vitro digestion*

Gold nanoparticles obtained with *Cornus mas* (GNPs-CM] or with *Sambucus nigra* (GNPs-E) fruits extracts have been subjected to preliminary testing using *in vitro* digestive method, according to protocol developed by Minekus and co-workers [29].

Oral phase: Simulated salivary fluid (SSF) was prepared as to contain standard electrolyte and enzyme concentration ($K^+$:18.8 mmol/L, $Na^+$:13.6 mmol/L, $Cl^-$:19.5 mmol/L, $H_2PO_4^-$: 3.7 mmol/L, $HCO_3^-$, $CO_3^{2-}$: 13.7 mmol/L, $Mg^{2+}$: 0.15 mmol/L, $NH_4^+$: 0.12 mmol/L, $Ca2^+$: 1.5 mmol/L, amylase: 75 U/mL). The final pH of SSF was 7. According to the protocol, the nanomaterial was mixed with SFF using a 50:50 (vol/vol) ratio, for a period of 2 minutes incubation (37°C).

Gastric phase: Simulated gastric fluid (SGF) was prepared according to protocol. The electrolyte and enzymatic content of SGF included: $K^+$: 7.8 mmol/L, $Na^+$: 72.2 mmol/L, $Cl^-$: 70.2 mmol/L, $H_2PO_4^-$: 0.9 mmol/L, $HCO_3^-$, $CO_3^{2-}$: 25.5 mmol/L, $Mg^{2+}$: 0.1 mmol/L, $NH_4^+$: 1.0 mmol/L, $Ca^{2+}$: 0.15 mmol/L, pepsin: 2000 U/mL). The pH of final SGF solution was 3. The gastric phase included the collection of the mixture resulting from previous step and mixing it with SGF using a 50:50 (vol/vol) ratio. Incubation of 2 hours at 37°C was allowed.

Intestinal phase: Simulated intestinal fluid (SIF) was prepared. The solution presented a pH of 7 and included electrolytes such as: $K^+$: 7.6 mmol/L, $Na^+$: 123.4 mmol/L, Cl-: 55.5 mmol/L, $H_2PO_4^-$: 0.8 mmol/L, $HCO_3^-$, $CO_3^{2-}$: 85 mmol/L, $Mg^{2+}$: 0.33 mmol/L, $Ca^{2+}$: 0.6 mmol/L. Also, individual enzymes were added to the solution: trypsin: 100 U/mL, chymotrypsin: 25 U/mL, pancreatic lipase: 2000 U/mL, colipase (2:1 molar ratio with lipase), pancreatic amylase 200U/mL, bile (10mM). The intestinal phase included collection of aqueous mixture resulted from gastric phase and mixing it with SIF using 50:50 (vol/vol) ratio. Incubation of 2 hours at 37°C was allowed to the resulting mixture.

*III.1 Evaluation of fluids obtained after each phase of in vitro digestion.*

After each phase the samples were analyzed using macroscopical observation (color, sediment), spectral analysis (UV-Vis spectroscopy), and by assessing hydrodynamic diameter (DLS).

III.1.1*. Macroscopic observation*

Color changes and the presence of observable sediment at the bottom of containers were evaluated.

III.1.2. *UV-Vis spectroscopy*

UV-Vis spectra were recorded using a Shimadzu UV-1800® instrument. Samples were subjected to dilution (1:10 vol/vol) prior to the measurements. Normalization of spectra was performed using OriginLab software® 7.0.

III.1.3 *Dynamic Light Scattering*

The hydrodynamic diameter was measured using dynamic light scattering technique, using a Malvern Zetasizer NanoZS90 (Malvern, Instruments, Westborough, UK) equipment. Measurements were performed at a 90° diffraction angle, 25°C temperature, 0.2 refraction index, and 3.320 absorbance.

III.1.4. *Assessment of antioxidant capacity of fluids obtained after each phase of in vitro digestion.*

The measurement of hydrogen donor capacity is based on the reduction of the stable radical 1,1-diphenyl-picrylhydrazyl (DPPH) by a number of nonenzymatic antioxidants such as glutathione, tocopherol, ascorbic acid. This reduction can be tracked by changing color from purple to pale yellow, monitored by changes of samples absorbance at 520nm.

Samples are diluted with phosphate buffer 10 mM, pH 7,4. Then 0,5 ml of the solution 0.1mM of DPPH was added left for 30 min at room temperature and the absorbance against the blanks was read. Blanks consist of samples treated in the same way as samples, but in which absolute methanol has been added instead of DPPH solution. In parallel, the absorbance of some control samples that do not contain serum, but an appropriate volume of phosphate buffer is determined. Hydrogen donor capacity is expressed as Inhibition % in relation to the control samples according to the following calculation formula:
Inhibition% = [(Control absorbance – Serum sample absorbance) / Control absorbance] x 100 [30].

III.1.5. *Polyphenolic content assessment*

Folin-Ciocalteu method [31] was used to determine the total phenolic content. 3 mL Folin-Ciocalteu reagent was mixed with a sample of 0,5 mL of the diluted sample and permitted to react for 5 min in the dark, adding then 2,4 mL of 0.7 M $Na_2CO_3$ solution. The solution was incubated 2h in the dark at room temperature (22°C).

The absorbance of the mixture was measured with UV-Vis spectrophotometer Perkin Elmer Lambda 25 (Perkin Elmer, Shelton, CT USA) on a double beam against a blank sample. Using the gallic acid (GA) standard curve (0-100mg/mL), the total phenolic content of the extract is expressed as mg GA equivalents/mL. [32]

## ACKNOWLEDGMENTS

This project was supported by a PhD research project (PCD nr 2462/66/17.01.2020) offered by Iuliu Hatieganu University of Medicine and Pharmacy, Cluj-Napoca, Romania

## REFERENCES

1. Saha S, Xiong X, Chakraborty PK, Shameer K, Arvizo RR, Kudgus RA, Dwivedi SK, Hossen MN, Gillies EM, Robertson JD, Dudley JT, Urrutia RA, Postier RG, Bhattacharya R, Mukherjee P, *ACS Nano*, **2016**, *10*(12), 10636–10651.
2. V. H. Nguyen, B. J. Lee, *Int. J. Nanomedicine*, **2017**, *12*, 3137–3151.
3. Dalibera, NC, Oliveira AF, Azzoni AR, *Microfluid Nanofluid*, **2023,** 27, 56.
4. C. Li, D. Li, G. Wan, J. Xu, W. Hou, *Nanoscale Res. Lett*., **2011**, *6*, 1–10.
5. Alexis F, Pridgen E, Molnar LK, Farokhzad OC. *Mol. Pharm*. **2008**, *1*, 505–515.

6. Ielo I, Rando G, Giacobello F, Sfameni S, Castellano A, Galletta M, Drommi D, Rosace G, Plutino MR*, Molecules*. **2021**, *26*, 5823.
7. Kolanthai E, Fu Y, Kumar U, Babu B, Venkatesan AK, Liechty KW, Seal S. *Wiley Interdiscip Rev Nanomed Nanobiotechnol*.**2022**, *14*, e1741.
8. Chen H, Dorrigan A, Saad S, Hare DJ, Cortie MB, Valenzuela SM, *PLoS One*. **2013**, *8*, e58208.
9. Giljohann DA, Seferos DS, Daniel WL, Massich MD, Patel PC, Mirkin CA*. Angew. Chem. Int. Ed*. **2010**, *49*, 3280–94.
10. Dinda B, Kyriakopoulos AM, Dinda S, Zoumpourlis V, Thomaidis NS, Velegraki A, Markopoulos C, Dinda M. *J Ethnopharmacol*. **2016**, *193*, 70–90.
11. Moldovan B, David L. *Foods*, **2020**, *9(9)*, 1266.
12. Moldovan B, David L, *Mini-Rev. Org. Chem.* **2017**, 14, 489-495.
13. Jurca T, Baldea I, Filip GA, Olteanu D, Clichici S, Pallag A, Vicas L, Marian E, Micle O, Muresan M. *J. Physiol. Pharmaco*l. **2020**, 71.
14. Mikaili P, Koohirostamkolaei M, Babaeimarzangou SS, Aghajanshakeri S, Moloudizargari M, Gamchi NS, Toloomoghaddam S. *J. Pharm. Biomed. Sci*. **2013**, 35, 1732–8.
15. Bayram, HM, Arda Ozturkcan, S.; *J. Funct. Foods*, **2020**, *75*, 104252.
16. Uncini Manganelli RE, Zaccaro L, Tomei PE. *J. Ethnopharmacol*. **2005**, *98*,23–7.
17. Fazio A, Plastina P, Meijerink J, Witkamp RF, Gabriele B. *Food Chem*. **2013**, *140*, 817–24.
18. Lee J, Finn CE. *J. Sci. Food Agric*. **2007**, *87*, 2665–75.
19. Dawidowicz AL, Wianowska D, Baraniak B. *LWT - Food Sci.Technol*. **2006**, *39*, 308–15.
20. Arceusz A, Wesolowski M. *Open Chem*. **2015**,*13*, 1196–208.
21. Ferreira-Santos, P; Badim, H; Salvador, ÂC; Silvestre, AJD; Santos, SAO; Rocha, SM; Sousa, AM; Pereira, MO; Wilson, CP; Rocha, CMR, Teixeira JA, Botelho C. *Biomolecules*. **2021**, 11.
22. Matyas M, Hasmasanu MG, Zaharie G. *Medicina* **2019**, *55*, 720.
23. Liu H, Pierre-Pierre N, Huo Q. *Gold Bull*. **2012**, *45*, 187–95.
24. Pokrowiecki R, Wojnarowicz J, Zareba T, Koltsov I, Lojkowski W, Tyski S, Mielczarek A, Zawadzki P.; *Int. J. Nanomed*. **2019**, *14*, 9235-9257.
25. Sohal IS, Cho YK, O'Fallon KS, Gaines P, Demokritou P, Bello D. *ACS Nano*. **2018**, *12*, 8115–28.
26. Mikulic-Petkovsek M, Samoticha J, Eler K, Stampar F, Veberic R. *J. Agric. Food Chem*. **2015**, *63*, 1477–87.
27. Moldovan R, Mitrea DR, Florea A, Chiş IC, Suciu Ş, David L, Moldovan BE, Mureşan LE, Lenghel M, Ungur RA, Opris RV, Decea N, Clichici SV; *Antioxidants* (Basel). **2022**, *11*, 1343.
28. Baldea I, Florea A, Olteanu D, Clichici S, David L, Moldovan B, Cenariu M, Achim M, Suharoschi R, Danescu S, Vulcu A, Filip GA; *Nanomedicine* (*Lond*). **2020**, *15*, 55-75.

29. Minekus M, Alminger M, Alvito P, Ballance S, Bohn T, Bourlieu C, Carrière F, Boutrou R, Corredig M, Dupont D, Dufour C, Egger L, Golding M, Karakaya S, Kirkhus B, Le Feunteun S, Lesmes U, Macierzanka A, Mackie A, Marze S, McClements DJ, Ménard O, Recio I, Santos CN, Singh RP, Vegarud GE, Wickham MS, Weitschies W, Brodkorb A. *Food Funct*. **2014**, 5.
30. Janaszewska A, Bartosz G., *Scand. J. Clin. Lab. Invest*. **2002**, *62*, 231–6.
31. Singleton VL, Orthofer R, Lamuela-Raventós RM. *Methods Enzymol*. **1999**, *299*, 152–78.
32. Perde-Schrepler M, David L, Olenic L, Potara M, Fischer-Fodor E, Virag P, Imre-Lucaci F, Brie I, Florea A, *J. Nanomater.* **2016**, 6986370.

STUDIA UBB CHEMIA, LXIX, 2, 2024 (p. 97-108)
(RECOMMENDED CITATION)
DOI:10.24193/subbchem.2024.2.07

# ASSESSMENT OF THE AUTO-OXIDATION TENDENCY AND THE STORAGE EFFECTS ON THE QUALITY OF LIGNITE IN OLTENIA BASIN

**Oana-Raluca MATEI[a]*, Camelia TRAISTĂ[b], Eugen TRAISTĂ[a], Sorin RADU[a]**

**ABSTRACT.** Coal auto-oxidation is an undesirable chemical phenomenon that occurs due to the interaction of coal with atmospheric oxygen, a phenomenon that takes place during the coal life cycle, from the extraction moment until it is used. Thus, it is imperative to understand this process not only for the prevention of coal autoignition in the mining industry, but also for the optimization of the coal storage. The aim of this work was to assess the chemical behavior such as the oxidation, self-heating, and auto-ignition characteristics of coal in Oltenia Basin, Romania during its storage period. The hydrogen peroxide oxidation testing was used to determine the auto-oxidation tendency of lignite, while for the monitoring of coal quality during the storage process, coal samples were taken from a coal stack after 0, 5, 10, 20 and 30 days of storage and analyzed regarding the moisture (39,71%), ash content (35.21 – 37,11%), calorific value (1940 – 1875 kcal/kg), and volatile compounds (36.71 – 37,27%). A good correlation between the autoxidation and the content of volatile matter was observed. Compared to the initial values measured in initial coal samples (day 0), the carbon content and the superior calorific value decreased, while the ash content increased after a period of 30 days of storage.Thus, it can be concluded that knowing the self-ignition characteristic of lignites is important both for managing coal stocks and for evaluating the impact that coal storage can have on the environment.

***Keywords:*** *coal oxidation, lignite auto-oxidation, coal oxygen absorbtion, coal quality degradation, Oltenia basin*

[a] *Petroșani University, Mining Faculty, 20 Institutului str., RO-332006, Petroșani, Romania*
[b] *Petroșani University, Doctoral School, 20 Institutului str., RO-332006, Petroșani, Romania*
* *Corresponding author: raluca.matei989@yahoo.com*

## INTRODUCTION

Coal oxidation is an undesirable phenomenon occurs due to the interaction of coal with atmospheric oxygen [1,2]. From an economic point of view, the oxidation of coal causes significant losses of qualitative and quantitative nature, both in the production and in the consumption units, because of the degradation of the initial parameters existing in the deposit [3,4]. In addition, the oxidation of coal results in emissions of toxic gases, such as carbon monoxide [5]. The behavior of the oxidation process for diverse types of coal samples can be observed by simultaneous monitoring of several parameters: the loss of the content of $CO_2$, CO, and $H_2O$ [5]. It was reported that even after 20 years of oxidation, coal still produces carbon oxides. The release of $CO_2$ during these experiments was estimated to be 88% of the absorbed oxygen. In the same time, under normal conditions, the production of CO is between 1 and 4% of the absorbed oxygen [6].

Among the existing coals, lignite has several main characteristics that explain its auto-oxidation and auto-ignition tendency, such as: the high oxidation rate, high friability, and the presence of finely divided pyrites in the coal mass [7,8]. The alteration of coal properties results in: decrease of the calorific value, decrease of agglutination and coking capacities, decrease of the carbon and hydrogen content; increase of the amount of oxygen and ash content, etc. [9].

The occurrence of the phenomenon of oxidation and auto-ignition may have several causes. The large contact surface of the coal leads to a faster oxidation process, which explains why the coal in powder form or broken into small fragments auto-ignites more easily. Moreover, volatile components react with oxygen more easily, increasing the auto-ignition tendency of the respective coals [10]. The state of the coal surface influences the auto-ignition phenomenon, since oxygen absorption does not take place if the surface is occupied with water molecules in an absorbed state. This explains why, with coals that form humic acids in a humid environment, water can favor the auto-ignition phenomenon. The coals with a higher content of oxygen and a lower content of hydrogen have a greater tendency towards auto-ignition [9].

Previous works have shown that, following the oxidation reaction, the coal gains in weight by up to 12% of the initial weight [11]. This shows that the weight of oxygen remaining in the coal-oxygen complex is higher than the weight of the carbon and hydrogen eliminated in the gaseous products. It was reported that mineral bassanite ($CaSO_4 \times 1/2H_2O$), which comes from the calcite in coal, can be used as an oxidation indicator [12].

Humidity is one of the basic parameters in the oxidation process with major influence not only on the oxidation of pyrite, but also on the organic part of the coal. Water can play an important role in the oxidation of coal in which it induces the formation of (hydro)peroxides, initiating oxidative reactions in organic macerals. At a temperature of 150°C, oxidation is slower in humid air than in dry air [13].

The drying of coal can affect its reactivity to $O_2$ and can initiate other chemical changes. The most conclusive evidence on this subject was brought by Dack and collaborators [14], when examined the effects of the variations of the dry temperature (-15°C to 150°C) on the content of free radicals. It was shown that bulk drying at 100°C produces irreversible (albeit slight) chemical changes of the (acid-base) capacitor type, a phenomenon that occurs when the coal is heated. The results show that, even around the temperature of 100°C, thermal chemical reactions take place. Carbonyl species can be lost through thermal reactions even if they were formed through oxidation. It is considered that oxygen is added to the centers of free radicals, and the addition of $O_2$ is reversible [15]. The increase in temperature favors the formation of carboxyl groups.

The smallest particles of coal have a weak alkanes content higher than the larger particles that are collected from the base of the stack [16]. Macropore oxidation occurs when the determined rate of the oxidation stage of coal particles is made by the diffusion of oxygen through the core of the entire lump. In the coal oxidation in micropores, the oxidation of coal particles is 'open' and the oxidation is not limited to diffusion. The oxidation of the macropores depends on the granulation. The depth of oxygen penetration in the coal varies between 2 and 4.5 μm and in the hottest areas they could reach even 20-50 μm, if the smallest particles in the hottest areas are completely exposed to oxygenation [16]. These small particles can lose the carbonyl groups after all the active sites have reacted.

Coal oxidation is not a singular reaction but a group of sometimes competing reactions. Moreover, given the heterogeneity of the coal, differences between the data are usually reported [17]. Coal oxidation can occur through exposure to air after the coal is mined. It was found that the occurrence of an increased amount of phenolic-OH and carboxylic groups in the oxidized coal is likely a major factor reducing the hydrophobicity of the coal. The scheme of the coal oxidation process is presented in Figure 1 [18]. Reasons for the observed variation of coal hydrophobicity with rank undoubtedly reflect differences in the chemical composition of the coal, particularly the oxygen containing functional groups of the coal [19].

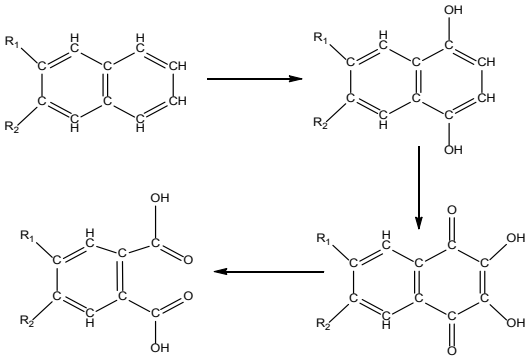

**Figure 1**. Scheme of the coal oxidation process

Coal autoignition is a serious problem in coal mining. Due to the very large loss of high-quality coal caused by spontaneous combustion, extensive research was conducted on the mechanism of spontaneous combustion of coal [20−24]. Many works have studied the activities of aliphatic chains and oxygen-containing functional groups, such as −OH, −CHO, −COOH, C=O, C– O, $-CH_3$ and $-CH_2$ in coal [25−27]. As a harmful element of coal, sulfur can not only produce $H_2S$ and $SO_2$, which would cause environmental pollution during the burning process, but also limit the rational use of coking coal resources. The sulfur-containing components of coal are mainly divided into two categories [28]: inorganic sulfur, which exists mainly in the form of mineral sulfur, such as pyrite; and organic sulfur, which generally exists in the molecular structure of coal through chemical bonds. According to the theory of molecular orbitals, sulfur atoms and other atoms could form π bonds by using the 3p orbitals. The valence electron shell is far from the atomic nucleus and is less bound to the atomic nucleus, so C–S bonds and S–H bonds are prone to breaking. Because of this, the sulfur atom oxidizes more easily than the carbon atoms [28].

The results of the research on the oxidation of different types of coal carried out by specialists in the field over the years have not been quite conclusive due to the multitude and the complexity of the factors and the investigations involved. Knowledge of the phenomena that favor the oxidation of coal requires a careful analysis of the variation of the physical and chemical properties of lignite, depending on the duration of storage and preservation. The aim of the current study is to assess the characteristics specific to each type of coal within the mining perimeters of Oltenia basin, Romania, from the point of view of oxidation, self-heating and auto-ignition capacity, with a view of preventing qualitative losses in time.

## RESULTS AND DISCUSSION

### *Self-heating and auto-ignition of lignite*

To ensure the prevention of quality losses over time, in the coal industry it is recommended to determine several quality parameters specific to each type of coal. Usually, these parameters refer to autooxidation, self-heating and auto-ignition capacity of coals.

In our study, the autoxidation tendency was assessed using coal granules with a grain size of 0.2 mm reacted with a perhydrol solution ($H_2O_2$ 20% - obtained by dilution of $H_2O_2$ 30% from Merck Millipore catalog number 107209) as oxidant, through the methodology described by Ionescu and collaborators [29]. The increase of the temperature of coal mixture following the perhydrol addition was registered. In identical working conditions (initial temperature, weight, granulation), the coals may have different behavior because of the different characteristics (petrographic, elemental composition, etc.).

The experiments were carried out on coal samples taken from two representative quarries in the mining basins of Oltenia, in order to find some notable similarities or differences between them, knowing in advance the specific geological characteristics of each mining area. The lignite samples for the experiment were taken from ten points (from holes dug 30 cm deep) on each coal stacks (finished production) belonging to the two quarries, which were then put together, to form two representative samples, according with the former Romanian standard SR ISO 1988:1996 and ISO 18283:2022 - Coal and coke - Manual sampling.

In the studied area the climate is temperate. The mild climate with moderate temperatures and abundant precipitation is also due to the circuit of southern, southwestern and western air masses. From the analysis of the monthly air temperature averages, it is found that the coldest month of the year is January (the average temperature being -2.5°C). The warmest month is July (average values between 20.6-21.4°C). During the year, the highest average monthly precipitation amounts are recorded at the end of spring (in May, between 86-103 l/m$^2$) and at the beginning of summer (in June, between 92-98 l/m$^2$) [31].

The Roşia and Pinoasa quarries belong to the Rovinari Mining Basin and the obtained results showed that the differences between them in terms of the heating-cooling time and the heating-cooling speed are insignificant, as presented in Figure 2.

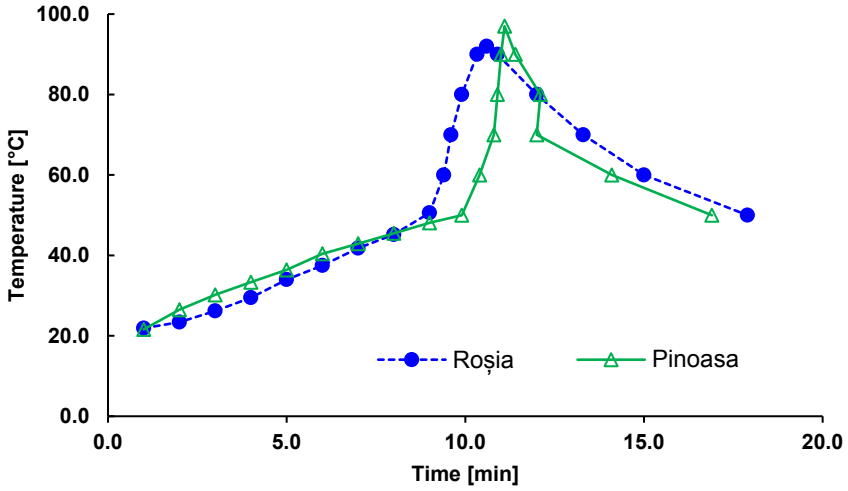


**Figure 2.** The variation of the heating-cooling temperature of the coal from the Rosia and Pinoasa in Rovinari basin

The results of the experiments regarding the auto-heating of the lignite from Rovinari (Roşia and Pinoasa quarries) are presented in Table 1.

**Table 1.** Auto heating parameters of the lignite from Roşia and Pinoasa quarries

| Coal source | $T_{in}$ [°C] | $T_{max}$ [°C] | Time [min] | Gradient [°C/min] |
|---|---|---|---|---|
| Roșia | 21.4 | 92.0 | 10.6 | 7.37 |
| Pinoasa | 21.4 | 97.0 | 11.1 | 6.85 |

According to the previously presented model, tests were carried out to determine the auto-oxidation capacity for coals from the Rosia quarry, for different values of the volatile matter content. The obtained experimental results are shown in table 2.

**Table 2.** Moisture, ash content, net colorific power, volatile mater content and results for the autooxidation tests on lignite from Roșia quarry

| Sample | Moisture W [%] | Ash content $A_{anh}$ [%] | Net caloric power $Q_{inf}$ [kcal/kg] | Volatile mater content V [%] | Autooxidation rate [°C/min] |
|---|---|---|---|---|---|
| 1 | 41.03 | 36.39 | 1838 | 39.70 | 7.4 |
| 2 | 37.64 | 35.41 | 2006 | 40.93 | 7.5 |
| 3 | 40.12 | 38.11 | 1812 | 39.40 | 7.3 |
| 4 | 42.69 | 39.43 | 1692 | 38.52 | 7.3 |
| 5 | 39.35 | 39.35 | 1817 | 37.79 | 7.2 |
| 6 | 42.53 | 38.76 | 1719 | 38.18 | 7.2 |
| 7 | 40.26 | 35.97 | 1897 | 40.11 | 7.4 |
| 8 | 42.00 | 38.81 | 1726 | 39.70 | 7.3 |
| 9 | 38.27 | 35.97 | 1977 | 40.10 | 7.3 |
| 10 | 40.48 | 38.44 | 1787 | 40.12 | 7.4 |
| 11 | 38.57 | 36.51 | 1932 | 42.15 | 7.6 |
| 12 | 38.62 | 37.72 | 1889 | 41.21 | 7.5 |
| Average | 40.13 | 37.57 | 1841 | 39.83 | 7.4 |
| Min | 37.64 | 35.41 | 1692 | 37.79 | 7.2 |
| Max | 42.69 | 39.43 | 2006 | 42.15 | 7.6 |
| Standard deviation | 1.70 | 1.44 | 101 | 1.26 | 0.12 |
| RSD% | 4.23 | 3.84 | 5.53 | 3.17 | 1.67 |

In the 12 analyzed lignite samples from Roșia quarry, the moisture content varied between 37.64 – 42.69 %. The ash content was in the range of 35.41 – 39.43 %, while the net calorific value ranged between 1692 – 2006 kcal/kg. In general, a very low variability of the measured parameters was observed, with a relative standard deviation (RDS %) below 5 %, which indicates a homogenous composition of the coal in the studied quarry. In the specific literature, there are extremely poor data on the autoxidation characteristics of lignite from Oltenia. Only Bacalu Ion [30] has carried out tests to determine this characteristic, obtaining values of the heating speed between 2.8 ÷ 7.1 °C/min.

The variation of the autoxidation rate of the lignite from the Roșia quarry, depending on the content of volatile substances, is shown in figure 3. From this figure, the autoxidation rate of coal samples increased with the increase in the volatile matter content; that is, the coal samples with a high volatile content exhibited a higher tendency to autoxidation. Thus, by measuring the volatile content of the coal, itsr autooxidation behavior may be predicted.

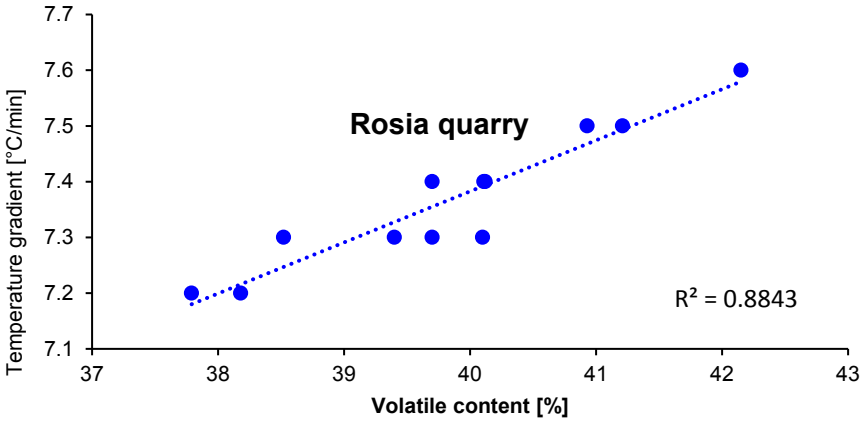


**Figure 3.** Variation of autooxidation rate *versus* volatile matter content in lignite Roșia quarry

According to Figure 3, it can be observed that there is a good correlation between the speed of autoxidation and the content of volatile matter.

***Modification of lignite characteristics depending on the storage time***

The analyses carried out regarding the auto-heating and the autooxidation capacity of the coals from the Oltenia Mining Basin revealed that the coal with the highest exposure to qualitative depreciation is the one from the Rovinari Quarries. This study is based on laboratory scale experiments through the analysis of the coal samples from Roșia and Pinoasa quarries.

It was found that, from a qualitative point of view, the coal from Pinoasa Quarry is superior to that from Roșia Quarry. This is highlighted by the results obtained based on chemical and technical analyses (Table 3), as well as by the way in which the parameters evolve under given experimental humidity conditions, in correlation with the period of storage in warehouses.

**Table 3.** The evolution of the quality parameters of lignite according to the storage duration (The Roșia Quarry)

| Period [days] | $W_{tot}$ [%] | $A_{anh}$ [%] | $Q_{inf}$ [kcal/kg] | $Q_{sup}$ [kcal/kg] | $C_{tot}$ [%] | $V_{anh}$ [%] |
|---|---|---|---|---|---|---|
| 0 | 39.71 | 35.21 | 1940 | 3580 | 57.03 | 36.61 |
| 5 | 39.71 | 36.48 | 1896 | 3507 | 55.69 | 36.94 |
| 10 | 39.71 | 36.75 | 1887 | 3492 | 55.39 | 37.09 |
| 20 | 39.71 | 36.90 | 1882 | 3483 | 55.21 | 37.24 |
| 30 | 39.71 | 37.11 | 1875 | 3471 | 54.99 | 37.27 |

Compared to the initial values of the analyses ($V_{anh}$=36.61, $C_{tot}$=57.03, $W_{tot}$=39.71%, $A_{anh}$=35.21 şi $Q_{sup}$=3580 Kcal/Kg), under the conditions of a storage period of 30 days, it can be observed that the content of volatile substances ($V_{anh}$) increased by 1.8 %, while the carbon content ($C_{tot}$) decreased by 3.6 %. The ash content ($A_{anh}$) increased by 5.4 %, though the superior calorific value ($Q_{sup}$) decreased by 3.1 % when compared to the initial value. The loss of coal estimated after 30 days of storage is 5,1% from initial mass, that which is mainly found in the reduction of carbon content.

Taking into account that 4.3 % of the oxidized carbon forms carbon monoxide, it follows that, by storing lignite for 30 days, there is an emission of 5.2 kg CO/ton of coal/month. Reported to the amounts of tens of thousands of tons of stored coal, it follows that the emissions of this toxic gas are significant for the storage area.

## CONCLUSIONS

According to the experimental results, the coal storage time depends on two main factors: the production deposited in the stacks and the amount of coal delivered daily. The phenomenon is characterized by a continuous movement of the coal stock in the warehouses. The more deliveries increase, the shorter the downtime, and the quality parameters of the excavated coal keep their initial values. In the case of keeping the coal in the warehouse for an average duration of 30 days, the quality of the coal decreases by more than 3 %.

The time the coal stays in the warehouses is different from one day to another and from one month to another, varying from a minimum duration of a few days to approx. 50 days of storage. The initiation of the oxidation process

and, implicitly, the qualitative deterioration of the coal, takes place around the value of 1900 Kcal/Kg (corresponding to the quality determined during testing), and decreases proportionally with the increase in storage time, reaching a quality loss of approx. 2.6 % after an average storage period of 10 - 15 days. The essential element in the analysis of coal depreciation is the duration of the storage process. The auto-oxidation phenomenon also has an impact on the quality of the environment, mainly the air, through carbon monoxide emissions, which can reach values of 5.2 kg CO/ton of coal/month.

## EXPERIMENTAL SECTION

### *Evaluations of auto-oxidation tendency.*

The hydrogen peroxide oxidation method was used to determine the auto-oxidation tendency of lignite. Already in 1952 Orleanskaya described the use of oxygenated water for evaluating the self-ignition capacity of coals, but by a different procedure [32]. The method was developed by the University of Petroșani in the 70's, and has been widely used to identify coals that are at risk of spontaneous combustion [29]. At that time, it was considered so important that it was also included in the chemistry laboratory curriculum. This method consists of placing 3 g of coal sample in 20 ml of 20% $H_2O_2$ in a glass container and monitoring the temperature over time. The maximum temperature obtained and the time in which it is reached are measured.

### *Monitoring of coal quality evolution during storage*

Coal samples were taken from a coal stack initially, and after 5, 10, 20 and 30 days. The samples were processed to determine certain technical characteristics in accordance with the standards in force as follows: SR ISO 1988:1996 [33] (The standard refers to coal sampling methods, as well as obtaining and preparing samples for analysis and moisture), SR 5264:1995 [34] (The standard establishes the methods for determining the humidity of solid mineral fuels by drying at 105°C), SR ISO 1171 [35] (The standard establishes a method for the determination of ash for all solid mineral fuels, using the gravimetric method, by calcination at 825°C), ISO 1928-2020 [36] (This document specifies a method for the determination of the gross calorific value of a solid mineral fuel at constant volume and at the reference temperature of 25 °C in a combustion vessel calorimeter calibrated by combustion of certified benzoic acid.) and STAS 5268 [37].( The determination consists of heating the sample, in the absence of air, at 850°C for 7 minutes and calculating the mass loss)

## REFERENCES


1. Z. Yutao, Z. Yuanbo, L. Yaqing, S. Xueqiang, Z. Yujieș; *Energy*, **2021**, *234*, 121299
2. M. Yu, N. Yang, H. Li, . Wang, M. Wu, F. Wang, T. Chu, K. Wang; *Energy*, **2024**, *289*, 129974
3. H. Liu, Z. Li, Y. Yang, G. Miao, P. Li, G. Wang, Y. Zhang, Z. Hou; *Energy*, **2024**, *291*, 130336
4. F. Wang, B. Tan, X. Zan, J. Huang, X. Fang, S. Fu, H. Wang, T. Li, Q. Qi; *Energy*, **2024**, *290*, 130054
5. H. Liu, Z. Li, Y. Yang, G. Miao; *J. Clean. Prod*., **2023**, *420*, 138380
6. F. E. Huggins, G.R. Dunmyre, M.C. Lin, G.P. Huffman; *Fuel*, **1985**, *64*, 348-350
7. M. Onifade, B. Genc; *Int. J. Coal. Sci. Technol*., **2019**, *6*, 151–168
8. B.B. Beamish, A. Arisoy; *Fuel*, **2008**, *87*, 125–130
9. S. Aich, B.K. Nandi, S. Bhattacharya; *Int. J. Coal. Sci. Technol*., **2019**, *6*, 51–62.
10. Y. Zhang, J. Zhang, Y. Li, S. Gao, C. Yang, X. Shi; *ACS Omega*, **2021**, *6*, 7669-7679
11. D. Zhou, W. Lu, J. Li, Y. Song, C. Wu, *Fuel*, **2022**, *308*, 121802
12. I. Mohammed, A. Isah, D. Al Shehri, M. Mahmoud, M. Arif, M.S. Kamal, I.S. Alade, S. Patil; *ACS Omega*, **2022**, *7*, 28571-28587
13. R. Bouwman, I.L.C. Freriks; *Fuel*, **1980**, *59*, 315-322
14. S.W. Dack, M.D. Hobday, T.D. Smith, J.R. Pilbrow; *Fuel*, **1984**, *63*, 39-42
15. J.S. Gethner; *Fuel*, **1987**, *66*, 1091-1096
16. M.G. Rockley, J.P. Devlin; *Applied Spectroscoy*, **1980**, *34*, 407-408
17. J. Barraza, A. Portilla, J. Pineres; *Fuel Process. Technol*., **2011**, *92*, 776-779
18. J. Yu, Y. Jiang, A. Tahmasebi, Y. Han, X. Li, J. Lucas, T. Wall; *Chem. Eng. Technol*., **2014**, *37*, 1635-1644
19. W. Wang, L. Liang, Y. Peng, M.; *Minerals,* **2021**, *11*, 239
20. J. Deng, Y. Xiao, Q. Li, J. Lu, H. Wen; *Fuel*, **2015**, *157*, 261– 269
21. Hu, X.; Yang, S.; Zhou, X.; Yu, Z.; Hu, C. J. Nat. Gas Sci. Eng. 2015, 26, 461–469
22. C. Avila, T. Wu, E. Lester; *Energ. Fuel*. **2014**, *28*, 1765– 1773
23. M. Onifade, B. Genc; *Int. J. Min. Sci. Technol*. **2018**, *28*, 933– 940
24. Y. Liang, F. Tian, H. Luo, H. Tang, *Int. J. Min. Sci. Technol*. **2015**, *25*, 749– 754
25. G.Gürdal, H. Hoşgörmez, D. Özcan, X. Li, H. Liu, W. Song; *Int. J. Coal Geol*., **2015**, *138*, 1– 15
26. K. Li, R. Khanna, J. Zhang, M. Barati, Z. Liu, T. Xu, V. Yang, V. Sahajwalla; *Energ. Fuel*., **2015**, *29*, 7178– 7189
27. X. Qi, L. Chen, H. Xin, Y. Ji, C. Bai, R. Song, H. Xue, F. Liu; *Energ. Fuel*., **2018**, 32, 10469– 10477
28. W. H. Calkins; *Fuel*, **1994**, *73*, 475– 484
29. C. Ionescu, A. Matei, E. Traistă, - Lucrări practice - Chimie Generală – Universitatea Tehnică Petroşani, **1993** – In Romanian

30. I. Bacalu, Studiul dependenţei parametrilor calitativi ai lignitului de condiţiile de exploatare și depozitare a acestuia, PhD Thesis, Petroșani University, **2009**, 188 – 198
31. Raport la studiul de evaluare a impactului asupra mediului pentru continuarea lucrărilor în perimetrul de licenţă extins al obiectivului de investitii "Deschiderea si punerea în exploatare a carierei Rosia de Jiu, judetul Gorj, la o capacitate de 8,0 milioane tone/an lignit", ICSITPML S.A. Craiova, **2020**, 274 – 282
32. G. R. Yohe, Oxidation of coal, Illinois State Geological Survey Report of Investigations 207Urbana, Illinois 1958, 33
33. SR ISO 1988:1996 Coals. Sampling
34. SR 5264:1995 Solid mineral fuels. Moisture determination
35. ISO 1171:2003 Solid mineral fuels – Determination of ash
36. ISO 1928:2020 Coal and coke. Determination of gross calorific value
37. STAS 5268-90 Combustibili solizi. Determinarea materiilor volatile, a cocsului şi a cărbunelui fix – in Romanian

STUDIA UBB CHEMIA, LXIX, 2, 2024 (p. 109-120)
(RECOMMENDED CITATION)
DOI:10.24193/subbchem.2024.2.08

# RADIOCARBON INVESTIGATION OF THE SOLITARY AFRICAN BAOBAB FROM DALKUT, DHOFAR, OMAN

**Adrian PATRUT[a,b]*, Roxana T. PATRUT[a], Mihaly MOLNAR[c], Laila S. AL HARTHY[d], J. Jed BROWN[e], Laszlo RAKOSY[f], Khalid A. AL FARSI[d], Abdulrahman R. AL HINAI[d], Ileana Andreea RATIU[a,b], Jenő BODIS[a,b]**

**ABSTRACT.** The article discloses the AMS (accelerator mass spectrometry) radiocarbon dating results of the well-known African baobab of Dalkut, Dhofar Governorate, Oman. The investigation shows that the baobab has a cluster structure and is composed of 3 perfectly fused stems. Three wood samples were collected from primary branches and one sample was collected from the exterior of a stem. Eight tiny segments were extracted from the samples and dated by radiocarbon. The oldest dated sample segment, which originates from a primary branch of the southern stem, had a radiocarbon date of 590 ± 18 BP, which corresponds to a calibrated age of 685 ± 15 years. This result indicates that the southern stem of the baobab of Dalkut is 800 ± 30 years old. According to other radiocarbon dating results, the two northern stems are younger and emerged from the southern stem around 550 years ago. The tree of Dalkut is a solitary baobab. The nearest baobab is over 150 km away, to the north.

***Keywords:*** *AMS radiocarbon dating, Adansonia digitata, Oman, multiple stems, age determination.*

[a] *Babeş-Bolyai University, Faculty of Chemistry and Chemical Engineering, 11 Arany Janos, RO-400028, Cluj-Napoca, Romania.*
[b] *Babeş-Bolyai University, Raluca Ripan Institute for Research in Chemistry, 30 Fantanele, RO-400294 Cluj-Napoca, Romania.*
[c] *Interact Centre, Institute for Nuclear Research, Bem ter 18/C, 4001 Debrecen, Hungary.*
[d] *Oman Botanic Garden, Muscat, Oman*.
[e] *Qatar University, College of Arts and Sciences, P.O. Box 2713, Doha, Qatar.*
[f] *Babeş-Bolyai University, Faculty of Biology and Geology, 44 Republicii, RO-400015 Cluj-Napoca, Romania.*
* *Corresponding author, apatrut@gmail.com*

## INTRODUCTION

The *Adansonia* genus, a subdivision of the Bombacoideae subfamily of Malvaceae, consists of eight generally recognised species. One species originates from mainland Africa, six species are endemic to Madagascar, while one species grows only in northern Australia. The African baobab (*Adansonia digitata* L.) is the best-known and most widespread of these species. Although it is endemic to the arid savanna of mainland Africa between the latitudes 16º N and 26º S, the African baobab can also be found on several African islands and outside Africa, in different areas throughout the tropics, where it has been introduced [1-5].

In 2005, we started a comprehensive research project aimed to clarify several controversial and poorly understood aspects related to the architecture, growth, and age of the African baobab. Our research relies on AMS radiocarbon dating of very small wood samples extracted especially from inner cavities, deep incisions in the stems, fractured stems or from the exterior of large baobabs. This methodology allows to investigate and date not only demised or fallen specimens, but also live and standing individuals [6-19].

According to our research, all superlative, i.e., large and/or old baobabs, are multi-stemmed and exhibit preferentially closed or open ring-shaped structures. The largest and oldest individuals may have wood volumes up to 300-500 $m^3$ and may reach ages up to 2,500 years [8, 9].

Since 2013 we extended our research on superlative individuals of the three best-known species of Madagascar, namely the fony (*Adansonia rubrostipa* Jum. & H. Perrier), the za (*Adansonia za* Baill.) and the Grandidier baobab (*Adansonia grandidieri* Baill.) [20-27].

The Sultanate of Oman has an interesting and unexpected African baobab population. With one exception, all specimens are located in southern Oman, in the Dhofar Governorate (region). Certain researchers consider these baobabs a botanical reminder of Dhofar's links with Africa.

The largest number of trees can be found in the wilayat (province) of Mirbat, in the so-called Baobab Forest of Wadi Hinna. Wadi Hinna is a small semi-arid valley (3 $km^2$) at the edge of the Dhofar Mountains (17º03' N, 54º36' E, altitude 300-360 m) and at 20 km from the coastal plain. The precipitation (annual rainfall 130 mm) falls almost exclusively during the rainy season (mid-June to mid-September), in which moist air from the Indian Ocean, i.e., the southwest monsoon (called khareef), encounters the mountains leading to clouds and dense fog [28]. The 106 trees of the Baobab Forest grow on a slope among huge stones of sedimentary rocks. In recent years, Wadi Hinna was divided into two parts, located at lower and higher

altitudes, namely Wadi Hinna (with 73 baobabs) and Wadi Hasheer (with 33 baobabs), according to the stratigraphic origin and composition. Other 3 baobabs can be found lower than Wadi Hinna, just above the Salalah Plain (altitude 90 m), in Wadi Al Ghazir.

A well-known baobab grows completely isolated in the town and wilayat of Dalkut, close to the border with Yemen.

Finally, there is a single baobab in the extreme north, close to Al Zahaimi, in the wilayat of Sohar in the Al Batinah North Governorate.

Here we present the investigation and AMS radiocarbon dating results of the baobab of Dalkut.

## RESULTS AND DISCUSSION

*The baobab of Dalkut*. As mentioned, Dalkut (also written Dhalkut, Dalqut, Dhalqut or Dhalkout) is a fishing town and also a wilayat in the Dhofar Governorate of Oman. The town of Dalkut is located below the Al Qamar Mountains and can be reached by descending the highway towards Dalkut Beach. Dalkut is positioned on the western side of Salalah, the capital of Dhofar, at 154 km (via the hairpin bend road) and 102 km (flight distance). The border with Yemen is at only 15 km (flight distance) toward west.

The annual rainfall in Dalkut is only 110 mm. The rain falls especially during the khareef season, when there is lot of fog and low visibility.

A main tourist attraction in Dalkut is the solitary baobab called by the locals “Hiroum Dheeri” (in Arabic, “The Tree from Very Far Away”), hinting at its allochthonous nature. The nearest baobab is in Wadi Hinna, over 150 km away.

The GPS coordinates of the baobab of Dalkut are 16º42.498’ N, 053º15.588’ E and the altitude is 67 m. It has a maximum height (h) of 13.5 m, the circumference at breast height (cbh; at 1.30 m above ground level) is 13.43 m and the total wood volume (V) is 60 $m^3$. Its height decreased to only 7.4 m after the tallest branch broke during the period of 2018-2019. The baobab is composed of 3 perfectly fused stems and has a cluster structure. The tri-stemmed trunk consists of two parts: the northern part has two stems, while the southern part is single-stemmed (**Figures 1 and 2**).

**Figure 1.** General view of the baobab of Dalkut taken from the east in 2022.

**Figure 2.** View of the baobab of Dalkut taken in 2017 before its tallest branch broke.

The wide canopy, with the horizontal dimensions of 24.20 (NS) x 29.50 (WE) m, has five primary branches with diameters up to 1.2 m.

We consider it highly possible that the current ground level around the baobab is 0.50 m higher than the initial ground level, due to the cement annexes/elements erected around the tree. In this case, the circumference cbh becomes 14.02 m and all height values increase by 0.50 m.

*Wood samples.* Four wood samples were collected from the 3 stems using an increment borer. Each sample has a code composed of a digit indicating the trunk it came from (1, 2, or 3) and a capital letter indicating whether it was collected directly from the stem or from a primary branch (S or B). Several tiny segments, each $10^{-3}$ m long, extracted from determined positions of the collected samples. The closest and youngest segment from each sample was noted by x, while the deepest and oldest segment was noted by y. An intermediate segment was noticed by i.

*AMS results and calibrated ages*. Radiocarbon dates of the eight sample segments are presented in Table 1. The radiocarbon dates are expressed in $^{14}C$ yr BP (radiocarbon years before present, i.e., before the reference year 1950). Radiocarbon dates and errors were rounded to the nearest year.

Calibrated (cal) ages, expressed in calendar years CE (CE, i.e., common era), are also listed in Table 1. The 1σ probability distribution (68.3%) was selected to derive calibrated age ranges. For two sample segments (1By, 3Sx), the 1σ distribution is consistent with one range of calendar years. For one segment (3By), the 1σ distribution corresponds to two ranges of calendar years, for one segment (2By) it is consistent with three ranges, while for another segment (3Bi) it corresponds to four ranges. In these cases, the confidence interval of one range is considerably greater than that of the other(s); therefore, it was selected as the cal CE range of the segment for the purpose of this discussion. For obtaining single calendar age values of sample segments, we derived a mean calendar age of each sample segment, called assigned year, from the selected range (marked in bold). Sample/ segment ages represent the difference between the current year 2024 CE and the assigned year, with the corresponding error. Sample ages and errors were rounded to the nearest 5 yr.

We used this approach for selecting calibrated age ranges and single values for sample ages in all our previous articles on AMS radiocarbon dating of large and old angiosperm trees [6-27].

**Table 1.** AMS Radiocarbon dating results and calibrated ages of samples collected from the baobab of Dalkut.

| Sample/ segment code | Depth[1] [height[2]] (m) | Radiocarbon date [error] ($^{14}$C yr BP) | Cal CE range 1σ [confidence interval] | Assigned year [error] (cal CE) | Sample age [error] (cal CE) |
|---|---|---|---|---|---|
| Dk-1Bx | 0.01 [2.50] | - | - | - | >Modern |
| Dk-1By | 0.34 [2.50] | 259 [± 10] | **1643-1655 [68.3%]** | 1649 [± 6] | 375 [± 5] |
| Dk-2Bx | 0.01 [2.65] | - | **-** | - | >Modern |
| Dk-2By | 0.60 [2.65] | 206 [± 18] | 1658-1683 [22.3%] 1743-1750 [5.3%] **1765-1799 [40.7%]** | 1772 [± 17] | 250 [± 15] |
| Dk-3Bx | 0.01 [3.09] | - | **-** | - | >Modern |
| Dk-3Bi | 0.15 [3.09] | 193 [± 10] | 1665-1676 [19.1%] 1743-1751 [11.2%] **1765-1784 [33.1%]** 1794-1797 [4.9%] | 1774 [± 9] | 250 [± 10] |
| Dk-3By | 0.35 [3.09] | 590 [± 18] | **1324-1355 [60.2%]** 1387-1405 [8.1%] | 1649 [± 15] | 685 [± 15 ] |
| Dk-3Sx | 0.01 [1.40] | 11 [± 10] | **1897-1903 [68.3%]** | 1900 [± 3] | 125 [± 5] |

[1] Depth in the wood from the sampling point.
[2] Height above ground level.

*Dating results of sample segments.* The baobab of Dalkut does not have fractured stems, deep entrances in the trunk, open false or normal cavities, nor an open or closed ring-shaped structure, to allow for the collection of very old samples, close to the age of the tree.

In such cases, we consider it is possible to investigate and date primary branches which are comparable in age to that of the stem from which they emerged. Thus, 3 samples, noted with the capital letter B, were extracted from 3 primary branches where each originates from one of the 3 stems.

The oldest sample segment was extracted from a primary branch which originates from the southern stem 3. Sample Dk-3B was collected at the height of 3.09 m above the ground and had a length of 0.35 m (**Figure 3**). The deepest segment Dk-3By, which represents the sample end, has a radiocarbon date of 590 ± 18 BP, which corresponds to a calibrated age of 685 ± 15 yr. At sampling height, the diameter of the primary branch (in sampling direction) is 0.95 m. The age of the oldest part of this primary

branch can be calculated by extrapolating the position and age of the oldest sample segment, Dk-3By, to the theoretical point of maximum age of the branch; this corresponds to its center at sampling height, which is positioned at 0.475 m from the sampling point. Based on our previous research on growth rates of baobabs, we consider that this branch and also its corresponding stem 3 are 800 ± 30 yr old.

The intermediary segment Dk-3Bi, which originates from a distance of 0.15 m from the sampling point, has a radiocarbon date of 193 ± 10 BP, which corresponds to a calibrated age of 250 ± 10 yr.

The sample Dk-1B was extracted from a primary branch of the northern stem 1. It was collected at the height of 2.50 m above the ground and had a length of 0.34 m. The deepest and oldest segment Dk-1By, which represents the sample end, has a radiocarbon date of 259 ± 10 BP, which corresponds to a calibrated age of 375 ± 5 yr. At sampling height, the diameter of this primary branch (in sampling direction) is 1.04 m. Thus, the theoretical center of the branch at sampling height is located at 0.52 m from the sampling point. These results indicate that the branch and its corresponding stem 1 are 550 ± 30 yr old.

The sample Dk-2B originates from a primary branch of the northern stem 2. It was collected at the height of 2.65 m above the ground and had a length of 0.24 m. The deepest and oldest segment Dk-2By, which represents the sample end, has a radiocarbon date of 206 ± 18 BP, which translates to a calibrated age of 250 ± 15 yr. At sampling height, the diameter of this primary branch (in sampling direction) is 1.02 m. Consequently, the theoretical center of the branch at sampling height is located at 0.51 m from the sampling point. The results indicate that the branch and its corresponding stem 2 are also 550 ± 30 yr old.

For the nearest segments of the 3 samples (adjacent to the bark), namely Dk-1Bx, Dk-2Bx and Dk-3Bx, the age falls after the year 1950 CE, i.e. the $^{14}C$ activity, expressed by the ratio $^{14}C/^{12}C$, is greater than the standard activity in the reference year 1950. Such values, which correspond to negative radiocarbon dates, are termed greater than Modern (>Modern). In such cases, the dated wood is young, being formed after 1950 CE. These results show that there are no arguments to claim that the 3 dated primary branches would have stopped their growth.

Eventually, we extracted one sample directly from the largest stem 3. The sample Dk-3S was collected at the height of 1.40 m and had a length of only 0.16 m. The sample was too short to provide interesting information about the age of this stem. That is why we dated only the nearest segment Dk-3Sx. It has a radiocarbon date of 11 ± 10 BP, which corresponds to a calibrated age of 125 ± 5 yr. According to this result, the largest stem 3 stopped growing 125 years ago.

**Figure 3.** Collecting the oldest sample Dk-3B.

*Age of the baobab of Dalkut*. The dating result of segment Dk-3By indicates that the maximum age of the southern part of the baobab of Dalkut, that consists only of stem 3, is 800 ± 30 calendar yr, i.e., 770 – 830 yr. The results of segments Dk-1By and Dk-2By show that stems 1 and 2, which form the northern part of the baobab are both 550 ± 30 calendar yr, i.e., 520 – 580 yr old. It can be stated that the baobab of Dalkut started growing around the year 1225 CE.

## CONCLUSIONS

The research presents the AMS radiocarbon dating results of the baobab of Dalkut from the Dhofar Governorate, Oman. Even if it is neither the biggest nor the oldest baobab in Oman, the baobab of Dalkut is likely the best known. It exhibits a cluster structure and is composed of 3 fused stems. Three wood samples were collected from primary branches, while one

sample was extracted from the outer part of a stem. The oldest dated sample has a radiocarbon date of 590 ± 18 BP, corresponding to a calibrated age of 685 ± 15 years. This value indicates that the single-stemmed southern part of the baobab is 800 ± 30 years old. On the other hand, the results show that the double-stemmed northern part of the baobab is younger and emerged from the southern stem 550 ± 30 years ago. In addition, the results indicate that the southern stem stopped growing 125 years ago, while the two northern stems, as well as all primary branches, continue to grow.

The baobab of Dalkut is a solitary African baobab. The nearest baobab is over 150 km to the north in Wadi Hinna. We consider that the baobab of Dalkut was planted by an African traveler passing through the area 800 years ago, around the year 1225. This classifies the baobabs of the Arabian Peninsula as archaeophytes.

The current condition of the baobab is not good. Many branches are partially or totally broken. We also observed that this tree was periodically infested with mealybugs (Pseudococcidae), which may be negatively affecting its growth. The bark is heavily damaged and missing in some parts. Therefore, we speculate that the baobab of Dalkut could be close to the end of its life cycle.

## EXPERIMENTAL SECTION

*Sample collection.* The investigated wood samples were collected with a Haglöf CH 800 increment borer (0.80 m long, 0.0108 m inner diametre). After each coring, the increment borer was cleaned and disinfected with methyl alcohol. The small coring holes were sealed with Steriseal (Efekto), a special polymer sealing product which prevents any infection of the trees. Several tiny segments of the length of $10^{-3}$ m were extracted from the collected samples. The segments were processed and investigated by AMS radiocarbon dating.

*Sample preparation*. The α-cellulose pretreatment method was used for removing soluble and mobile organic components. The resulting samples were combusted to $CO_2$ with $MnO_2$ as oxidant in a modified sealed combustion tube. The gaseous $CO_2$ was analyzed by $^{14}C$ AMS [29-31].

*AMS measurements*. The AMS radiocarbon measurements were performed at the Ede Hertelendi Laboratory of Environmental Studies (HEKAL), Debrecen, Hungary, by an EnvironMICADAS, which is a coupled AMS mini carbon dating system (200 kV power system) with enhanced gas

ion source (GIS). The GIS allows measurements directly from gaseous $CO_2$. The EnvironMICADAS was developed and built by ETH Laboratory, Zürich, Switzerland, especially for Environmental studies [30,32].

The obtained fraction modern values were finally converted to a conventional radiocarbon date. The radiocarbon date values are corrected with the value -25‰ for $\delta^{13}C$ isotopic fractionation. The radiocarbon dates and errors were rounded to the nearest year.

*Calibration*. Radiocarbon dates were calibrated and converted into calendar ages with the OxCal v4.4 for Windows [33], by using the IntCal20 atmospheric data set [34].

## ACKNOWLEDGMENTS

The investigation of the baobabs of Dhofar, Oman was authorised by the Environment Authority of the Sultanate of Oman with the Permit Number 6210/10/173.

The research was funded by the Romanian Ministries of Education and of Research CNCS-UEFISCDI under grant PN-III-P4-ID-PCE-2020-2567, No.145/2021.

## REFERENCES

1. D.A. Baum, *Annals of the Missouri Botanical Garden*, **1995**, *82*, 440-471.
2. G.E. Wickens, P. Lowe, "The Baobabs: Pachycauls of Africa, Madagascar and Australia", Springer, Dordrecht, **2008**, pp. 232-234, 256-257, 295-296.
3. J.D. Pettigrew, L.K. Bell, A. Bhagwandin, E. Grinan, N. Jillani, J. Meyer, E. Wabuyele, C.E. Vickers, *Taxon*, **2013**, *61*,1240-1250.
4. A. Petignat, L. Jasper, "Baobabs of the world: The upside down trees of Madagascar, Africa and Australia", Struik Nature, Cape Town, **2015**, pp. 16-86.
5. G.V. Cron, N. Karimi, K.L. Glennon, C.A. Udeh, E.T.F. Witkowski, S.M. Venter, A.E. Assobadjo, D.H. Mayne, D.A. Baum, *Taxon*, **2016**, *65*, 1037-1049.
6. A. Patrut, K.F. von Reden, D.A. Lowy, A.H. Alberts, J.W. Pohlman, R. Wittmann, D. Gerlach, L. Xu, C.S. Mitchell, *Tree Physiology*, **2007**, *27*, 1569-1574.
7. A. Patrut, K.F. von Reden, R. Van Pelt, D.H. Mayne, D.A. Lowy, D. Margineanu, *Annals of Forest Science*, **2011**, *68*, 93-103.
8. A. Patrut, S. Woodborne, R.T. Patrut, L. Rakosy, D.A. Lowy, G. Hall, K.F. von Reden, *Nature Plants*, **2018**, *4(7),* 423-426.

9. A. Patrut, K.F. von Reden, D.H. Mayne, D.A. Lowy, R.T. Patrut, *Nuclear Instruments and Methods in Physics Research Section B*, **2013**, *294*, 622-626.
10. A. Patrut, S. Woodborne, K.F. von Reden, G. Hall, M. Hofmeyr, D.A. Lowy, R.T. Patrut, *PLOS One*, **2015**, *10(1)*, e0117193.
11. A. Patrut, L. Rakosy, R.T. Patrut, I.A. Ratiu, E. Forizs, D.A. Lowy, D. Margineanu, K.F. von Reden, *Studia UBB Chemia*, **2016**, *LXI*, *4*, 7-20.
12. A. Patrut, R.T. Patrut, L. Rakosy, D.A. Lowy, D. Margineanu, K.F. von Reden, *Studia UBB Chemia*, **2019**, *LXIV*, *2 (II)*, 411-419.
13. A. Patrut, S. Woodborne, K. F. von Reden, G. Hall, R.T. Patrut, L. Rakosy, P. Danthu, J-M. Leong Pock-Tsy, D.A. Lowy, D. Margineanu, *Radiocarbon*, **2017**, *59(2)*, 435-448.
14. A. Patrut, S. Woodborne, R.T. Patrut, G. Hall, L. Rakosy, C. Winterbach, K.F. von Reden, *Forests*, **2019**, *10*, 983-994.
15. A. Patrut, R.T. Patrut, M.J. Slater, L. Rakosy, D.A. Lowy, K.F. von Reden, *Studia UBB Chemia*, **2020**, *LXV*, *3*, 149-156.
16. A. Patrut, A. Garg, S. Woodborne, R.T. Patrut, L. Rakosy, I.A. Ratiu, D.A. Lowy, *PLoS ONE*, **2020**, *15(1)*, e0227352.
17. A. Patrut, R.T. Patrut, L. Rakosy, I.A. Ratiu, D.A. Lowy, K.F. von Reden, *Dendrochronologia* **2021**, *70*, 125898.
18. A. Patrut, R.T. Patrut, W. Oliver, I.A. Ratiu, D.A. Lowy, G. Shiimbi, L. Rakosy, D. Rakosy, S. Woodborne; K.F. von Reden, *Forests*, **2022**, *13*, 1899.
19. R.T. Patrut, A. Patrut, G. Hall, C.W. Winterbach, I. Robertson, I.A. Ratiu, V. Bocos-Bintintan, L. Rakosy, S. Woodbourne, *Forests*, **2023**, *14*, 1917.
20. A. Patrut, K.F. von Reden, P. Danthu, J-M. Leong Pock-Tsy, R.T. Patrut, D.A. Lowy, *PLOS One*, **2015**, *10(3)*, e0121170.
21. R.T. Patrut, A. Patrut, J-M Leong Pock-Tsy, S. Woodborne, L. Rakosy, P. Danthu, I.A. Ratiu, J. Bodis, K.F. von Reden, *Studia UBB Chemia*, **2019**, *LXIV*, *4*, 131-39.
22. A. Patrut, R.T. Patrut, J-M. Leong Pock-Tsy, S. Woodborne, L. Rakosy, I.A. Ratiu, J. Bodis, P. Danthu, *Studia UBB Chemia*, **2020**, *LXV*, *4*, 151-158.
23. A. Patrut, R.T. Patrut, J-M. Leong Pock-Tsy, P. Danthu, S. Woodborne, L. Rakosy, I.A. Ratiu, *Forests*, **2021**, *12*, 1258.
24. A. Patrut, K.F. von Reden, P. Danthu, J-M. Leong Pock-Tsy, R.T. Patrut, D.A. Lowy, *PLoS ONE*, **2015**, *10(3)*, e0121170.
25. A. Patrut, R.T. Patrut, P. Danthu, J-M. Leong Pock-Tsy, L. Rakosy, D.A. Lowy, K.F. von Reden, *PLOS One*, **2016**, *11(1)*, e146977.
26. A. Patrut, R.T. Patrut, L. Rakosy, I.A. Ratiu, P. Danthu, J-M. Leong Pock-Tsy, K.F. von Reden, *Studia UBB Chemia*, **2023**, *LXVIII*, *1*, 119-129.
27. A. Patrut, R.T. Patrut, J-M. Leong Pock-Tsy, L. Rakosy, P. Danthu, I.A. Ratiu, J. Bodis, S. Woodbourne, *Studia UBB Chemia*, **2023**, *LXVIII*, *3*, 141-151.
28. F. Slotta, L. Wacker, F. Riedel, K-U. Heussner, K. Hartmann, G. Helle, *Biogeosciences*, **2021**, *18*, 3539-3564.
29. M. Molnar, R. Janovics, I. Major, J. Orsovszki, R. Gonczi, M. Veres, A.G. Leonard, S.M. Castle, *Radiocarbon, **2013**, 55(2-3),* 665-676.

30. M. Molnar, L. Rinyu, M. Veres, M. Seiler, L. Wacker, *Radiocarbon,**2013**, 55(2-3),* 338-344.
31. R. Janovics, I. Futo, M. Molnar, *Radiocarbon, **2018**, 60(5),* 1347-1355.
32. M. Molnar, M. Meszaros, R. Janovics, I. Major,K. Hubay, B. Burgo, T. Varga, K. Kertesz, V. Gergely, A. Vas, G. Orsozovszki, A. Molnar, M. Veres, M. Seiler, L. Wacker, A.J. Timothy Jull, *Radiocarbon*, ***2021**, 63(2),* 499-511.
33. C. Bronk Ramsey, *Radiocarbon, **2009**, 51,* 337-360.
34. P.J. Reimer, W.E.N. Austin, E. Bard, A. Bayliss, P.G. Blackwell, C. Bronk Ramsey, M. Butzin, H. Cheng, R. Lawrence Edwards, M. Friedrich, P.M. Grootes, T.P. Guilderson, I. Hajdas, T.J. Heaton, A. G. Hogg, K.A Hughen, B. Kromer, S.W. Manning, R. Muscheler, J.G. Palmer, C. Pearson, J. van der Plicht, R.W. Reimer, D.A. Richards, E.M. Scott, J.R. Southon, C.S.M. Turney, L. Wacker, F. Adolphi, U. Büntgen, M. Capano, S.M. Fahrni, A. Fogtmann-Schulz, R. Friedrich, P. Köhler, S. Kudsk, F. Miyake, J. Olsen, F. Reinig, M. Sakamoto, A. Sookdeo, S. Talamo, *Radiocarbon*, **2020**, *62(4)*, 727-757.

STUDIA UBB CHEMIA, LXIX, 2, 2024 (p. 121-134)
(RECOMMENDED CITATION)
DOI:10.24193/subbchem.2024.2.09

# WEAK INTERACTIONS BETWEEN HYDRACIDS / BINARY ACIDS: SOME CONSIDERATIONS FROM A DFT ANALYSIS

**Luana RADU[a], Alexandru LUPAN[a], Maria LEHENE[a], Radu SILAGHI-DUMITRESCU[a]***

**ABSTRACT.** Non-covalent interactions involving element-hydrogen contacts are a central part in supramolecular chemistry and play essential roles in biomolecular structure. Reported here is a systematic computational analysis of such interactions within $XH_n$---$YH_m$ dimers, where X and Y are C, Si, N, P, O, S, F and Cl, respectively. Two functionals are employed – the widely used BP86 and the M06-2X functional especially designed for describing noncovalent interactions. The interaction energies are found to be correlated with charge separation to a degree of 80%, suggesting that these noncovalent interactions can be reasonably explained/predicted by their electrostatic component. Energy decomposition analyses on the other hand suggest that correlation effects are the underlying root of the interaction. The rarely discussed intermolecular vibrations are also analyzed and noted to sometimes intercede in the typical observation windows for molecular spectroscopy. Moreover, in some cases notable effects of the non-covalent interactions are noted upon internal vibrations of the partners.

***Keywords:*** *hydracid, binary acid, noncovalent, DFT, supramolecular*

## INTRODUCTION

Non-covalent interactions involving element-hydrogen contacts are a central part in supramolecular chemistry and play essential roles in biomolecular structure. Their accurate computational description has been

[a] *Faculty of Chemistry and Chemical Engineering, Babeș-Bolyai University, Str. Arany Janos Nr. 11, RO-400028 Cluj-Napoca, Romania*
* *Correspondence to: radu.silaghi@ubbcluj.ro*

described extensively, with the importance of very high-level / accurate methods often highlighted.[1–4] We have, on the other hand, shown elsewhere that accurate description of larger, real-life systems whose geometry is based dominantly on hydrogen bonds or on other non-covalent interactions is still elusive despite overconfident statements to the contrary.[5–14]

Chemical Reviews was among the first review journals to recognize the significance of non-covalent interactions and published the first thematic issue on the subject in 1988. Similar reviews followed in 1994, 2000 and 2016.[15]

A series of dimers analyzed in this paper have been also studied in literature, such as: $H_2O$•••$NH_3$, HF•••$CH_4$, $H_2O$•••$CH_4$, HF•••HCl, $H_2O$•••$H_2O$, $H_2O$•••HF, HCl•••$H_2O$, etc. The dimers of $H_2O$ and HF are among the most studied systems for hydrogen bonding. The investigation of the $H_2O$•••HF dimer dates back to 1969 when Kollman and Allen performed the first semiempirical and later ab initio studies of this dimer. The existence of this dimer was confirmed by microwave spectroscopy in 1975. The energies and frequencies of the $H_2O$•••HF dimer have been calculated with CCSD(T) and MP2 methods, and the results from this level of theory provide dissociation energies and frequencies appropriate to experimental values.[16]

The heterogenous dimer, HF•••HCl was first characterized in 1977, but the only configuration detected was ClH•••FH in the microwave spectra of the molecular beam electric resonance experiments. Several years later, Fraser and Pine observed the FH•••ClH configuration in the microwave and infrared (IR) spectra of molecular beams created by expanding a mixture of HCl and HF in helium. Following the characterization (through full geometry optimizations and vibrational frequency analyses) of this system it was concluded that there is an electronic preference of HF to donate and of HCl to accept a hydrogen bond in this dimer.[16]

Reported here is a systematic computational analysis of the non-covalent interactions within $H_nX$---$H_nY$ dimers, where n=1-4 and X and Y are C, Si, N, P, O, S, F and Cl, respectively. Two functionals are employed – the widely used BP86 and the M06-2X functional especially designed for describing noncovalent interactions.[2]

## RESULTS AND DISCUSSION

DFT calculations were performed with two functionals, M06-2X and BP86, to explore the order of magnitude of the dependence of the results on methodology. The M06-2X functional was designed specifically for the study of non-covalent interactions, and thus parametrized to take into account long-

range dispersions. To this extent, at least in its initial report, corrections now common for other functionals (such as Grimme's dispersion) were deemed superfluous for M06-2X.[1,2,17,18] Its performance on describing structures that rely primarily on supramolecular interactions has previously been shown to be distinctly better than that of other methods.[11,12] The BP86 functional was chosen as an example of functional in general use, with the observation that the M06-2X functional in known to far outperforms BP86 and other classical functionals in describing weak interactions; however, in most cases of practical interest classical functionals are still the choice – as M06-2X fails dramatically in, e.g., describing spin states and geometries at transition metal systems.[8–13,19–27] In this context, the BP86 data may be taken as illustrating the degree to which DFT functionals can deviate from the optimum results – while the M06-2X data would be (one of) the optimal functional(s) to employ for the task (of examining systems whose geometry relies entirely on non-covalent interactions). Tables 1 and 2 show the key geometrical parameter in the dimers examined here – i.e. the intermolecular H---X contact, alongside the binding energy between the two monomers. In order to evaluate the computed H---X distance (D), the Tables also shows the sums of van der Waals radii for the respective H---X pair; an attractive interaction should entail a value of D lower than this sum. To offer a measure of the significance of the difference between the DFT-calculated distance D, and the sum of van der Waals radii, also listed in the Tables is a value R defined as the average between the sum of the van der Waals radii and the sum of the covalent radii of the respective atoms. In the ensuing discussion, unless otherwise specified, the M06-2X data are interpreted.

With few exceptions, the distances between atoms that are involved in non-covalent interactions increase as a larger molecule is involved in the system and if the number of hydrogen atoms in the molecule increases. The average distances (obtained by calculating the arithmetic mean of all interactions of the same type from different systems) for each type of interaction are: H---Cl 3.10 Å, H---F 2.39 Å, H---O 2.16 Å, H---S 2.77 Å, H---N 2.25 Å, H---P 3.05 Å, H---C 2.87 Å, H---Si 3.30 Å. The smallest distances (D) identified for each type of interaction are: H---Cl 2.45 Å, H---F 1.82 Å, H---O 1.75 Å, H---S 2.4 Å, H---N 1.67 Å, H---P 2.49 Å, H---C 2.38 Å, H---Si 2.58 Å. The largest distances identified for each type of interaction are: H---Cl 3.33 Å, H---F 2.91 Å, H---O 3.29 Å, H---S 3.04 Å, H---N 3.04 Å, H---P 3.64 Å, H---C 3.33 Å, H---Si 3.66 Å.

Thus, it is observed that the stronger interactions generally settle at values around 2.5 Å; however, there are non-covalent interactions even at distances of about 1.75 Å, while the weaker interactions settle at 3.04 Å, 3.33 Å, 3.66 Å, i.e. at distances greater than 3 Å. Compared to R (R representing the

average between the sum of the van der Waals radii and the sum of the covalent radii of the atoms involved in a non-covalent interaction), the closest and most distant interactions are established at the following distances for each type of interaction: H- --Cl 0.3 Å, respectively 1.18 Å, H---F 0.05 Å, respectively 1.04 Å, H---O 0.04 Å, respectively 1.38 Å, H--- S 0.21 Å and 1.02 Å respectively, H---N 0.05 Å and 1.11 Å respectively, H---P 0.28 Å and 1.43 Å respectively, H---C 0.38 Å and 1.33 Å, H---Si 0.47 Å and 1.08 Å, respectively. Compared to the calculated average distances, the closest and the farthest interactions are set at the following distances for each type of interaction: H---Cl 0.23 Å and 0.65 Å, respectively, H---F 0.51 Å, respectively 0.57 Å, H---O 0.41 Å, respectively 1.12 Å, H---S 0.37 Å, respectively 0.43 Å, H---N 0.57 Å, respectively 0.79 Å, H---P 0.55 Å respectively 0.59 Å, H---C 0.46 Å respectively 0.49 Å, H---Si 0.25 Å respectively 0 .35 Å. Marked in Tables 1 and 2 in italics are the instances where the predicted intermolecular contacts are larger than the sums of van der Waals radii: ClH---ClH, $OH_2$--- $SiH_4$, $SH_2$---ClH, $SH_2$--- $SiH_4$, $PH_3$---ClH, $PH_3$---FH, $PH_3$---$SH_2$, $PH_3$--- $PH_3$, $PH_3$---$CH_4$, $PH_3$---$SiH_4$, $NH_3$---ClH, $NH_3$---$PH_3$, $NH_3$---$SiH_4$, $CH_4$---ClH, $CH_4$---FH, $CH_4$---$PH_3$, $CH_4$---$CH_4$, $CH_4$--- $SiH_4$, $SiH_4$---ClH, $SiH_4$---FH, $SiH_4$---$OH_2$, $SiH_4$---$SH_2$, $SiH_4$---$NH_3$, $SiH_4$---$PH_3$, and $SiH_4$---$CH_4$. This list thus includes 11 of the Si models (~70% of the total of 15 Si models), 9 of the P models, 4 of the S models, and 3 of the Cl models. There is thus a clear trend for heavier and softer elements to not engage in well-defined intermolecular element-hydrogen interactions – and this is especially true for Si and P. In the case of Si, this expectedly involves the Si in $SiH_4$ as an acceptor (due to sterical constraints by the tetrahedral coordination geometry at Si), but also the protons in $SiH_4$. Also marked in Tables 1 and 2 are the cases where D is smaller than R – i.e. cases where the intermolecular distance would be closer to the sum of covalent radii than to the sum of van der Waals radii. These particularly strong interactions involve the pairs ClH---$OH_2$, ClH---$NH_3$, FH---FH, FH---$OH_2$, FH---$NH_3$, $OH_2$---ClH, $OH_2$---FH, and $NH_3$---FH –dominantly involving the two most electronegative elements of the set examined here – fluorine (5 out of 8 pairs on the list) and oxygen (4) , followed closely by their neighbors nitrogen and chlorine (3 instances each).

For the H---Cl the interaction energy is in most systems ~0.6 kcal/mol, with values ranging from 0.4 kcal/mol for the HCl dimer HCl to 2.5 kcal/mol for the HF/HCl pair. For the H---F interaction, the values range from 5.7 kcal/mol in the HF dimer to 0.6 kcal/mol in the pairs with $CH_4$ and $PH_3$. For H---O, the energies range from 9.4 kcal/mol in the $H_2O$/HF pair, to 1.4 kcal/mol in the HF/$SiH_4$ pair. For the H---S interaction, the values range from 4.4 kcal/mol for the $H_2S$/HF pair to 0.6 kcal/mol with $PH_3$. For the H---N interactions, energies range from 13.2 kcal/mol in the $NH_3$ pairs with HCl or HF, to 0.6 kcal/mol in the pairs with $PH_3$, $CH_4$ and $SiH_4$. For the H---P interaction, the

lowest energy is found in the $PH_3/CH_4$ pair with 0.2 kcal/mol, while the strongest interaction is in the $PH_3$/HF pair, with 4.4 kcal/mol. The H---C interaction is a weak one regardless of the system components, ranging from 0.5 kcal/mol in the methane dimer to 1.3 in the $CH_4$/HF pair. The H---Si interaction is also of weak intensity, ranging from 0.6 kcal/mol (in the $SiH_4$ pairs with HF or $CH_4$) to 2.5 kcal /mol in the water/$SiH_4$ pair.

**Table 1.** H---X intermolecular distances (D, Å), sums of van der Waals radii (vdW, Å), average between vdW and the sums of covalent radii (R, Å) and interaction energies (kcal/mol) for $XH_n$---$YH_m$ systems with X = Cl, F, O, S. BP86 data are shown in grey. *Italics: D>vdW*; **bold: D<R**.

| dimer | contact | R | vdW | D | ΔE | D | ΔE |
|---|---|---|---|---|---|---|---|
| ClH---ClH | H---Cl | 2.15 | 2.95 | *3.27* | 0.41 | 4.8 | 0.15 |
| ClH---FH | H---F | 1.87 | 2.67 | 1.97 | 3.8 | 1.9 | 3.61 |
| ClH---$OH_2$ | H---O | 1.91 | 2.72 | **1.85** | 7.28 | 1.75 | 7.83 |
| ClH---$SH_2$ | H---S | 2.19 | 3.00 | 2.50 | 3.55 | 2.34 | 3.93 |
| ClH---$NH_3$ | H---N | 1.93 | 2.75 | **1.67** | 11.71 | 1.62 | 13.25 |
| ClH---$PH_3$ | H---P | 2.21 | 3.00 | 2.58 | 3.51 | 2.42 | 3.66 |
| ClH---$CH_4$ | H---C | 2.00 | 2.90 | 2.52 | 1.11 | 2.63 | 0.20 |
| ClH---$SiH_4$ | H---Si | 2.58 | 3.30 | 3.12 | 0.71 | 9.27 | 0.00 |
| FH---ClH | H---Cl | 2.15 | 2.95 | 2.45 | 2.51 | 2.45 | 1.88 |
| FH---FH | H---F | 1.87 | 2.67 | **1.82** | 5.65 | 1.81 | 5.02 |
| FH---$OH_2$ | H---O | 1.91 | 2.72 | **1.75** | 9.41 | 1.74 | 8.79 |
| FH---$SH_2$ | H---S | 2.19 | 3.00 | 2.40 | 4.39 | 2.35 | 4.39 |
| FH---$NH_3$ | H---N | 1.93 | 2.75 | **1.75** | 13.18 | 1.73 | 13.18 |
| FH---$PH_3$ | H---P | 2.21 | 3.00 | 2.49 | 4.39 | 2.43 | 3.77 |
| FH---$CH_4$ | H---C | 2.00 | 2.90 | 2.38 | 1.26 | 2.49 | 0.63 |
| FH---SiH4 | H---Si | 2.58 | 3.30 | 3.05 | 0.63 | 3.23 | 0.63 |
| $OH_2$---ClH | H---O | 1.91 | 2.72 | **1.85** | 7.53 | 1.75 | 7.53 |
| $OH_2$---FH | H---O | 1.91 | 2.72 | **1.76** | 9.41 | 2.01 | 2.51 |
| $OH_2$---$OH_2$ | H---O | 1.91 | 2.72 | 1.95 | 6.28 | 1.94 | 5.02 |
| $OH_2$---$SH_2$ | H---S | 2.19 | 3.00 | 2.61 | 3.14 | 2.60 | 2.51 |
| $OH_2$---$NH_3$ | H---N | 1.93 | 2.75 | 1.98 | 7.53 | 1.94 | 6.90 |
| $OH_2$---$PH_3$ | H---P | 2.21 | 3.00 | 2.71 | 2.51 | 2.73 | 1.88 |
| $OH_2$---$CH_4$ | H---C | 2.00 | 2.90 | 2.56 | 0.63 | 2.90 | 0.00 |
| $OH_2$---$SiH_4$ | H---Si | 2.58 | 3.30 | *3.54* | 2.51 | 4.73 | 0.00 |
| $SH_2$---ClH | H---Cl | 2.15 | 2.95 | *3.06* | 0.63 | 2.87 | 0.63 |
| $SH_2$---FH | H---F | 1.87 | 2.67 | 2.19 | 1.88 | 2.19 | 1.26 |
| $SH_2$---$OH_2$ | H---O | 1.91 | 2.72 | 2.11 | 3.77 | 2.04 | 3.14 |
| $SH_2$---$SH_2$ | H---S | 2.19 | 3.00 | 2.86 | 1.88 | 2.73 | 1.26 |
| $SH_2$---$NH_3$ | H---N | 1.93 | 2.75 | 2.12 | 5.02 | 1.99 | 5.65 |
| $SH_2$---$PH_3$ | H---P | 2.21 | 3.00 | 2.92 | 1.88 | 2.84 | 1.26 |
| $SH_2$---$CH_4$ | H---C | 2.00 | 2.90 | 2.76 | 0.63 | 5.42 | 0.00 |
| $SH_2$---$SiH_4$ | H---Si | 2.58 | 3.30 | *3.66* | 1.26 | 6.73 | 0.00 |

**Table 2.** H---X intermolecular distances (D, Å), sums of van der Waals radii (vdW, Å), average between vdW and the sums of covalent radii (R, Å) and interaction energies (kcal/mol) for $XH_n$---$YH_m$ systems with X = P, N, C, Si. BP86 data are shown in grey. *Italics: D>vdW*; **bold: D<R**.

| dimer | contact | R | vdW | D | ΔE | D | ΔE |
|---|---|---|---|---|---|---|---|
| $PH_3$---ClH | H---Cl | 2.15 | 2.95 | *3.21* | 0.63 | 5.65 | 0.00 |
| $PH_3$---FH | H---F | 1.87 | 2.67 | *2.77* | 0.63 | 2.43 | 3.77 |
| $PH_3$---$OH_2$ | H---O | 1.91 | 2.72 | 2.44 | 1.26 | 2.52 | 0.63 |
| $PH_3$---$SH_2$ | H---S | 2.19 | 3.00 | *3.21* | 0.63 | 5.4 | 0.00 |
| $PH_3$---$NH_3$ | H---N | 1.93 | 2.75 | 2.52 | 1.26 | 2.44 | 1.26 |
| $PH_3$---$PH_3$ | H---P | 2.21 | 3.00 | *3.61* | 1.26 | 3.69 | 0.00 |
| $PH_3$---$CH_4$ | H---C | 2.00 | 2.90 | *3.23* | 0.63 | 6.08 | 0.00 |
| $PH_3$---$SiH_4$ | H---P | 2.21 | 3.00 | *3.26* | 1.26 | 8.05 | 0.00 |
| $NH_3$---ClH | H---Cl | 2.15 | 2.15 | *3.10* | 0.63 | 1.62 | 13.18 |
| $NH_3$---FH | H---N | 1.93 | 2.75 | **1.75** | 13.18 | 1.73 | 13.18 |
| $NH_3$---$OH_2$ | H---N | 1.93 | 2.75 | 1.98 | 7.53 | 2.18 | 2.51 |
| $NH_3$---$SH_2$ | H---N | 1.93 | 2.75 | 2.12 | 5.02 | 1.99 | 5.65 |
| $NH_3$---$NH_3$ | H---N | 1.93 | 2.75 | 2.21 | 3.77 | 2.19 | 3.14 |
| $NH_3$---$PH_3$ | H---N | 1.93 | 2.75 | *3.04* | 0.63 | 3.07 | 2.51 |
| $NH_3$---$CH_4$ | H---N | 1.93 | 2.75 | 2.60 | 0.63 | 5.25 | 0.00 |
| $NH_3$---$SiH_4$ | H---Si | 2.58 | 2.58 | *3.35* | 1.26 | 13.38 | 0.00 |
| $CH_4$---ClH | H---Cl | 2.15 | 2.95 | *3.31* | 0.63 | 5.85 | 0.00 |
| $CH_4$---FH | H---F | 1.87 | 2.67 | *2.69* | 0.63 | 3.90 | 0.00 |
| $CH_4$---$OH_2$ | H---O | 1.91 | 2.72 | 2.46 | 0.63 | 2.74 | 0.00 |
| $CH_4$---$SH_2$ | - | - | - | - | | 5.88 | 0.63 |
| $CH_4$---$NH_3$ | H---N | 1.93 | 2.75 | 2.57 | 0.63 | 2.66 | 0.63 |
| $CH_4$---PH3 | H---P | 2.21 | 3.00 | *3.64* | 0.23 | 5.80 | 0.01 |
| CH4---$CH_4$ | H---C | 2.00 | 2.90 | *3.30* | 0.49 | 5.68 | 0.38 |
| $CH_4$---$SiH_4$ | H---Si | 2.58 | 3.30 | 3.23 | 0.63 | 7.30 | 0.00 |
| $SiH_4$---ClH | H---Cl | 2.15 | 2.95 | *3.33* | 0.21 | 6.27 | 0.00 |
| $SiH_4$---FH | H---F | 1.87 | 2.67 | *2.91* | 1.26 | 4.03 | 0.00 |
| $SiH_4$---$OH_2$ | H---O | 1.91 | 2.72 | *3.29* | 0.00 | 4.08 | 0.00 |
| $SiH_4$---$SH_2$ | H---S | 2.19 | 3.00 | *3.06* | 1.26 | 6.37 | 0.00 |
| $SiH_4$---$NH_3$ | H---N | 1.93 | 2.75 | *2.92* | 3.14 | 11.51 | 0.00 |
| $SiH_4$---$PH_3$ | H---P | 2.21 | 3.00 | *3.18* | 1.26 | 6.70 | 0.00 |
| $SiH_4$---$CH_4$ | H---C | 2.00 | 2.90 | *3.33* | 0.63 | 6.65 | 0.00 |
| $SiH_4$---$SiH_4$ | H---Si | 2.58 | 3.30 | 3.17 | 1.26 | 7.11 | 0.00 |

In the following, the results obtained with the BP86 functional will be briefly discussed, specifying that the assemblies in which the intermolecular distance is greater than 5 Å have been excluded from the discussion. The average distances (obtained by calculating the arithmetic mean of all interactions of the same type from different systems) for each type of interaction are: H---Cl 3.37 Å, H---F 2.64 Å, H---O 2.30 Å, H---S 2.505 Å, H---N 1.99 Å, H---P 2.80 Å,

H---C 2.67 Å, H---Si 3, 98 Å. Compared to the calculated average distances, the closest and most distant interactions are found at the following distances for each type of interaction: H---Cl 0.50 Å, respectively 1.43 Å, H---F 0.45 Å, respectively 1.39 Å, H---O 0.12 Å, respectively 1.78 Å, H---S 0.10 Å, respectively 0.23 Å, H---N 0 Å, respectively 0 .67 Å, H---P 0.07 Å and 0.89 Å respectively, H---C 0.04 Å and 0.23 Å respectively, H---Si 0.75 Å. Relative to R, the closest and most distant interactions are found at the following distances for each type of interaction: H---Cl 0.30 Å and 2.65 Å respectively, H---F 0.03 Å, respectively 2.03 Å, H---O 0.03 Å respectively 2.17 Å, H---S 0.15 Å respectively 0.54 Å, H---N 0.01 Å respectively 0 .73 Å, H---P 0.21 Å, respectively 1.48 Å, H---C 0.49 Å, respectively 0.9 Å, H---Si 0.65 Å, respectively 2.15 Å. The smallest distances identified for each type of interaction are: H---Cl 2.45 Å, H---F 1.81 Å, H---O 1.74 Å, H---S 2.34 Å, H---N 1.62 Å, H---P 2.42 Å, H---C 2.49 Å, H---Si 3.23 Å. The BP86 functional often fails to give ΔE of the order of kcal/mol, in many cases ΔE being approximated to 0 kcal/mol. Overall, we find that in general the BP86 functional leads to energy differences ΔE that are smaller than those obtained using the M06-2X functional. Regarding the distances between the atoms involved in the non-covalent interaction, there are significant differences between the results obtained with the two functionals, especially in the case of systems containing larger molecules. If one averages all the distances obtained with the two functionals, a value of 2.68 Å is obtained for the M06-2X functional and an average of 3.94 Å for the BP86 functional. In the case of energies, an average of 2.9 kcal/mol is obtained for the M06-2X functional, and 2.5 kcal/mol for the BP86 functional. Even if the difference between these averages does not seem large at first glance, upon closer analysis we find that in fact the higher values obtained compensate for those approximated by 0. As a general note, the very small values seen even with M06-2X should be interpreted with caution – especially when below 2 kcal/mol. While the trends are expected to be correctly reproduced, the exact values may still be in error and in principle even improved by more accurate post-HF approaches and/or further corrections (e.g., counterpoise, dispersion).

Figure 1 illustrates the correlations between the Mulliken partial atomic charges on the two units – which are an indication of the degree of polarity of the interaction - and the binding energies, at $R^2$~0.7. Better correlations are seen in the pairs with stronger overall interactions and with more linear X-H---Y geometries (e.g., 0.97 for ClH---YHm in Figure 2). These numbers illustrate the predominantly/majorly electrostatic nature of the non-covalent intermolecular interactions examined here, in line with considerations consistently made about hydrogen bonds in general, but not only.[5,6]

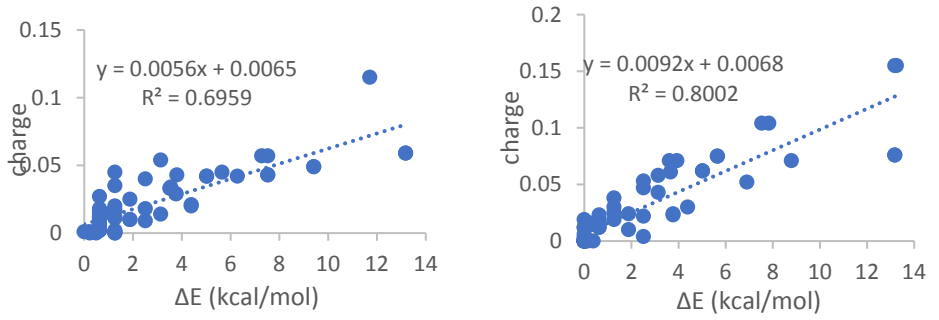


**Figure 1.** Correlation between the binding energies (ΔE) and Mulliken atomic charges, from M06-2X (left) and BP86 (right) calculations.

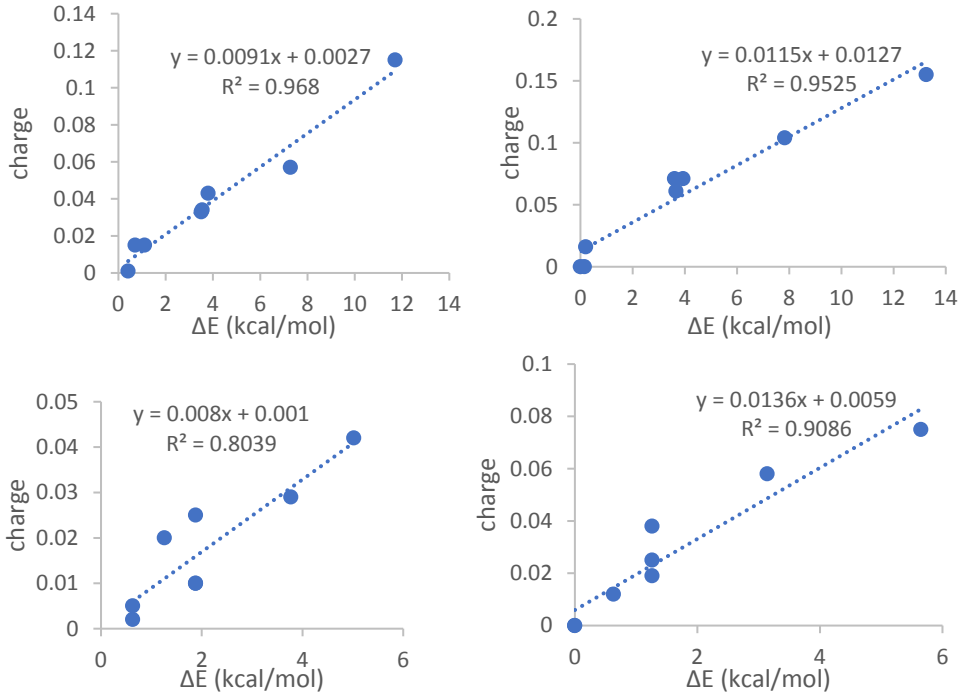


**Figure 2.** Correlations between the binding energies (ΔE) and Mulliken charges, from M06-2X (left) and BP86 (right) calculations for the ClH-$YH_m$ (top) and $OH_2$---$YH_m$ (bottom) sets of models.

The vibration frequencies for all models have been compared with the frequencies seen in the molecule whose hydrogen was involved in the interaction in the initial geometry. A large number of intermolecular vibrations may be noted; this is expected to impact the total energy of the system. Most of these frequencies occur in regions rarely explorable experimentally for large molecules of practical interest (i.e., below 400 $cm^{-1}$ – although this is somewhat of a circular comment since such vibrations from the solvent/ medium will be those responsible for the experimental limitations). However, larger values are seen for the models where the proton donors in the $XH_n$---$YH_m$ dimers are $NH_3$, FH or ClH (up to~1000 $cm^{-1}$), $OH_2$ (up to ~800 $cm^{-1}$), $SH_2$ and $PH_3$ (up to ~5-600 $cm^{-1}$). It is expected that such frequencies should be observable not only in such dimeric mixtures as analyzed here, but also in more complex environments, including ones where the element-hydrogen bonds examined here are in fact parts of more complex molecular structures (indeed, while most of the larger frequencies involve the strong acids HF and HCl which would be dissociated in water, several of them also only involve only water, hydrogen sulfide and ammonia – which may be taken as prototypes of hydroxyl, amino and sulfhydryl groups, respectively). Such intermolecular vibrations are inherently ignored in most rationalizations of vibrational spectra when (as usually is the case) monomolecular models are employed.

Also of practical interest, we may note that the inherent vibrations of the hydrogen-donating molecule shift upon interaction with the various partners by a various degrees: up to 10 $cm^{-1}$ in $CH_4$ but with a few exceptions of up to 200 $cm^{-1}$ at high frequencies, similarly in $SiH_4$ (but with exceptions only going up to ~20 $cm^{-1}$), $NH_3$ (one exception of ~70 $cm^{-1}$ at ~1100 $cm^{-1}$), and $PH_3$ (exceptions of up to ~40 $cm^{-1}$). For $OH_2$, distinct effects are seen, of 40 and 130 $cm^{-1}$ for two of the total of three bands ion the spectrum; $SH_2$ behaves somewhat similarly, although with smaller effects than seen in $OH_2$. For FH and ClH, the effects are even larger (600 and 900 $cm^{-1}$, respectively). Overall, the strength of the intermolecular effects on the vibrational spectrum is thus (expectedly) seen to increase with the strength of the intermolecular interaction and to be more efficient in systems with well-aligned $H_{n-1}X$-H---$YH_m$ units (especially those involving diatomics, and more efficiently for lower values of n and m).

The importance of solvation is well recognized in predicting molecular structures and properties, including spectra.[28–30] However, in most cases implicit solvation models are employed, or, more rarely, relatively small explicit models. The results shown here may suggest that explicit solvation may be essential for describing spectroscopic properties in cases where stronger and directionally well-defined supramolecular interactions occur.

On a methodological note, when comparing the M06-2X functional to BP86, a decrease in vibration frequency values by 3-5% is observed. The largest discrepancy occurs in the case of the SiH4 molecule, 6.5%, and the smallest in the case of the water molecule, 0.8%.

Further on methodological aspects, Tables 3 and 4 illustrate representative data from energy decomposition analyses on two extreme cases from our set of dimers – $CH_4$---$CH_4$ and HF---HF from M06-2X calculations (with similar data available for BP86 calculations). The electrostatic component of the interaction energy in Tables 3 and 4 is in fact seen to be almost identical between the methane dimer vs. the HF dimer – despite the fact that the total interaction energy is stronger by ~5 kcal/mol in the HF case (and essentially zero in the methane case). The above-discussed data on Mulliken charges does convincingly show correlations between the interaction energies and the magnitude of charge separation. Interestingly, Tables 3 and 4 suggest this to be mere correlation and not causation. Instead, a notable part of the ~5 kcal/mol interaction energy within the HF dimer appears to originate from the difference between the sterical and the quantum effects. These two terms in turn are derived from quantities enumerated in the upper rows of Tables 3 and 4.

**Table 3.** Extended Transition State - Natural Orbitals for Chemical Valence (ETS-NOCV) analysis and Shubin Liu's energy decomposition analysis (EDA-SBL) for the $CH_4$---$CH_4$ structure optimized with M06-2X.

| **Type of Energy** | **Energy (Hartree)** | | | **Energy (kcal/mol)** |
|---|---|---|---|---|
| **ETS-NOCV energy decomposition terms** | Full structure $CH_4$—$CH_4$ | Fragment 1 $CH_4$ | Fragment 2 $CH_4$ | ΔE |
| Electronic kinetic energy (ET) | 80.639 | 40.321 | 40.317 | -0.137 |
| Weizsacker kinetic energy (TW) | 65.539 | 32.780 | 32.780 | -13.368 |
| Interelectronic Coulomb repulsion energy (EJ) | 77.694 | 32.852 | 32.842 | 7530.332 |
| Internuclear Coulomb repulsion energy (ENuc) | 39.045 | 13.526 | 13.516 | 7531.834 |
| Nuclear-electronic Coulomb attraction energy (EV) | -264.602 | -120.311 | -120.288 | -15061.920 |
| Energy without electronic correlation (ET+EV+EJ+ENuc) | -67.224 | -33.612 | -33.613 | 0.109 |
| Exchange correlation energy (Ex) | -13.065 | -6.533 | -6.532 | 0.315 |
| Coulomb correlation energy (Ec) | -0.776 | -0.388 | -0.388 | -0.312 |
| Pauli kinetic energy (ET-TW) | 15.100 | 7.542 | 7.537 | 13.230 |
| **EDA-SBL energy decomposition terms** | | | | |
| E_steric: | 65.539 | 32.780 | 32.780 | -13.368 |
| E_electrostatic: | -147.863 | -73.933 | -73.930 | 0.246 |
| E_quantum: | 1.259 | 0.620 | 0.617 | 13.233 |
| E_total: | -81.065 | -40.533 | -40.533 | 0.111 |

Some of the latter are dependent on the total number of particles in the system, but one may note that the correlation effects are essentially zero on the methane dimer, but amount to ~70% of the total interaction energy in the HF dimer. The intrinsic asymmetry of the monomeric units (HF vs. methane) may in principle be a common cause for both the subsequent charge separation and correlation. However, confirmation and full exploration of such hypotheses would require a systematic analysis of the set of dimers, as opposed to only the two extremes – which is within the scope of a subsequent report.

**Table 4.** Extended Transition State - Natural Orbitals for Chemical Valence (ETS-NOCV) analysis and Shubin Liu's energy decomposition analysis (EDA-SBL) for the FH---FH structure optimized with M06-2X.

| **Type of Energy** | **Energy (Hartree)** | | | **Energy (kcal/mol)** |
|---|---|---|---|---|
| **ETS-NOCV energy decomposition terms** | Full structure FH--FH | Fragment 1 FH | Fragment 2 FH | ΔE |
| Electronic kinetic energy (ET) | 200.834 | 100.419 | 100.419 | -2.172 |
| Weizsacker kinetic energy (TW) | 146.106 | 73.124 | 73.124 | -89.795 |
| Interelectronic Coulomb repulsion energy (EJ) | 131.979 | 56.050 | 56.050 | 12473.902 |
| Internuclear Coulomb repulsion energy (ENuc) | 30.883 | 5.412 | 5.412 | 12587.314 |
| Nuclear-electronic Coulomb attraction energy (EV) | -542.861 | -251.462 | -251.462 | -25060.665 |
| Energy without electronic correlation (ET+EV+EJ+ENuc) | -179.165 | -89.581 | -89.581 | -1.621 |
| Exchange correlation energy (Ex) | -20.842 | -10.420 | -10.420 | -1.524 |
| Coulomb correlation energy (Ec) | -0.935 | -0.466 | -0.466 | -1.912 |
| Pauli kinetic energy (ET-TW) | 54.729 | 27.294 | 27.294 | 87.623 |
| **EDA-SBL energy decomposition terms** | | | | |
| E_steric: | 146.106 | 73.124 | 73.124 | -89.795 |
| E_electrostatic: | -379.999 | -190.000 | -190.000 | 0.551 |
| E_quantum: | 32.951 | 16.409 | 16.409 | 84.187 |
| E_total: | -200.942 | -100.467 | -100.467 | -5.057 |

## EXPERIMENTAL SECTION

Dimeric models $XH_n$---$YH_m$, where n,m=1-4 and X and Y are C, Si, N, P, O, S, F and Cl, respectively (i.e., involving HF, HCl, $H_2O$, $H_2S$, $NH_3$, $PH_3$, $CH_4$ and $SiH_4$), were built using the Spartan[31] graphical interface so that there would be a linear X---H-Y unit, with the X---H distance slightly below the sum of van der Waals radii. Geometries were optimized using the M06-2X and

BP86 functionals and the 6-311G(d,p) basis set within the Gaussian software package.[32] Vibrational spectra were verified so that no negative frequencies would be present (i.e., the structures were true energy minima). Solvation was not included, as most of the systems examined here would not be viable in usual solvents (either because of dissociation, or because of solvation). Relative energies (ΔE) listed in Tables 1 and 2 represent the difference between the energy of the energy of the $XH_n$---$YH_m$ pair and the isolated $XH_n$ and $YH_m$ systems calculated separately; positive values imply an attractive interaction.

For the energy decomposition analysis Multiwfn[33] was used. With the Extended Transition State - Natural Orbitals for Chemical Valence (ETS-NOCV) analysis[34–36] method, the energy decomposition terms were calculated, where the structures was separated in two main fragments. The steric, electrostatic, quantum and total energies were calculated with Shubin Liu's energy decomposition (EDA-SBL)[37] method.

## CONCLUSIONS

Reported here is a systematic computational analysis of such interactions within $XH_n$---$YH_m$ dimers, where X and Y are C, Si, N, P, O, S, F and Cl, respectively. The interaction energies are found to be correlated with charge separation to a degree of 80%, suggesting that these noncovalent interactions can be reasonably explained/predicted by their electrostatic component – though energy decomposition analyses exploring the phenomenon in more detail appear to indicate a role for correlation effects more so than electrostatics. The rarely discussed intermolecular vibrations are also analyzed and noted to sometimes intercede in the typical observation windows for molecular spectroscopy. Moreover, in some cases notable effects of the non-covalent interactions are noted upon internal vibrations of the partners.

## ACKNOWLEDGMENTS

Drs. Daniela Cioloboc and Adrian M.V Brânzanic (UBB) are thanked for helpful discussions and technical support.

## Supporting Information available

Tables containing vibrational frequencies, Figures illustrating geometries – available upon request from the authors.

## REFERENCES

1. Zhao, Y.; Truhlar, D. G. A *J. Chem. Phys.* **2006**, No. 125, 194101–194118.
2. Zhao, Y.; Truhlar, D. G. *Theor. Chem. Acc.* **2008**, *120*, 215–241.
3. Grimme, S. *J. Comput. Chem.* **2006**, *27*, 1787–1799. https://doi.org/10.1002/jcc.
4. Radu, L. BSc Diploma Paper: Studiul Interacțiunilor Necovalente. Studii Experimentale Și Teoretice, Babes-Bolyai University, 2014.
5. Silaghi-Dumitrescu, L.; Attia, A. A. A.; Silaghi-Dumitrescu, R.; Blake, A. J.; Sowerby, D. B. *Inorg. Chim. Acta* **2018**, *475*, 120–126. https://doi.org/10.1016/j.ica.2017.08.052.
6. Silaghi-Dumitrescu, R.; Lupan, A. *Cent. Eur. J. Chem.* **2013**, *11* (3), 457–463.
7. Irsai, I.; Majdik, C.; Lupan, A.; Silaghi-Dumitrescu, R. *J. Math. Chem.* **2012**, *50* (4), 703–733.
8. Carrascoza, F.; Zaric, S.; Silaghi-Dumitrescu, R. *J. Mol. Graph. Model.* **2014**, *50*, 125–133.
9. Irsai, I.; Pesek, S. Z.; Silaghi-Dumitrescu, R. *Studia UBB Chemia.* **2022**, *67* (4), 47–72.
10. Irsai, I.; Lupan, A.; Majdik, C.; Silaghi-Dumitrescu, R. *Studia UBB Chemia.* **2017**, *62* (4), 495–513.
11. Silaghi-Dumitrescu, R. *Studia UBB Chemia.* **2010**, *60(1),* 31–36.
12. Lupan, A.; Kun, A.-Z. Z.; Carrascoza, F.; Silaghi-Dumitrescu, R. Performance *J. Mol. Model.* **2013**, *19* (1), 193–203.
13. Carrascoza Mayen, J. F.; Lupan, A.; Cosar, C.; Kun, A.-Z.; Silaghi-Dumitrescu, R. *Biophys. Chem.* **2015**, *197*, 10–17.
14. Pesek, S.; Lehene, M.; Brânzanic, A. M. V.; Silaghi-Dumitrescu, R. *Molecules* **2022**, *27* (24), 8974.
15. Hobza, P.; Řezáč, J. *Chem. Rev.* **2016**, *116* (9), 4911–4912.
16. Sexton, T. M.; Howard, J. C.; Tschumper, G. S. *J. Phys. Chem. A* **2018**, *122* (21), 4902–4908.
17. Leverentz, H. R.; Truhlar, D. G. *J Phys Chem A* **2008**, *112* (26), 6009–6016.
18. Zhao, Y.; Truhlar, D. G. *J. Phys. Chem. A* **2005**, *109* (25), 5656–5667.
19. Silaghi-Dumitrescu, R.; Silaghi-Dumitrescu, I. *J. Inorg. Biochem.* **2006**, *100* (1), 161–166.
20. Attia, A. A. A.; Silaghi-Dumitrescu, R. A *J. Mol. Graph. Model.* **2016**, *69*, 103–110.
21. Xie, Y. M.; Schaefer, H. F.; Silaghi-Dumitrescu, R.; Peng, B.; Li, Q. S.; Stearns, J. A.; Rizzo, T. R. *Chem. Eur. J.* **2012**, *18* (41), 12941–12944.
22. Attia, A. A. A.; Lupan, A.; Silaghi-Dumitrescu, R. *RSC Adv.* **2013**, *3* (48), 26194–26204.
23. Brânzanic, A. M. V.; Ryde, U.; Silaghi-Dumitrescu, R. I *J. Inorg. Biochem.* **2020**, *203*, 110928.
24. Silaghi-Dumitrescu, R. A *Studia UBB Chemia,* **2007**, *52* (2), 127–139.
25. Silaghi-Dumitrescu, R.; Silaghi-Dumitrescu, I. *Rev. Roum. Chim.* **2004**, *49*, 257–268.

26. Surducan, M.; Makarov, S. V.; Silaghi-Dumitrescu, R. *Eur. J. Inorg. Chem.* **2014**, *34* (34), 5827–5837..
27. Attia, A. A. A.; Cioloboc, D.; Lupan, A.; Silaghi-Dumitrescu, R. *J. Inorg. Biochem.* **2016**, *165*, 49–53.
28. Tomasi, J.; Mennucci, B.; Cammi, R. *Chem. Rev.* **2005**, *105* (8), 2999–3093.
29. Barone, V.; Cossi, M. *J. Phys. Chem. A* **1998**, *102* (97), 1995–2001.
30. Klamt, A.; Jonas, V.; Bürger, T.; Lohrenz, J. C. W. *J. Phys. Chem. A* **1998**, *102* (26), 5074–5085.
31. SPARTAN '18 for Windows, Wavefunction Inc., 18401 Von Karman Avenue, Suite 370 Irvine, CA 92612. 2018.
32. Frisch, M. J.; Trucks, G. W.; Schlegel, H. B.; Scuseria, G. E.; Robb, M. A.; Cheeseman, J. R.; Scalmani, G.; Barone, V.; Petersson, G. A.; Nakatsuji, H.; Li, X.; Caricato, M.; Marenich, A.; Bloino, J.; Janesko, B. G.; Gomperts, R.; Mennucci, B.; Hratchian, H. P.; Ortiz, J. V.; Izmaylov, A. F.; Sonnenberg, J. L.; Williams-Young, D.; Ding, F.; Lipparini, F.; Egidi, F.; Goings, J.; Peng, B.; Petrone, A.; Henderson, T.; Ranasinghe, D.; Zakrzewski, V. G.; Gao, J.; Rega, N.; Zheng, G.; Liang, W.; Hada, M.; Ehara, M.; Toyota, K.; Fukuda, R.; Hasegawa, J.; Ishida, M.; Nakajima, T.; Honda, Y.; Kitao, O.; Nakai, H.; Vreven, T.; Throssell, K.; MontgomeryJr., J. A.; Peralta, J. E.; Ogliaro, F.; Bearpark, M.; Heyd, J. J.; Brothers, E.; Kudin, K. N.; Staroverov, V. N.; Keith, T.; Kobayashi, R.; Normand, J.; Raghavachari, K.; Rendell, A.; Burant, J. C.; Iyengar, S. S.; Tomasi, J.; Cossi, M.; Millam, J. M.; Klene, M.; Adamo, C.; Cammi, R.; Ochterski, J. W.; Martin, R. L.; Morokuma, K.; Farkas, O.; Foresman, J. B.; Fox, D. J. Gaussian 09, Revision E.01. *Gaussian 09, Revision E.01, Gaussian, Inc., Wallingford CT, 2016*. Gaussian, Inc.: Wallingford CT, 2016.
33. Lu, T.; Chen, F. *J. Comput. Chem.* **2012**, *33* (5), 580–592.
34. Mitoraj, M. P.; Michalak, A.; Ziegler, T. *J. Chem. Theory Comput.* **2009**, *5* (4), 962–975.
35. Michalak, A.; Mitoraj, M.; Ziegler, T. *J. Phys. Chem. A* **2008**, *112* (9), 1933–1939.
36. Ziegler, T.; Rauk, A. *Theor. Chim. Acta* **1977**, *46* (1), 1–10..
37. Cao, X.; Liu, S.; Rong, C.; Lu, T.; Liu, S. *Chem. Phys. Lett.* **2017**, *687*, 131–137.

STUDIA UBB CHEMIA, LXIX, 2, 2024 (p. 135-150)
(RECOMMENDED CITATION)
DOI:10.24193/subbchem.2024.2.10

# NUTRITIONAL COMPOSITION AND ANTIOXIDANT CAPACITY OF COMMON BEAN (*PHASEOLUS VULGARIS* L.) CORE COLLECTION

**Aleksandra ILIĆ[a]*, Dejan PRVULOVIĆ[b], Radenka KOLAROV[b], Sonja GVOZDENAC[a], Slađana MEDIĆ-PAP[a], Dario DANOJEVIĆ[a], Vukašin POPOVIĆ[a]**

**ABSTRACT.** Variation of common bean (*Phaseolus vulgaris* L.) core collection was assessed based on the main nutritive and bioactive components. Nutritional profile was described for each cultivar and landrace. Protein content was in the familiar range for common bean (19.6-31.6%). Detected variability for potassium, sulphur, iron and zinc was 7.78, 16.7, 14.99, and 40.17%, respectively. Total phenolic content ranged from 1.8 to 14.1 mg GAE /g DW, with high variation (CV = 41.3%). Likewise, antioxidant tests DPPH, ABTS and FRAP had high, genotype-based, CV in range 29-46%. With the application of PCA and cluster analysis, better insight in underlying germplasm structure was acknowledged, as well accession's grouping based on the studied traits. Cultivars Vulkan and Panonski tetovac, breeding line HR45, landraces L24, L92, L119, L120, and L125 had larger amounts of iron, nitrogen, and proteins. Elevated phenolic content was observed in cultivars Balkan and Spinel, as well as landraces L19, L29, L41 and L60. In addition, cultivar Royal Dutch was recognized for higher levels of zinc, and higher antioxidant capacity revealed by DPPH, ABTS, and FRAP assays. Therefore, these tests could be used in the selection of the accessions for breeding for nutritive quality enhancing.

***Keywords:*** *nutritive value, bioactive compounds, variability, landraces, cultivars*

[a] *Institute of Field and Vegetable Crops, National Institute of the Republic of Serbia, Maksima Gorkog 30, Novi Sad, Serbia*
[b] *University of Novi Sad, Faculty of Agriculture, Trg Dositeja Obradovića 8, Novi Sad, Serbia*
** Corresponding author aleksandra.savic@ifvcns.ns.ac.rs*

## INTRODUCTION

Due to its high nutritional value, common bean (*Phaseolus vulgaris* L.) is one of the most valuable legumes for human consumption worldwide. Moreover, it is recognized as a very diverse crop in terms of different types of cultivation methods, phenotypic and genotypic variability, as well as a wide range of environments to which it is adapted [1]. All these traits have established this species as a significant component in the traditional diet and life of many nations, keeping in mind that it is usually the only source of proteins and other nutrients in developing countries and people living in rural and marginal areas. It is also getting higher in demand as a source of vegetable proteins in the nutrition of urban population due to the rise in the adoption of flexitarian, vegetarian and vegan diets [2].

The species *Phaseolus vulgaris* is also recognized for the existence of Mesoamerican and Andean gene pools which derived from two independent domestication events in Middle and South America [3]. Accessions belonging to these two gene pools distinguish between themselves according to their phenotypic, biochemical, nutritional, adaptive and genotypic differences [4,5]. A great diversity of the common bean is identified in Europe, mainly as a result of beans' evolution under diverse cropping systems, agro-ecological conditions and farmer's preference in term of types of seeds (market classes) and use [6]. Genetic collections of the species *Phaseolus vulgaris* in Serbia are maintained within breeding institutes. These collections accommodate the seeds of traditional and modern domestic and foreign cultivars, breeding lines and landraces from the territory of Serbia and neighbouring countries. These genetic collections have been characterized for their phenotypic, agronomic and genotypic variability; however, information on nutraceutical value is missing. Nutritional value is an important component in breeding, both from the aspect of increasing the content of certain nutrients, but also from selection of high yielding genotypes of good nutritive and bioactive properties.

Common bean is rich in proteins, carbohydrates, fibres, vitamins, and minerals, as well as a variety of bioactive compounds [7]. Even though common beans are considered vegetables due to the high fibre and mineral content, it is also a protein crop. Dry seed of the beans contains 20-35% of crude proteins, which is more than any other plant-based food. These are high-quality proteins, with almost all essential amino acids in higher quantities, except for methionine and tryptophan. As for carbohydrates, they make up to 70% of seeds' dry matter, with starch being the major component of complex sugars which degrades slowly, making beans low glycaemic index food. Dietary fibres (18-20%) are another component of beans' seed, important for the health of the human digestive tract and cardiovascular system. In addition to this, most of the fat

found in bean seeds are unsaturated fats, essential for the prevention of coronary heart disease, high blood pressure and stroke [8]. Common bean is also recognized for high amount of minerals which are required for proper function of human body system, including macronutrients (sulphur, potassium, phosphorus, calcium, magnesium) and micronutrients (iron, zinc, copper, manganese, iodine). Moreover, beans are rich in vitamins, especially B group vitamins (folates), vitamins E and K [9].

Beans are good sources of bioactive compounds with antioxidant properties, including plant phenolics, tannins, flavonoids, anthocyanins, among others [10]. These phenolic compounds play an important role in antioxidative response through free radicals scavenging activity against harmful effect of ROS [11]. Moreover, the antioxidative activity of the common bean secondary metabolites could protect human cells against damages caused by oxidative stress [12]. Other health effects of beans include prevention of diabetes type 2, peripheral vascular diseases, hypertension, heart attack and in combat of Alzheimer's, Parkinson's disease and various type of cancers [13]. Many products are developed from common bean, including gluten-free flour, biscuits with lower antinutrient contents, high-nutritional bread and other [14]. Therefore, the main objective of this study was to assess nutritional value of a selected set of common bean accessions comprising *Phaseolus vulgaris* core collection with greatest phenotypic and genetic variation.

## RESULTS AND DISCUSSION

Variability of common bean accessions based on studied nutritive traits was presented in Table 1. For all the studied samples, mean values of protein, nitrogen, phosphorus, and sulphur contents were 23.22%, 3.71%, 0.40% and 0.26%, respectively. Cultivar Balkan had the lowest protein (19.62%) and nitrogen (3.14%) content, while the least amount of phosphorus was found among the breeding line BAT477 and landrace L9 (0.33%). On the other hand, landrace L92 distinguished with the largest amount of proteins (31.61%), nitrogen (5.06%) and phosphorus (0.51%) in its seeds. The largest potassium content was found among the cultivar Poboljšani gradištanac and landrace L120 (1.33%), while for the sulphur it was in landrace L29 (0.47%). On the contrary, breeding line BAT477 had the lowest seed amount of both potassium (0.93%) and sulphur (0.20%). Iron content ranged from 45.93 mg/kg in cultivar Dobrudžanski 7 to 104.70 mg/kg in landrace L125, with mean value of 64.18 mg/kg for all studied samples. Other genotypes with increased iron content were landrace L24 (85.63 mg/kg) and breeding line HR45 (83.78 mg/kg). Landrace L120 had the largest zinc content (101.60 mg/kg), as opposed to landrace L10 with the

smallest value (24.17%). Moreover, cultivars Royal Dutch and Vulkan were recognized for elevated zinc content (84.22 mg/kg and 90.02 mg/kg, respectively) compared to average found for all the samples (38.16 mg/kg). The highest variability was observed for zinc (CV = 40.17%); moderate variation was recorded for sulphur (CV = 16.70%) and iron (CV = 14.99%) contents while the lowest variability was found for the contents of protein (CV = 10.33%), nitrogen (CV = 10.33%), phosphorus (CV = 8.49%) and potassium (CV = 7.78%).

**Table 1**. Variability of studied nutritive traits in IFVCNS common bean core collection

| | **Proteins** | **N** | **P** | **K** | **S** | **Fe** | **Zn** |
|---|---|---|---|---|---|---|---|
| | **%** | | | | | **mg/kg** | |
| **Mean** | 23.22 | 3.71 | 0.40 | 1.12 | 0.26 | 64.18 | 38.16 |
| **SE** | 0.32 | 0.05 | 0.005 | 0.001 | 0.001 | 1.27 | 2.03 |
| **CV%** | 10.33 | 10.33 | 8.49 | 7.78 | 16.70 | 14.99 | 40.17 |
| **Range** | 19.62 | 3.14 | 0.33 | 0.93 | 0.20 | 45.93 | 24.17 |
| | 31.61 | 5.06 | 0.51 | 1.33 | 0.47 | 104.70 | 101.60 |

Observed amounts of both nitrogen and protein contents were in the variation range recorded for common bean worldwide [14,8]. However, bean accessions in our study had slightly more nitrogen and protein contents, with greater variability, when compared to the results of Celmeli et al. [15] and de Lima et al. [16]. This could be due to the nature of the studied material, conferring greatest captured phenotypic and genotypic diversity of larger collection, but can also be related to more samples analysed in our study. Plant based proteins make up to 65% of the world's total supply of protein for human consumption, of which 45-50% come from legumes and cereals [17]. This indicates the importance of investigation of new sources of this type of proteins, but also making attempts in increasing protein contents through breeding. Results of this research showed that some landraces had more proteins compared to commercial cultivars, which makes them valuable components in breeding with aforementioned purpose. On the other hand, even though the accessions in the core collection were chosen according to their variability, not significant differences were observed for phosphorus and potassium contents. Recorded values of these two macronutrients were similar to those found in Paredes et al. [18]. Obtained results argue that investigated core collection is not a suitable source of variability for increasing phosphorus and potassium contents via breeding.

Iron and zinc contents recorded in this study were in the same range as observed in research of Islam et al. [19] and Guzman-Maldonado et al. [20]. In addition, the average zinc value corresponded to that found in research of 1000 common bean genotypes from the CIAT's common bean collection [21], while iron content was even higher. As for newer research, iron and zinc contents

were higher compared to the results of Ramirez-Ojeda et al. [22] and de Lima et al. [16]. Therefore, results of this study demonstrated great variability and accumulation of iron and zinc in evaluated bean germplasm, which, in turn, gives the possibility of the selection of cultivars with large quantities of these nutrients. It is estimated that 17% of the population worldwide suffer from zinc deficiency, while for the iron that number reaches 30%. A large percentage of child deaths are associated with zinc insufficiency, while anaemia often occurs due to low iron bioavailability, especially in food of plant origin [23]. By providing sufficient amounts of these micronutrients into the human diet, normal pregnancies may be ensured, as well as adequate child growth and development, immune system function and neurobehavioral development [24].

The total phenolic content ranged from 1.80 mg GAE/g DW (cultivar Biser) to 14.1 mg GAE/g DW (landrace L29), with mean value of 6.46 mg GAE/g DW and relatively large variation (CV = 41.3%). The highest amount of total tannins content was observed in landrace L48 (5.70 mg GAE/g DW and the lowest in landrace L73 (2.70 mg GAE/g DW, with moderate variability, CV = 18.6% (Table 3). Carbas *et al*. [14] observed similar values for total phenolic contents, while de Lima *et al.* [16] found similar total tannin values in bean landraces from Brazil. On contrary, Sahaskul *et al*. [25] recorded smaller variation of total phenolic content, (0.72 to 3.12 mg GAE/g DW, in range), in the study of more than one legume species (2 Phaseolus, 4 Vigna and one Glycine species). Moreover, reported concentrations of these compounds are higher in common beans compared to lentils, chickpea, soybeans, which is related to the better antioxidant and nutraceutical properties of beans and implication on human health [10]. Total phenolic and tannins content, alone or in combination with other constituents, are a potential candidate as a selection criterion for antioxidant activity in beans.

Results of seven non-enzymatic antioxidant assays (DPPH, ABTS, FRAP, NBT, TAA, TRC, and NO inhibitory), involving the measurement of the ability of compound to act as free radical scavengers, and one enzymatic assay LP (lipid peroxidation) are represented in Table 2. Landrace L29 was with highest DPPH and ABTS values (59.20 and 94.00 μmol TE/g DW, while the highest FRAP level was observed in landrace L40 (94.80 μmol TE/g DW. On the contrary, cultivar Biser had the lowest values for DPPH, ABTS and FRAP, with 9.60, 6.80 and 18.00 μmol TE/g DW, respectively. In comparison to the results of Carbas et al. [16] twice as high mean DPPH and FRAP values were observed in our study, and therefore better antioxidant potential. Good free radical scavenging properties with protective roles in cellular oxidative stress caused by dietary habits, inflammation, microbial interactions and other were detected among investigated common bean germplasm. NBT levels ranged from 0.03 U/g DW in breeding line BAT 477 to 0.26 U/mg DW in landrace L120, with mean value of 0.23 U/mg DW.

**Table 2.** Variability of bioactive compounds in IFVCNS common bean core collection

| | TPC mg GAE | TTC mg GAE | DPPH µmol TE | ABTS µmol TE | FRAP µmol TE | NBT U | TAA µmol TE | TRC µmol TE | NO % | LP nmol MDA/ mg protein |
|---|---|---|---|---|---|---|---|---|---|---|
| | g DW | | | | | mg DW | g DW | | | |
| **Mean** | 6.46 | 4.14 | 35.27 | 51.48 | 51.94 | 0.23 | 210.1 | 113.6 | 0.02 | 0.12 |
| **SE** | 0.4 | 0.1 | 1.2 | 0.4 | 0.4 | 0.01 | 0.4 | 1.2 | 0.01 | 0.01 |
| **CV %** | 41.3 | 18.6 | 29.2 | 46.1 | 32.5 | 13.4 | 10.9 | 8.3 | 12.1 | 5.2 |
| **Range** | 1.80 | 2.70 | 9.60 | 6.80 | 18.00 | 0.03 | 262.8 | 134.8 | 0.01 | 0.11 |
| | 14.1 | 5.70 | 59.20 | 94.00 | 94.80 | 0.26 | 144.8 | 85.2 | 0.03 | 0.13 |

TPC – total phenolic content, TTC – total tannin content, NBT – nitroblue tetrazolium test, TAA – total antioxidant activity, TRC – total redox capacity, NO – nitric oxide test, LP – lipid peroxidation

Total antioxidant activity ranged from 144.8 µmol TE/g DW in cultivar Vulkan to 262.8 µmol TE /g DW in cultivar Naya Nayahit, with mean value of 210.1 µmol TE/g DW and variability of CV = 10.9%. Landrace L18 exhibited the lowest total redox capacity (85.2 µmol TE/g DW) compared to landrace L5 with the highest value (134.8 µmol TE/g DW). On the contrary, the same landrace L5 displayed the lowest potential for nitric oxide inhibition (0.01%), while the landrace L120 (0.03%) was distinguished as best for the value of this bioactive compound. Nitric oxide acts in plant–microbe interactions, responses to abiotic stress, stomatal regulation and a range of developmental processes [26]. Additionally, nitric oxide plays an important role in symbiotic organisms, particularly between legumes and *Sinorhizobium* [27]. In beans, NO is involved in lipid and photosynthesis recovery under Mn stress conditions, it is assumed that NO beneficial effects are attributable to NO/Mn cross-talk [28]. According to only enzymatic assay performed in this study, lipid peroxidation ranged from 0.11 nmol MDA/mg protein in landrace L121 to 0.13 nmol MDA/mg protein in landrace L124, with variability of only CV = 5.2% (Table 3). Low variability (CV below 10%) in TRC and LP indicates that differences for these parameters among tested genotypes could be obtained only under stress conditions.

Different nutritional and bioactive profiles were observed between groups generated according to the seed coat traits (market classes). In general, accessions from the Albus group had the lowest level of radical scavenging compounds revealed by ABTS and FRAP assays (36.04 µmol TE/g DW and 41.36 µmol TE/g DW respectively), but relatively large amounts of zinc (42.12 mg/kg). On the other hand, Roseus group was recognized for the large levels of total phenolics (8.50 mg GAE/g DW), DPPH (39.0 µmol TE/g DW), ABTS (83.0 µmol TE/g DW), NBT (0.24 U/g DW) and TRC (124.4 µmol TE/g DW), but the smallest amounts of both iron (58.21 mg/kg) and zinc (29.21 mg/kg). The least amounts of proteins (21.61%), nitrogen (3.46%) and potassium (1.02%)

were found in the Griseus group. Conversely, accessions from Aureus seed form displayed largest amounts of nitrogen (4.09%) and proteins (25.59%), with elevated levels of sulphur (0.30%) and iron (70.72 mg/kg). Highest amounts of iron (83.52 mg/kg) and TAA (242.6 µmol TE/g DW), but lowest amounts of zinc (29.22 mg/kg) were observed in the Niger group. Highest value for zinc content (45.75 mg/kg), total phenolic content (10.46 mg GAE/g DW), DPPH (48.72 µmolTE/ g DW) and FRAP (77.60 µmol TE/g DW) was recorded for Crepito accessions (Table 3). Differences between common bean seed forms (market classes) in terms of their nutritive value were observed in other studies [29,14]. Even though it was suggested that dark-coloured beans have overall better antioxidant properties, that was not completely the case in our study.

**Table 3.** Nutritional and bioactive profile of different bean groups generated according to seed coat traits

| | Albus | Roseus | Versicolor | Griseus | Aureus | Niger | Crepito | Vinosus | Brunneus |
|---|---|---|---|---|---|---|---|---|---|
| **N %** | 3.71 | 3.69 | 3.76 | 3.46 | 4.09 | 3.64 | 3.66 | 3.91 | 3.53 |
| **P %** | 0.41 | 0.40 | 0.40 | 0.37 | 0.43 | 0.39 | 0.42 | 0.40 | 0.40 |
| **K %** | 1.13 | 1.13 | 1.15 | 1.02 | 1.18 | 1.12 | 1.12 | 1.12 | 1.05 |
| **S %** | 0.26 | 0.23 | 0.25 | 0.23 | 0.30 | 0.25 | 0.34 | 0.29 | 0.30 |
| **Fe mg/kg** | 63.27 | 58.21 | 62.13 | 65.46 | 70.72 | 83.52 | 59.86 | 60.89 | 64.28 |
| **Zn mg/kg** | 42.12 | 29.21 | 36.33 | 33.08 | 31.42 | 29.22 | 45.75 | 40.06 | 35.39 |
| **Proteins %** | 23.17 | 23.06 | 23.53 | 21.61 | 25.59 | 22.74 | 22.90 | 24.46 | 22.05 |
| **TPC mg GAE/g DW** | 5.44 | 8.50 | 5.39 | 7.13 | 6.64 | 5.30 | 10.46 | 7.30 | 8.85 |
| **TTC mg GAE/ g DW** | 4.47 | 4.25 | 3.73 | 4.21 | 3.72 | 3.30 | 3.92 | 4.30 | 4.40 |
| **DPPH µmol TE/g DW** | 32.27 | 39.0 | 34.52 | 36.74 | 31.92 | 32.0 | 48.72 | 37.60 | 38.80 |
| **ABTS µmol TE/g DW** | 36.04 | 83.0 | 52.12 | 61.14 | 61.52 | 43.6 | 78.64 | 58.8 | 60.4 |
| **FRAP µmol TE/g DW** | 41.36 | 67.6 | 54.4 | 55.54 | 47.20 | 61.20 | 77.60 | 66.40 | 51.40 |
| **NBT U/mg DW** | 0.22 | 0.24 | 0.23 | 0.20 | 0.23 | 0.23 | 0.23 | 0.23 | 0.23 |
| **TAA µmol TE /g DW** | 205.5 | 216.6 | 207.9 | 214.6 | 207.6 | 242.6 | 206.9 | 218.4 | 222.6 |
| **TRC µmol TE g/DW** | 112.4 | 124.4 | 111.8 | 115.1 | 117.2 | 117.4 | 111.5 | 115.4 | 110.2 |
| **NO %** | 0.02 | 0.02 | 0.02 | 0.02 | 0.02 | 0.02 | 0.02 | 0.02 | 0.02 |
| **LP nmol MDA/mg protein** | 0.12 | 0.13 | 0.12 | 0.12 | 0.12 | 0.11 | 0.12 | 0.12 | 0.12 |

TPC – total phenolic content, TTC – total tannin content, NBT – nitroblue tetrazolium test, TAA – total antioxidant activity, TRC – total redox capacity, NO – nitric oxide test, LP – lipid peroxidation

Principal component analysis reduced the initial number of studied variables (traits) from 16 to 6 with eigenvalues (λ) larger than 1, which explained 69.3% of variability of the examined dataset, in total (Table 4). First two principal components explained 18.46% and 18.09% total variability, respectively, and were separated for graphical representation of relationships among studied traits and accessions. The first principal component was associated with traits such as total phenolics, DPPH, ABST and FRAP. Nitrogen, phosphorus and protein content defined second principal component. The third main component was related to the total antioxidant activity, sulphur and zinc contents. NBT and LP defined forth, while total tannins and iron content defined fifth and sixth principal component, respectively.

**Table 4.** Principal component analysis of studied common bean core collection: eigenvalues, total variance, and cumulative variance

| Principal component | Eigenvalue | Total variance % | Cumulative variance % |
|---|---|---|---|
| 1 | 3.14 | 18.46 | 18.46 |
| 2 | 3.07 | 18.09 | 36.55 |
| 3 | 1.69 | 9.95 | 46.51 |
| 4 | 1.46 | 8.57 | 55.08 |
| 5 | 1.29 | 7.60 | 62.69 |
| 6 | 1.12 | 6.61 | 69.29 |

Vector projections of studied traits and position of accessions on biplot graph enable identification of their relationships according to investigated nutritive value. Therefore, positive correlations could be observed between the traits that defined first PC (TPC, ABTS, FRAP, DPPH) which were in negative association with traits of the second PC (proteins, nitrogen, phosphorus). Majority of accessions grouped in the middle of the biplot chart (G1), comprising of 28 landraces, one breeding line and six cultivars (Naya Nayahit, Spinel, Alubia, Poboljšani gradištanac, Gerle and Harwood). Both nutritive and bioactive compounds levels found in these accessions were around the average for the entire core collection. Second group (G2) consisted of six cultivars (Žutotrban, Dobrudžanski 7, Balkan, Pasuljica P1, Biser, C-20) and one landrace (L12). Main features of these cultivars and landrace were the lowest observed values for total phenolics content (2.80 mg GAE/g DW), DPPH (14.97 μmol TE/g DW), ABTS (25.14 μmol TE (g/DW) and FRAP (24.34 μmol TE/g DW) in average. Two cultivars (Vulkan and Panonski tetovac), one breeding line (HR45) and four landraces (L14, L76, L119 and L120) comprised third group (G3) and were characterized with largest mean content of TRC (120.80 μmol TE/g DW), nitrogen (4.27%), phosphorus (0.44%), zinc (52.21 mg kg-1) and protein (26.73%) contents. The largest average amount of total phenolics content (11 mg GAE/gDW), DPPH (47.00 μmol TE/g DW), ABTS (78.37 μmol TE/g DW) and FRAP (77.93 μmol

TE/g DW) were recorded in accessions of the fourth group (G4) that clustered around the same vectors on biplot graph. This group included one breeding line (BAT 477) and five landraces (L29, L35, L40, L121, and L122). Two accessions had separate position, cultivar Royal Dutch which distinguished according to higher amounts of DPPH (50 μmol TE/g DW), ABTS (86.4 μmol TE/g DW), FRAP (83.2 μmol TE/g DW) and zinc content (84.22 mg/kg) and landrace L92 with elevated levels of nitrogen (5.06%), phosphorus (0.51%), potassium (1.26%) and proteins (31.61%) contents (Fig. 1).

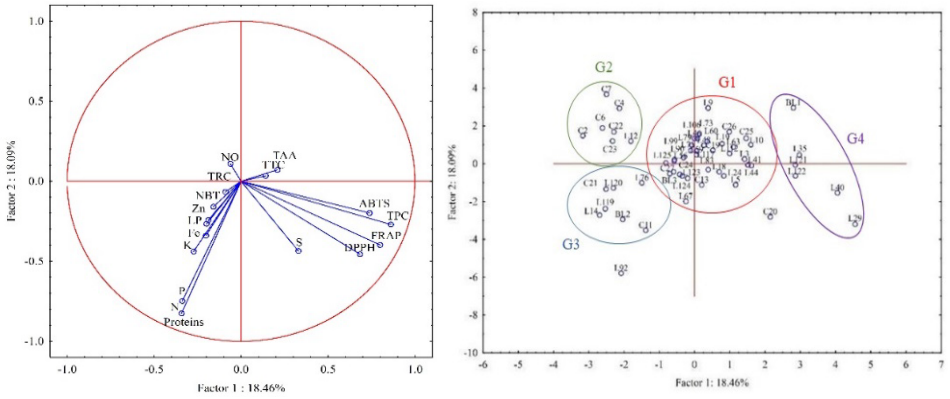


TPC – total phenolic content, TTC – total tannin content, NBT – nitroblue tetrazolium test, TAA – total antioxidative activity

**Figure 1.** Principal component analysis biplot representing distribution of nutritional and biochemical characteristics and common bean accessions in the first and second dimension

Hierarchical cluster analysis based on squared Euclidean distance was applied in order to assess the relationships among accessions in more detail (Figure 2). The dendrogram divided landraces and cultivars in three main clusters (A, B, C), with additional subdivision within the third cluster (C1, C2, C3). Cluster A included only two cultivars of Bulgarian origin, Vulkan and Dobrudzanski 7 and one landrace (L120). These genotypes are recognized for the largest amount of zinc content on average (91.95 mg/kg). Four accessions were organized within cluster B, one breeding line, HR45, and three landraces (L24, L92 and L125). Largest amount of iron (88.36 mg/kg), nitrogen (4.29%) and protein content (26.84%) was observed in this group. Accessions comprising cluster C accounted for 87.7% of the studied core collection. Most of these accessions had values of studied traits around or below the average, with certain deviation. Subcluster C1 included cultivars Balkan and Spinel, and landraces L19, L29, L41, L60. Main features of these accessions were higher values of total phenolics content (7.85 mg GAE/g DW). Largest group was subcluster C2, which, together with

subcluster C3 had better total antioxidant activity (213.53 and 212.34 μmol TE/g DW), respectively), while C3 subcluster also had in average more iron (73.07 mg/kg) and total phenolics (7.27 mg GAE/ g DW) in their seeds.

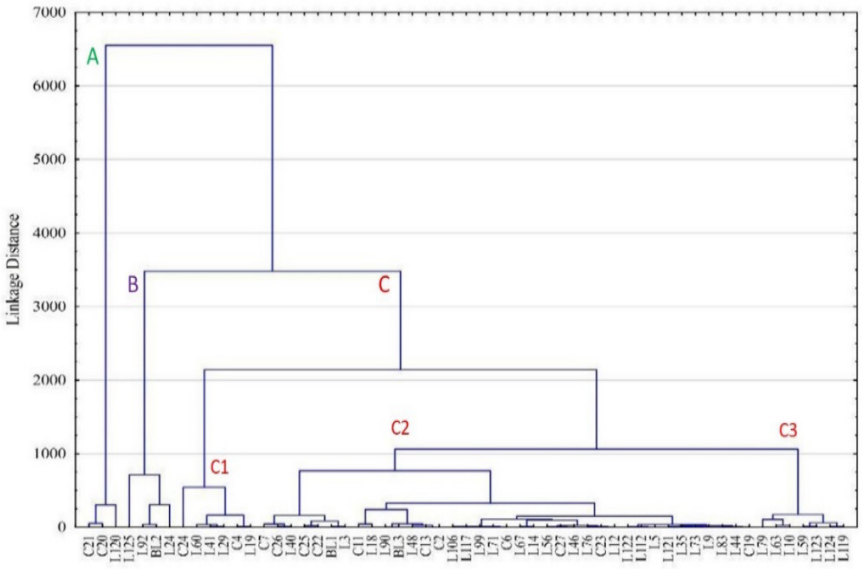


**Figure 2.** Hierarchical cluster analysis based on squared Euclidean distance of common bean core collection

After describing each accession according to its nutritional profile, application of PCA and cluster analysis revealed underlying structure of studied common bean germplasm. With the deployment of cultivars and landraces in several small homogenous groups, accessions with specific combinations of nutritional compounds were acknowledged. It was possible to distinguish accessions with superior composition in terms of specific nutritional and bioactive compounds. This information is important for the selection of preferable accessions for nutritive quality enhancing through breeding. Moreover, results of this research will enable accessions of already known good agronomic performance associated with elevated nutritional value to be advanced in production as functional food.

## CONCLUSIONS

Bean accessions proved to have high nitrogen and protein contents, with greater variability. However, some landraces (L92, L14, L67, and L119) had more proteins compared to commercial cultivars, which makes them valuable

components in breeding with afore mentioned purpose. Results of this study demonstrated great variability and accumulation of iron and zinc in evaluated bean germplasm, which, in turn, gives the possibility of the selection of cultivars with large quantities of these nutrients. Among different antioxidant tests applied DPPH, ABTS and FRAP had high, genotype-based, CV in range 30-40%.

Therefore, these tests could be used in the selection of accessions according to non-enzymatic antioxidant capacity. With the application of PCA and cluster analysis, nutritive profile was determined for each accession, while underlying structure and grouping patterns of studied germplasm were revealed. All of these results could help in the choice of new genotypes with desirable traits in further nutritive quality breeding.

## EXPERIMENTAL SECTION

A total of 57 accessions from the common bean core collection maintained at the institute of Field and Vegetable Crops, Novi Sad (IFVCNS), Serbia was analysed in this paper.

The material was selected based on the greatest phenotypic and genetic variability detected in previous studies. This included 33 landraces collected from various locations in Serbia, 5 landraces of foreign origin and 1 landrace of unknown origin, 6 domestic cultivars, 9 foreign cultivars and 3 foreign breeding lines. Landraces, cultivars and breeding lines were also classified according to the seed traits (seed coat colour, seed coat patterns) in several seed forms, most commonly grown in Serbia: Roseus (pink seed colour), Versicolor (seed coat pattern), Griseus (greenish-yellow seed colour), Aureus (yellow and golden-yellow seed colour), Albus (white seed colour), Niger (black seed colour), Crepito (cream seed colour), Vinosus (red seed colour) and Brunneus (brown seed colour). In addition, gene pool for each accession was determined based on phaseolin types in previous studies [30] and accessions were designated as Mesoamerican or Andean (Table 5; Figure 3).

Bean accessions were grown in a one-year trial under field conditions, since the primary goal was to make comparison between the accessions grown under the same environmental conditions. Field trial was set as a randomised complete block design with three replications at the experimental field of IFVCNS. The plot was arranged in three rows, 2 m long, with a distance between the rows of 60 cm and 5 cm in the row. The beans have been sown in the beginning of May and harvested in September. After harvest, air-dried 100 g seeds of each bean accession were grounded using a hand mill for the following analyses. The analyses were carried out by the IFVCNS and Faculty of Agriculture, University of Novi Sad.

**Table 5.** List of the accessions from IFVCNS common bean core collection chosen for the study

| No | Accession / origin | Seed form | Gene pool | No | Accession / origin | Seed form | Gene pool |
|---|---|---|---|---|---|---|---|
| **1** | L3 (SRB[1]) | *Roseus* | A* | 30 | L106 (SRB) | *Albus* | A |
| **2** | L5 (SRB) | *Roseus* | A | 31 | L112 (SRB) | *Albus* | A |
| **3** | L9 (SRB) | *Griseus* | A | 32 | L117 (SRB) | *Albus* | A |
| **4** | L10 (SRB) | *Griseus* | A | 33 | L119 (SRB) | *Aureus* | M |
| **5** | L12 (SRB) | *Albus* | M | 34 | L120 (KAZ) | *Albus* | A |
| **6** | L14 (SRB) | *Versicolor* | A | 35 | L121 (BIH) | *Versicolor* | A |
| **7** | L18 (SRB) | *Versicolor* | A | 36 | L122 (BIH) | *Crepito* | A |
| **8** | L19 (SRB) | *Versicolor* | A | 37 | L123 (HRV) | *Aureus* | A |
| **9** | L24 (SRB) | *Griseus* | A | 38 | L124 (BIH) | *Versicolor* | A |
| **10** | L29 (SRB) | *Crepito* | A | 39 | L125 (N/A) | *Niger* | M |
| **11** | L35 (SRB) | *Brunneus* | A | 40 | C2 (**Žutotrban**, SRB) | *Versicolor* | A |
| **12** | L40 (SRB) | *Crepito* | A | 41 | C4 (**Balkan**, SRB) | *Albus* | M |
| **13** | L41 (SRB) | *Vinous* | A | 42 | C6 (**Pasuljica P-1**, SRB) | *Albus* | M |
| **14** | L44 (SRB) | *Aureus* | A | 43 | C7 (**Biser**, SRB) | *Albus* | M |
| **15** | L46 (SRB) | *Aureus* | A | 44 | C11 (**Panonski tetovac**, SRB) | *Albus* | A |
| **16** | L48 (SRB) | *Albus* | A | 45 | C13 (**Poboljšani gradištanac**, SRB) | *Albus* | M |
| **17** | L56 (SRB) | *Versicolor* | A | 46 | C19 (**Naya Nayahit**, USA) | *Niger* | M |
| **18** | L59 (SRB) | *Albus* | A | 47 | C20 (**Royal Dutch**, NLD) | *Crepito* | A |
| **19** | L60 (SRB) | *Griseus* | A | 48 | C21 (**Vulkan**, BGR) | *Albus* | M |
| **20** | L63 (SRB) | *Griseus* | A | 49 | C22 (**Dobrudžanski 7**, BGR) | *Albus* | A |
| **21** | L67 (SRB) | *Vinosus* | A | 50 | C23 (**C-20**, USA) | *Albus* | M |
| **22** | L71 (SRB) | *Crepito* | A | 51 | C24 (**Spinel**, USA) | *Albus* | M |
| **23** | L73 (SRB) | *Griseus* | A | 52 | C25 (**Alubia**, BRA) | *Albus* | A |
| **24** | L76 (SRB) | *Versicolor* | A | 53 | C26 (**Gerle**, BGR) | *Versicolor* | M |
| **25** | L79 (SRB) | *Albus* | M | 54 | C27 (**Harwood**, CAN) | *Albus* | M |
| **26** | L83 (SRB) | *Albus* | M | 55 | BL1 (**BAT 477**, BGR) | *Griseus* | M |
| **27** | L90 (SRB) | *Brunneus* | M | 56 | BL2 (**HR45**, CAN) | *Albus* | M |
| **28** | L92 (SRB) | *Aureus* | M | 57 | BL3 (**Oreol L-xan**, BGR) | *Albus* | A |
| **29** | L99 (SRB) | *Versicolor* | A | | | | |

* A – Andean, M - Mesoamerican

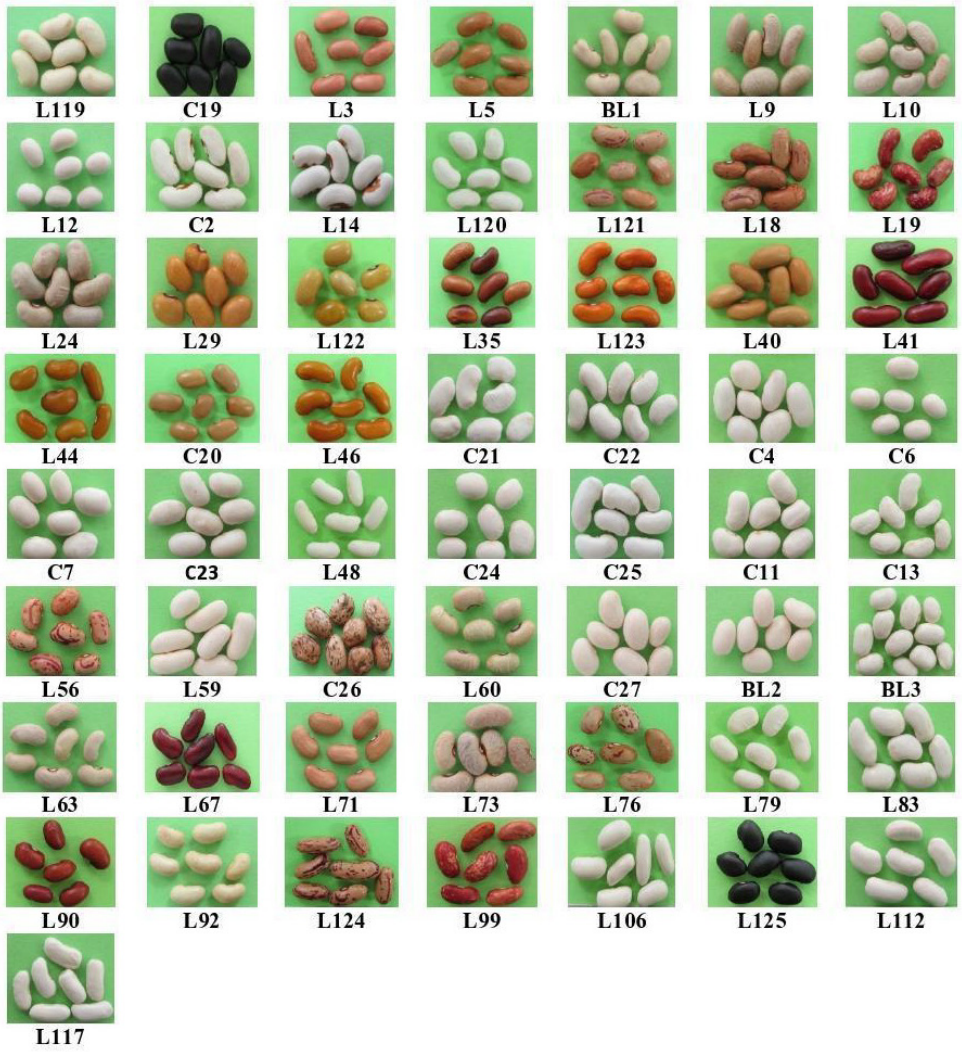


**Figure 3.** Studied accessions from the IFVCNS, Serbia, common bean core collection

The main common bean nutritive quality parameters assessed in this study included content of proteins (%), nitrogen (%), phosphorus (%), potassium (%), sulphur (%), iron (mg/kg$^{-1}$) and zinc (mg/kg$^{-1}$), with the application of the following methods. Nitrogen and sulphur content were determined in the elemental analysis with the application of CHNS elemental analyser Elementar III Vario El; protein content was determined with the conversion factor (N × 6.25), where

nitrogen content was multiplied by 6.25. Potassium, phosphorus, iron and zinc contents were determined with the method of inductively coupled plasma on the apparatus ICP-OES Varian. Content of the metals was assessed after the destruction of organic matter by mineral acids (10 ml $HNO_3$ and 2 ml $H_2O_2$) in the process of microwave decomposition at 180°C, in the apparatus Ethos1-MILESTONE.

Analysis of biochemical parameters was performed in the Laboratory for Biochemistry, Faculty of Agriculture Novi Sad (Serbia). Grounded seed material of each accession (500 mg) was extracted with methanol solution (50 ml) by sonication for 20 minutes in an ultrasonic bath at ambient temperature. The extracts were rapidly vacuum-filtered through a sintered glass funnel and kept refrigerated until assayed. The total phenolic content (TPC) was determined using a Folin-Ciocalteu colorimetric method [31]. Total tannins content (TTC) was determined by the Folin-Ciocalteu procedure, after removal of tannins by their adsorption on insoluble matrices [32]. Calculated values were subtracted from TPC and TTC and expressed as mg of gallic acid equivalent per g of seed dry weight (mg GAE/g DW). The scavenging efficiency of free radicals was tested in a DPPH (2,2-diphenyl-1-picrylhydrazyl) methanol solution [33]. Ferric-reducing antioxidant power (FRAP) assay was carried out according to Valentao *et al*. [34].

The ABTS (2,2′-azinobis-(3-ethylbenzothiazoline-6-sulfonic acid)) assay was based on a method developed by Miller *et al*. [35]. The total antioxidant activity (TAA) and NBT (nitroblue tetrazolium test) were evaluated by method of Kalaskar and Surana [36]. A reducing power assay (total reduction capacity) (TRC) was performed by the method of Saha *et al* [37]. A methanol solution of known trolox concentrations was used for calibration and formation of standard curve. The DPPH, FRAP, ABTS, TAA and TRC are expressed in μmol trolox equivalent antioxidant capacity per g seed dry weight (μmol TE/g DW). NBT is expressed as U per mg of seed dry weight (U/mg DW). Protein content in homogenates was determined using bovine serum albumin as a protein standard test [39]. Lipid peroxidation (LP) was measured at 532 nm using the thiobarbituric acid (TBA) test [39] and expressed as nmol malondialdehyde equivalents per mg protein (nmol MDA (mg/protein). NO-nitric oxide test was performed according to Shirinova *et al* [40]. Percentage was calculated based on the ability of extracts to inhibit NO formation.

*Statistical analysis* was performed using software Statistica, version 13.2 (Dell Inc., USA). Descriptive statistics, including mean, standard error (SE) of mean, range and coefficient of variation was estimated for all studied traits. Principal component analysis (PCA) was performed based on correlation variances to identify significant traits responsible for overall variability, as well

as to identify underlying structure of studied collection. In addition, for better assessment of genotypes grouping cluster analysis based on complete linkage and squared Euclidean distance was performed.

## ACKNOWLEDGMENTS

This research was supported by the Ministry of Science, Technological Development and Innovation of the Republic of Serbia, grant No. 451-03-47/2023-01/200032.

## REFERENCES

1. A. De Ron; A. Gonzales; A. Rodino; M. Santalla; L. Godoy; R. Papa; *Arbor*, **2016,** *192*, 779.
2. D. Rubiales; P. Annicchiarico; M.C. Vaz Patto; B. Julier; *Front. Plant. Sci.,* **2021**, *12*, 782574.
3. P. Gepts; F.A. Bliss; Econ. Bot., **1988,** *42*, 86-104.
4. L. Raggi; B. Tiranti; V. Negri; *Genet. Resour. Crop Evol.*, **2013**, *60*, 1515-1530.
5. B. Pipan; V. Meglič; *BMC Plant. Biol.,* **2019**, *19*, 442.
6. A. Savić; M. Zorić; M. Brdar-Jokanović; M. Zdravković; M. Dimitrijević; S. Petrović; D. Živanov; M. Vasić; *Genet. Resour. Crop Evol.,* **2020,** *67*, 2195-2212.
7. M. Sitohy; E.M. Deskoy; A. Osman; M.R. Rady; *Sci. Hortic.,* **2020,** *271*, 109495.
8. S. Ivanovska; M. Jankulovska; N. Sandeva Atanasova; Genetic Diversity of Beans (*Phaseolus* sp.). Macedonian Ecological Society, Skopje, **2021**, pp. 76-80.
9. S. Jan; I.A. Rather; P.A. Sofi; M.A. Wani; F.A. Sheikh; M.A. Bhat; R.R. Mir; *Legum. Sci.,* **2021,** *3*, *e86*.
10. Y.D. Garcia-Diaz; E.N. Aquino-Bolanos; J.L. Chavez-Servia; A.M. Vera-Guzman; J.C. Carillo-Rodriguez; *Chil. J. Agric. Res.*, **2018**, *78,* 255-265.
11. J. Mierziak; K. Kostyn; A. Kulma; *Molecules*, **2014**, *19,* 16240-16265.
12. R. Campos-Vega; B.D. Oomah; G.F. Loarca-Pina; Cultivars: Chemical Properties, Antioxidant Activities and Health Benefits, Nova Science Publishers Inc., **2013**, pp. 157-170.
13. P.X. Chen; Zhang H.; Marcone M.F.; Pauls K.P.; Liu R.; Tang Y.; Zhang B.; J.B. Renaud; *J. Funct. Foods,* **2017,** *38*, 675-685.
14. B. Carbas; N. Machado; D. Oppolzer; L. Ferreira; M. Queiroz; C. Brites; E.A.S. Rosa; A.I. Barros; Antioxidants **2020**, *9*, 186.
15. T. Celmeli; H. Sari; H. Canci; D. Sari; A. Adak; T. Eker; C. Toker; *Agronomy* **2018**, 8, 166.
16. J.D. De Lima; W. Ribeiro Rivadavea; S.A. Frehner Kavalco; A.C. Goncalves Junior; A.D. Lopes; G.J. da Silva; *AIMS Agric. Food*, **2021**, *6*, 932-944.
17. A. Iqbal; A. Iqtidar; N. Ateeq; M. Khan; *Food Chem.,* **2006,** 97, 331-335.
18. M. Paredes; V. Becerra; J. Tay; *Chil. J. Agric. Res.* **2009***, 69*, 486-495.

19. F. Islam; K. Basford; R. Redden; A. Gonzales; P. Kroonenberg; S. Beebe; Genet. Resour. *Crop. Evol.* **2002**, *49,* 217-283.
20. S. Guzman-Maldonado; J. Acosta-Gallegos; O. Paredes-Lopez; *J. Sci. Food* Agric. **2000**, *80*, 1874-1881
21. S. Beebe; A. Gonzales; J. Rengifo; *Food and Nutr. Bull.* **2000**, 21, 428-433
22. A. Ramirez-Ojeda; R. Moreno-Rojas; F. Camara-Martos; *J. Food Compost Anal.* **2018**, *73*, 17-28.
23. S. Gupta; A.K.M. Brazier; N.M. Lowe; *J. Hum. Nutr. Diet* **2020**, *33*, 624-643
24. C. Chavez-Mendosa; E. Sanchez; *Molecules*, **2017**, *22*, 1360.
25. Y. Sahaskul; A. Aursalung; S. Thangsiri; P. Wonchang; P. Sangkasa-od; A. Wongpia; A. Polpanit; W. Inthachat,; P. Temviriyanukul; U. Suttisansanee; *Foods*, **2022,** *11*, 2062.
26. L. Mur; J. Mandon; S. Persijin; S. Cristescu; I. Moshkov; G. Novikova; M. Hall; F. Harren; K. Hebelstrup; K. Gupta; *AoB PLANTS 5, pls052*, **2013.**
27. E. Baudouin; L. Pieuchot; G. Engler; N. Pauly; A. Puppo; *Mol. Plant-Microbe Interact.* **2006**, *19*, 970-975.
28. Y. Mahjoubi; T. Rzigui; O. Kharbech; S.N. Mohamed; L. Abaza; A. Chaoui; I. Nouairi; W. Djebali; *Protoplasma* **2022**, *259*, 949-964.
29. F. Giusti; G. Caprioli; M. Ricciutelli; S. Vittori; G. Sagratini; *Food Chem.,* **2016**, *221*, 689-697.
30. A. Savić; Genotypic and phenotypic characterization of dry bean (Phaseolus vulgaris L.) collection PhD thesis, University of Novi Sad, Faculty of Agriculture, **2019**, pp 82-86. (in Serbian)
31. V. Nagavani; T. Raghava Rao; *Adv. Biol. Res.,* **2010**, *41*, 159-168.
32. A. Hagermann; I. Harvey-Mueller; H.P.S. Makkar; A Laboratory Manual FAO/IAEA Working Document **2000**, 4.
33. H.Y. Lai; Y.Y. Lim; *Int. J. Environ. Sci. Dev.,* **2011,** *2*, 442-447.
34. P. Valentao; E. Fernandes; F. Carvalho; P.B. Andrade; R.M. Seabra; M.L. Bastos; *J. Agric. Food Chem.,* **2002**, *50*, 4989-4993.
35. N.J. Miller; C. Rice-Evans; M.J. Davies; V. Gopinathan; A. Milner; *Clin. Sci.,* **1993**, *84*, 407-412.
36. M.G. Kalaskar; S.J. Surana; *J. Chil. Chem. Soc.,* **2014**, *59*, 2299-2302.
37. A.K. Saha; M.R. Rahman; M. Shahriar; S.K. Saga; N. Al Azad; S. Das; J *Pharmacogn. Phytochem.,* **2013**, *2*, 181-188.
38. M. Bradford; *Anal Biochem* **1976,** *72*, 248-254.
39. S. Mandal; A. Mitra; N. Mallick; *Physiol. Mol. Plant. Pathol.,* **2008**, *72*, 56-61.
40. A.G. Shirinova; G.V. Prokhorova; V.M. Ivanov; E.A. Osipova; D. Chebukov; *J Anal. Chem.,* **1993**, *48*,128-133.